

NUMERICAL MODELING AND EXPERIMENTAL INVESTIGATION OF LASER-
ASSISTED MACHINING OF SILICON NITRIDE CERAMICS

by

XINWEI SHEN

B.S. Sichuan University, 1991
M.S. Sichuan University, 1994

AN ABSTRACT OF A DISSERTATION

submitted in partial fulfillment of the requirements for the degree

DOCTOR OF PHILOSOPHY

Department of Industrial and Manufacturing Systems Engineering
College of Engineering

KANSAS STATE UNIVERSITY
Manhattan, Kansas

2010

Abstract

Laser-assisted machining (LAM) is a promising non-conventional machining technique for advanced ceramics. However, the fundamental machining mechanism which governs the LAM process is not well understood so far. Hence, the main objective of this study is to explore the machining mechanism and provide guidance for future LAM operations. In this study, laser-assisted milling (LAMill) of silicon nitride ceramics is focused.

Experimental experience reveals that workpiece temperature in LAM of silicon nitride ceramics determines the surface quality of the machined workpiece. Thus, in order to know the thermal features of the workpiece in LAM, the laser-silicon nitride interaction mechanism is investigated via heating experiments. The trends of temperature affected by the key parameters (laser power, laser beam diameter, feed rate, and preheat time) are obtained through a parametric study. Experimental results show that high operating temperature leads to low cutting force, good surface finish, small edge chipping, and low residual stress. The temperature range for brittle-to-ductile transition should be avoided due to the rapid increase of fracture toughness.

In order to know the temperature distribution at the cutting zone in the workpiece, a transient three-dimensional thermal model is developed using finite element analysis (FEA) and validated through experiments. Heat generation associated with machining is considered and demonstrated to have little impact on LAM. The model indicates that laser power is one critical parameter for successful operation of LAM. Feed and cutting speed can indirectly affect the operating temperatures.

Furthermore, a machining model is established with the distinct element method (or discrete element method, DEM) to simulate the dynamic process of LAM. In the microstructural modeling of a β -type silicon nitride ceramic, clusters are used to simulate the rod-like grains of the silicon nitride ceramic and parallel bonds act as the intergranular glass phase between grains. The resulting temperature-dependent synthetic materials for LAM are calibrated through the numerical compression, bending and fracture toughness tests. The machining model is also validated through experiments in terms of cutting forces, chip size and depth of subsurface damage.

NUMERICAL MODELING AND EXPERIMENTAL INVESTIGATION OF LASER-
ASSISTED MACHINING OF SILICON NITRIDE CERAMICS

by

XINWEI SHEN

B.S. Sichuan University, 1991
M.S. Sichuan University, 1994

A DISSERTATION

submitted in partial fulfillment of the requirements for the degree

DOCTOR OF PHILOSOPHY

Department of Industrial and Manufacturing Systems Engineering
College of Engineering

KANSAS STATE UNIVERSITY
Manhattan, Kansas

2010

Approved by:

Major Professor
Dr. Shuting Lei

Copyright

XINWEI SHEN

2010

Abstract

Laser-assisted machining (LAM) is a promising non-conventional machining technique for advanced ceramics. However, the fundamental machining mechanism which governs the LAM process is not well understood so far. Hence, the main objective of this study is to explore the machining mechanism and provide guidance for future LAM operations. In this study, laser-assisted milling (LAMill) of silicon nitride ceramics is focused.

Experimental experience reveals that workpiece temperature in LAM of silicon nitride ceramics determines the surface quality of the machined workpiece. Thus, in order to know the thermal features of the workpiece in LAM, the laser-silicon nitride interaction mechanism is investigated via heating experiments. The trends of temperature affected by the key parameters (laser power, laser beam diameter, feed rate, and preheat time) are obtained through a parametric study. Experimental results show that high operating temperature leads to low cutting force, good surface finish, small edge chipping, and low residual stress. The temperature range for brittle-to-ductile transition should be avoided due to the rapid increase of fracture toughness.

In order to know the temperature distribution at the cutting zone in the workpiece, a transient three-dimensional thermal model is developed using finite element analysis (FEA) and validated through experiments. Heat generation associated with machining is considered and demonstrated to have little impact on LAM. The model indicates that laser power is one critical parameter for successful operation of LAM. Feed and cutting speed can indirectly affect the operating temperatures.

Furthermore, a machining model is established with the distinct element method (or discrete element method, DEM) to simulate the dynamic process of LAM. In the microstructural modeling of a β -type silicon nitride ceramic, clusters are used to simulate the rod-like grains of the silicon nitride ceramic and parallel bonds act as the intergranular glass phase between grains. The resulting temperature-dependent synthetic materials for LAM are calibrated through the numerical compression, bending and fracture toughness tests. The machining model is also validated through experiments in terms of cutting forces, chip size and depth of subsurface damage.

Table of Contents

List of Figures	viiiix
List of Tables	xii
Acknowledgements.....	xiii
Nomenclature and Abbreviation.....	xv
Chapter 1 - Introduction.....	1
1.1 Motivation.....	1
1.2 Literature Review	3
1.2.1 Ceramic Machining.....	3
1.2.2 Laser-Assisted Machining of Ceramics	6
1.2.3 Models for Laser-Assisted Machining of Ceramics	10
1.3 Objectives of This Research	18
1.4 Organization of Dissertation.....	18
Chapter 2 - Experimental Study on Operating Temperature in Laser-Assisted Machining of Silicon Nitride Ceramics.....	20
2.1 Introduction.....	20
2.2 Experimental Setup of LAMill	22
2.3 Investigation on Laser-Si ₃ N ₄ Interaction Mechanism.....	24
2.3.1 Heating Experiments.....	24
2.3.2 Effect of Silica Bubble on Heating	28
2.4 Parametric Study on Heating Experiments	29
2.4.1 Parameters in LAMill	29
2.4.2 Preheat Time	30
2.4.3 Laser Power	31
2.4.4 Laser Beam Diameter	31
2.4.5 Feed Rate	31
2.4.6 Laser Intensity.....	34
2.5 Evaluation of Surface Quality under Different Operating Temperatures.....	34

2.5.1 Operating Temperature and Cutting Force	35
2.5.2 Evaluation of Surface Quality	38
2.6 Guidelines on Parameter Selection	42
2.7 Conclusions	43
Chapter 3 - Thermal Modeling and Experimental Investigation of Laser-Assisted Machining of	
Silicon Nitride Ceramics.....	44
3.1 Introduction.....	44
3.2 Transient Three-Dimensional FEA Model	47
3.2.1 Mathematical Description of the Model	47
3.2.2 Model Development Using FEA	50
3.3 Experimental Setup.....	55
3.4 Simulation Results	56
3.4.1 Temperature Distributions of the Workpiece	56
3.4.2 Effect of Heat Generation in Machining.....	58
3.4.3 Uncertainty Analysis.....	61
3.5 Model Validation	62
3.6 Guidelines on Parameter Selection	64
3.7 Conclusions.....	68
Chapter 4 - Creation of Synthetic Material for Machining Simulation Using DEM.....	
4.1 Introduction.....	69
4.2 DEM and Advanced Ceramics	70
4.3 Microstructural Modeling of a Silicon Nitride Material.....	71
4.3.1 Creation of Synthetic Silicon Nitride Material	71
4.3.2 Microstructural Modeling of β -Si ₃ N ₄	74
4.3.3 Calibration for the Synthetic Material	79
4.4 Specimen Dimensions for Material Removal.....	87
4.5 Conclusions.....	89
Chapter 5 - Machining Modeling and Experimental Investigation of Laser-Assisted Machining of	
Silicon Nitride Ceramics	90

5.1 Introduction.....	90
5.2 Temperature-Dependent Synthetic Material.....	92
5.2.1 Temperatures over the Cutting Zone	93
5.2.2 Synthetic Specimen for LAM	94
5.2.3 Creation of Temperature-Dependent Synthetic Specimen	96
5.3 Equivalent Orthogonal Cutting.....	96
5.4 Experimental Setup.....	99
5.5 Model Validation	100
5.6 Conclusions.....	110
References.....	111
Appendix A - Publications Related to Ph.D. Dissertation	124
Appendix B - Finite Element Discretization Solution: Newton-Raphson Procedure in ANSYS	126

List of Figures

Figure 2.1 Experimental setup of laser-assisted milling	23
Figure 2.2 Schematic of LAMill setup	23
Figure 2.3 Workpiece surfaces	25
Figure 2.4 EDS spectrum of elements detected in the heated zone	25
Figure 2.5 EDS spectrum of elements detected in the bubble	27
Figure 2.6 Silica bubble	27
Figure 2.7 EDS spectrum of elements detected in the powders	27
Figure 2.8 Effect of silica bubble on temperature	28
Figure 2.9 Effect of preheat time on temperature	32
Figure 2.10 Effect of laser power on temperature	32
Figure 2.11 Effect of laser beam diameter on temperature	33
Figure 2.12 Effect of feed rate on temperature	33
Figure 2.13 Damage in a machined surface	34
Figure 2.14 Predicted temperature histories	36
Figure 2.15 Relationship between temperature and main cutting force	36
Figure 2.16 Relationship between fracture toughness and temperature	37
Figure 2.17 Machined surfaces under different operating temperatures	39
Figure 2.18 Profiles of exit edge chipping	39
Figure 2.19 Surface roughness and operating temperature	40
Figure 2.20 Surface residual stress under different operating temperatures	40
Figure 3.1 Schematic of laser-assisted milling	48
Figure 3.2 FEA model with one half of the workpiece	51
Figure 3.3 Schematic of cutting zone in milling	53
Figure 3.4 FEA mesh for the cutting zone	53
Figure 3.5 Positions of laser spot and pyrometer spot	57
Figure 3.6 Temperature contours of the workpiece obtained from simulation	59

Figure 3.7 Cutting zone and its temperatures	60
Figure 3.8 Temperature contours obtained on the back face from simulation	60
Figure 3.9 Temperature histories with $P_l = 300$ W	65
Figure 3.10 Temperature histories with $P_l = 410$ W	65
Figure 3.11 Temperature histories with $P_l = 470$ W	66
Figure 3.12 Temperature histories with $f = 0.012$ mm/tooth/rev	66
Figure 3.13 Temperature histories with $f = 0.048$ mm/tooth/rev	67
Figure 4.1 Physical mechanism for axial cracking	72
Figure 4.2 The microstructure of a typical dense ceramic	72
Figure 4.3 Synthetic specimen	75
Figure 4.4 SEM image of a β -type silicon nitride ceramic	76
Figure 4.5 Parallel-bond	77
Figure 4.6 Schematic of the compression test	81
Figure 4.7 Axial stress versus axial strain in a compression test	81
Figure 4.8 Four-point fixture schematic of the bending test	84
Figure 4.9 Load versus deflection in a bending test	84
Figure 4.10 Four-point fixture schematic of the fracture toughness test	86
Figure 4.11 Load versus deflection in a fracture toughness test	86
Figure 4.12 Schematic of material removal configuration	88
Figure 5.1 Schematics of laser-assisted milling	95
Figure 5.2 Schematics of laser-assisted milling	98
Figure 5.3 Orthogonal cutting in simulation	98
Figure 5.4 Configuration of the orthogonal cutting	101
Figure 5.5 Contact-force distribution from simulation	101
Figure 5.6 Histories of the cutting forces from simulation	103
Figure 5.7 Comparison of the experimental and the simulated cutting forces under different cutting temperatures	103
Figure 5.8 Tool wear under different cutting temperatures ($L_c = 10$ mm)	105
Figure 5.9 Exit edge chipping at different cutting temperatures	106
Figure 5.10 Chips in LAMill experiments ($T_c = 1350^\circ\text{C}$)	107

Figure 5.11 Chips in simulation ($T_c = 1350^\circ\text{C}$)	107
Figure 5.12 Subsurface damages detected from LCSM	108
Figure 5.13 Surface/subsurface damages	109
Figure 5.14 Comparison of the maximum subsurface damages (d) at different cutting temperatures	109
Figure B.1 Newton-Raphson solution - one iteration.....	127
Figure B.2 Newton-Raphson solution - next iteration	128
Figure B.3 Incremental newton-raphson procedure	129
Figure B.4 Initial-stiffness newton-raphson.....	130
Figure B.5 Arc-length approach with full Newton-Raphson.....	137

List of Tables

Table 1.1 Limitations in machining models for brittle materials	18
Table 2.1 Operating conditions in the parametric study	30
Table 3.1 Thermal properties of silicon nitride	55
Table 3.2 Thermal properties of silicon nitride	57
Table 3.3 Operating conditions of laser-assisted milling of Si_3N_4	63
Table 4.1 Microparameters that define the DEM material	73
Table 4.2 Parameters that control the material-creation procedure	74
Table 4.3 Parameters in numerical tests	82
Table 4.4 Property comparison between real silicon nitride and synthetic material (25 °C).....	82
Table 5.1 Properties of Si_3N_4	93
Table 5.2 Parameters that control the material-creation procedure	97
Table 5.3 Microparameters that define the DEM material (1350°C).....	97
Table 5.4 Operating conditions of laser-assisted milling of Si_3N_4	100

Acknowledgements

Over the past years I have had the opportunity to work with many extraordinary people - both inside and outside the Department - and have been blessed with a tremendous amount of support. I am grateful for the opportunity to thank them now.

First and foremost, I would like to thank my advisor, Professor Shuting Lei, who introduced me to the laser- related research, guided me in Ph.D. program, and continually supported and inspired me over these years. His broad knowledge and commitment to teaching excellence, student achievement and rigorous scholarship really impressed me.

I would also like to thank my committee members for their comments and suggestions on my dissertation. Thanks Professor Larry weaver (Chairperson) for his presence of my defense; Thanks Professor E. Stanley Lee and Professor David Ben-Arieh for their encouragement and great support; In particular, thanks Professor Zhongquan Charlie Zheng for his critical suggestions on my research.

I would also like to extend my most sincere thanks to Professor ZJ Pei. He constantly gave me valuable advice and significant support with his kindness, excellent research and abundant experience. Many thanks are also given to Professor Dr. Chih-Hang (John) Wu. He always emphasized my strengths and show great open-mindedness and warmth, and always made time for me whenever I needed any help. I would like to thank Professor Shing I. Chang. He provided me lots of useful and detailed suggestions on how to improve and complete the research. Particular thanks also go to Professor Zenghu Chang. He provided lots of brilliant ideas and valuable suggestions on my research.

I would also like to sincerely thank Department head Professor Bradley A. Kramer for his unchanging support and encouragement to me. I also thank the kind assistance from Mr. Timothy W. Deines and Professor Carl Wilson. Likewise, I also thank the other professors and staffs in the Department. I sincerely appreciate their help with everything. Without them, I probably would not achieve this goal.

I would also like to express my appreciation to my old friends: Dr. Budong Yang and Ms Lin Xu, Ms. Lian Li and Dr. Wangping Sun, Dr. Judong Shen, Dr. Jianmei Zhang and Mr. Ping Hu, Dr. Zhifeng Cheng and Ms. Xiujuan Feng, and Dr. Zhichao Li, and new friends: Ms Qiumei

Bian and Dr. Jianwei Liu, Mr. Yu Chen, Mr. Pengfei Zhang, Ms. Na Qin, and Mr. Weilong Cong, and many other friends for their concerns and invaluable support. In particular, I would like to thank Dr. Budong Yang and Ms. Qiumei Bian for the research cooperation and useful discussions.

I would like to give special thanks to my parents, my brothers, my mother-in-law and grandma-in-law for their unconditional love and continual support over the years. They always encouraged me to strive to be the best I could and to produce the best work I could. Last, but not least, I would like to thank my wife Qi Lu and my son Elvin. Without their support, patience, and encouragement, it is impossible for me to make it this far.

Nomenclature and Abbreviation

<p>$2D$ = two-dimensional</p> <p>$3D$ = three-dimensional</p> <p>a = precrack length, mm</p> <p>A = area of the bond cross section, m^2</p> <p>$ASTM$ = American Society for Testing and Materials</p> <p>AWJ = abrasive waterjet machining</p> <p>b = specimen thickness, width of specimen in orthogonal cutting, mm</p> <p>c = specific heat, $J/kg \cdot K$</p> <p>C_s = side cutting edge angle of the cutter, deg</p> <p>CDM = continuum damage mechanics</p> <p>CNC = computer numerical control</p> <p>CW = continuous wave</p> <p>d = maximum depth of subsurface damage, μm</p> <p>DOC = depth of cut, mm</p> <p>D_c = cutter diameter, mm</p> <p>D_l = laser beam diameter, mm</p> <p>DEM = distinct element method (or discrete element method)</p> <p>E_c = particle-particle contact modulus, GPa</p> <p>\bar{E}_c = parallel-bond modulus, GPa</p> <p>$ECDM$ = electrochemical discharge machining</p> <p>EDM = electrical discharge machining</p>	<p>EDS = Energy-Dispersive X-Ray Spectroscopy</p> <p>f = feed per tooth per revolution, mm/tooth/rev</p> <p>F_c = main cutting force in the cutting speed direction, N</p> <p>F_t = thrust cutting force, N</p> <p>F_y = cutting force in the y direction, N</p> <p>F_z = cutting force in the z direction, N</p> <p>\bar{F}_i = force vector between particles, N</p> <p>\bar{F}^n = scalar value of \bar{F}_i^n, N</p> <p>\bar{F}_i^n = normal component between particles, N</p> <p>\bar{F}_i^s = shear component between particles, N</p> <p>FDM = finite difference method</p> <p>FEA = finite element analysis</p> <p>FVM = finite volume method</p> <p>g = function of the ratio a/H for four-point fracture toughness test</p> <p>G_c = cutting energy from each cut, J</p> <p>h = convection coefficient, $W/m^2 \cdot K$</p> <p>\bar{h} = average convection coefficient of the model, $W/m^2 \cdot K$</p> <p>H = specimen height, mm</p> <p>H_w = workpiece height, mm</p> <p>HAZ = heat-affected zone</p> <p>HCP = hexagonal close-packed</p>
--	--

i = inclination angle of the cutter, deg
 I = moment of inertia of the bond cross section, m^4
 k = thermal conductivity, $W/m \cdot K$
 K_{Ic} = fracture toughness, $MPa \cdot m^{1/2}$
 k_n/k_s = particle stiffness ratio
 \bar{k}^n/\bar{k}^s = parallel-bond stiffness ratio
 L = specimen length, mm
 L_o = support span, mm
 L_c = cutting length, mm
 L_l = laser-cutter allowance, mm
 L_s = distance from the center of Point B to the top surface of the workpiece, mm
 L_t = distance from the center of Point A to the left end of the workpiece, mm
 L_w = width of the workpiece, mm
 LAM = laser-assisted machining
 $LAMill$ = laser-assisted milling
 LBM = Lattice Boltzmann method
 $LCSM$ = laser confocal scan microscopy
 LM = laser machining
 \bar{M} = elastic moment developing in the parallel bond, Nm
 MD = molecular dynamics
 MTP = minimum temperature point
 MRR = material removal rate
 n = unit normal vector
 n_i = unit normal vector
 N_c = cluster size
 N_f = minimum number of contacts to be a non-floater

N_f/N = remaining floaters ratio
 P = break load, N
 P_l = laser power, W
 PSZ = partially-stabilized zirconia
 $PCBN$ = polycrystalline cubic boron nitride
 q_{con}'' = convective heat flux, W/m^2
 q_{gen}'' = heat flux applied to the workpiece, W/m^2
 q_l'' = heat flux from laser source, W/m^2
 q_{rad}'' = radiation heat flux, W/m^2
 r = nose radius of the cutter, mm
 R_{av} = minimum particle radius, μm
 R_{max}/R_{min} = particle size ratio
 \bar{R} = bond radius, m
 RPM = revolution per minute
 RUM = rotary ultrasonic machining
 S = cutting length for simulation, mm
 S_1 = areas clamped with insulating materials, m^2
 S_2 = area covered by the laser beam (laser spot), m^2
 S_3 = areas where the cutter is in contact with the workpiece in one cut, m^2
 S_4 = areas including all the workpiece surfaces open to the surroundings excluding S_2 and S_3 , m^2
 SEM = scanning electron microscope
 t = time, s
 t_u = uncut chip thickness, mm
 t_p = preheat time, s

t_s = time for one step movement of laser spot, s
 $t_{u,e}$ = equivalent uncut chip thickness, mm
 T = temperature, °C
 T_c = average temperature of the cutting zone, °C
 T_s = surface temperature, °C
 T_∞ = ambient temperature, °C
 USM = ultrasonic machining
 vol = workpiece volume, m³
 V_c = cutting speed, m/s
 V_f = feed rate, mm/min
 V_l = laser moving speed, mm/min
 V_p = final velocity in numerical tests, m/s
 W_c = chamfer width of the insert, mm
 W_w = workpiece width, mm
 x, y, z = rectangular coordinates, m
 x, y', z' = rectangular coordinates, m
 $x_i^{[A]}$ = position vector of the center of particle A, m
 $x_i^{[B]}$ = position vector of the center of particle B, m
 $x_i^{[C]}$ = position vector of the contact point of two particles, m

Z = tooth number

Greek Letters

α = rake angle, deg
 α_e = equivalent rake angle of the cutter, deg
 β_c = clearance angle of the cutter, deg

β = volumetric thermal expansion coefficient, K⁻¹
 β_w = wall normal stiffness multiplier
 δ = square division of uniform elements, mm
 ε = emissivity of workpiece surface
 η = particle damping coefficient
 η_h = ratio of the cutting energy converted to heat
 η_w = ratio of the generated heat transferred to the workpiece
 θ_c = chamfer angle of the insert, deg
 $\bar{\lambda}$ = parallel-bond radius multiplier
 μ = particle friction coefficient
 ρ = density, kg/m³
 σ = Stefan-Boltzmann constant
 σ_o = locked-in isotropic stress, MPa
 σ_b = flexural strength, MPa
 $\bar{\sigma}_c$ = normal strength, MPa
 $\bar{\sigma}_{c,mean}$ = inter-cluster parallel-bond normal strength, mean, MPa
 $\bar{\sigma}'_{c,mean}$ = intra-cluster parallel-bond normal strength, mean, MPa
 $\bar{\tau}_c$ = shear strength, MPa
 $\bar{\tau}_{c,mean}$ = inter-cluster parallel-bond shear strength, mean, MPa
 $\bar{\tau}'_{c,mean}$ = intra-cluster parallel-bond shear strength, mean, MPa

Chapter 1 - Introduction

1.1 Motivation

As one kind of advanced structural ceramics, silicon nitride (Si_3N_4) has been increasingly used in a number of industrial applications, such as engine components, turbochargers, bearings, metal cutting and shaping tools, and hot metal handling, etc. It interests manufacturers and researchers for its high strength, hardness and fracture toughness, outstanding wear resistance, good chemical stability, low density and so on. The traditional and also commonly used technique for machining ceramics is grinding with a diamond wheel. But diamond grinding has low material removal rate (MRR), high machining cost, and surface/subsurface cracks which are extremely difficult to detect, thus strongly impeding the widespread use of ceramic components. Currently, there are some non-traditional ceramic machining techniques developed. They can be summarized as follows: ultrasonic machining (USM), electrical discharge machining (EDM), abrasive waterjet machining (AWJ), laser machining (LM), laser-assisted machining (LAM), plasma-assisted machining, single-point machining, electron-beam and ion-beam machining, microwave machining, and some hybrid machining. Among these non-traditional ceramic machining methods, LAM seems to be one promising technique due to its great potential to overcome the disadvantages of diamond grinding. In LAM, laser local heating can soften the material at the cutting zone and thus facilitates material removal by conventional machining operations such as turning or milling. However, up till now LAM is still in the stage of laboratory development and not applied in industry. The fundamental machining mechanism which governs the LAM process is not well understood so far, and as a result there is no effective guidance for parameter selection, especially how to avoid the surface/subsurface cracks and damage. Therefore, a deep understanding of the material removal mechanism in LAM is needed.

As one hybrid machining process, LAM combines laser technology with conventional machining operation, which involves two distinct processes: laser heating and material removal. In LAM, the laser is positioned in front of the cutter with the laser spot on the unmachined section of the workpiece. As the surface of the workpiece is subjected to the moving laser heat source, the laser energy absorbed by the workpiece is converted into heat, resulting in steep

thermal gradients and thermal stresses, which may cause surface/subsurface cracking in the workpiece. Furthermore, temperatures at the cutting zone are required to be within a proper range because, for LAM, underheating cannot decrease the hardness and strength of the material, and overheating may cause damage to the machined face and alteration of the material properties. Hence, laser intensity and moving speed should be carefully selected so as to ensure that the outer layer of the machined face at a defined depth of cut is not damaged, and at the same time the minimum temperature at the cutting zone is higher than the material softening temperature. Therefore, the analysis of temperature and thermal stresses is necessary and also very important for LAM. At present, one of the effective approaches to deal with this kind of problem is to establish a three-dimensional transient heat transfer model. Simulation with this model can provide distributions of temperature and thermal stress, and then identify with overly high or low temperatures, thus predicting the potential cracks. Also, a set of suitable operating parameters can be found and the expected temperature at the cutting zone can be achieved by adjusting the proper operating parameters, such as laser power, laser beam diameter, laser moving speed, and preheat time.

Moreover, once the cutter contacts the workpiece, the material removal begins. So far much of work has been reported on grinding mechanism, but there is little on LAM. As is known, silicon nitride is a temperature-dependent brittle material, and its properties, such as Young's modulus of elasticity, flexural strength, fracture toughness, etc., change with laser heating. Compared to metal cutting, ceramic machining exhibits a few distinct characteristics such as crack formation and uncontinuous chips. Simulation with a numerical model can help us discover the mechanism of crack formation and propagation, and explore the effects of machining parameters (e.g., depth of cut, feed, cutting speed) on cutting forces, cracks, etc.

In addition, as a hybrid process, LAM involves many operating parameters. These parameters can be classified into two groups: (1) parameters associated with laser and (2) parameters associated with machining. The former mainly includes preheat time, laser power, laser beam diameter, and laser moving speed. The latter mainly consists of cutter diameter, depth of cut, feed, cutting speed, and laser-cutter lead. In comparison with conventional machining, the selection of appropriate operating conditions is much more difficult, since both thermal and machining aspects should be considered. Hence, an effective and efficient strategy for parameter selection is strongly required.

1.2 Literature Review

1.2.1 Ceramic Machining

In the last three decades, an enormous interest in advanced ceramic materials emerged. However, due to the high cost of ceramic machining, the use of ceramic components is not as enormous as the interest. Currently, diamond grinding accounts for more than 80% of the total ceramic machining (Allor and Jahanmir, 1996), but there are still some other machining methods available. These methods include ultrasonic machining (USM), electrical discharge machining (EDM), abrasive waterjet machining (AWJ), laser machining (LM), laser-assisted machining (LAM), plasma-assisted machining, single-point machining, electron-beam and ion-beam machining, microwave machining, and combined machining. A brief introduction to each of the machining method will be given in this section.

Diamond grinding is by far the most widely used traditional method in industry. One problem of diamond grinding is that the machining cost constitutes 30% to 60% of the total cost and for some high-precision components even as high as 90% (Wobker and Tonshoff, 1993). The other problem for grinding ceramics is the lack of experience with diamond tooling and insufficient machine-tool stiffness, thus generating small subsurface cracks that are extremely difficult to detect (Allor and Jahanmir, 1996). These small subsurface cracks can seriously decrease the strength of the machined parts (Sheppard, 1990; Gou and Chand, 1995). So far, much work has been done to improve the grinding process. For example, some researchers (Mayer and Fang, 1993; Saurwalt, 1993) found that the surface damaged area is associated with wheel grit size. The smaller the grit size, the more ductile mode appearance in machining and the less damage on the machined surface. Some researchers (Wang and Hsu, 1994; Zhang and Jahanmir, 1996; Yin et al., 2003) found that the appropriate choice of grinding fluid chemistry can improve material removal rate and decrease grinding damage. The grinding fluid can keep the cutting point and ceramic workpiece at lower temperatures during machining, and thus the machining-induced damage in the workpiece surface can be reduced. Some researchers (Sheppard, 1987; Bifano et al., 1988; König and Wageman, 1993; Rice, 1993; Ives et al., 1993) concluded that a ductile regime takes place on a localized scale when the grit penetration is limited to a small size, and in this ductile manner there is a decrease in the subsurface damage. But this ductile-regime grinding requires low and precise feeds, very small grit depths, and

extremely low material removal rate (MRR). Some researchers tried to improve the grinding equipment. For instance, Shen et al. (2001) applied water-jet to dress diamond wheel and developed a precision surface grinding technique to cut Al_2O_3 ceramics and achieved high efficiency and surface finish.

Another prominent method successfully used in industry is ultrasonic technique. Ultrasonic machining (USM) is an abrasive process, and also called ultrasonic impact grinding (Moore, 1986) and ultrasonic abrasive machining (Schwartz, 1992). Based on mechanical oscillation of an abrasive slurry, USM uses the vibrating tool (sonotrode) to reproduce its shape into the hard and brittle material. USM does not generate a heat affected zone or cause any chemical/electrical alternations on workpiece surface, and can produce almost any complicated 3D shapes with economical material removal rates (Hahn et al., 1993; Sadat, 1999). However, the fresh slurry has to be supplied and removed from the gap between the cutting tool and the workpiece, and thereby may wear the wall of the machined hole. Moreover, the movement of the abrasive slurry will damage the cutting tool. In addition, research (Iwanek et al., 1986; Pei, 1995) observed that once the fracture toughness of ceramics or penetration depth increases, the efficiency of USM has a large decrease. To overcome the shortcomings of USM, rotary ultrasonic machining (RUM) was developed which combines the material removal mechanisms of USM and diamond grinding. The slurry is replaced with abrasives bonded to the tool, and coolant is used to wash away the swarfs and prevent jamming the drill (Pei, 1995). RUM can increase the material removal rate (MRR) and improve the hole accuracy (Treadwell and Pei, 2003). However, a commercial RUM machine is only limited to machining circular holes.

Electrical discharge machining (EDM) is a non-abrasive technique, which is especially important for machining hard, brittle, and high-melting-point materials (Faulk, 1993). In EDM, the material removal rate is strongly influenced by the electrical and thermal properties of the workpiece rather than by the hardness, brittleness of the work material (Faulk, 1993; Tuersley, 1994; Sadat, 1999; Sanchez et al., 2001). The main advantage of EDM in ceramic machining is its ability to produce complicated shapes, no mechanical residual stresses on the workpiece, and relatively high material removal rate. The main disadvantage is that this method is only limited to conductive materials with electrical conductivity over 0.01 S cm^{-1} (König et al., 1988). For ceramic materials with low electrical conductivity, EDM can be used if some doping is added to the ceramic material to improve its conductivity. For example, Martin et al. (1989) added TiB_2

particles to SiC and TiN particles to Si₃N₄, and Lee and Lau (1991) added TiC particles to Al₂O₃. Although this kind of material can be machined by EDM, the temperature is limited to about 1000 °C due to the onset of oxidation of the metallic phases beyond that point. For non-conductive ceramic materials, electrochemical discharge machining (ECDM) can be used. Electrochemical discharge machining (ECDM) is a combination of thermal and chemical machining for ceramic materials, which is influenced by various process parameters such as the applied voltage, the interelectrode gap; the temperature, concentration and type of electrolyte; the shape, size and material of the electrodes, and the nature of the power supply, etc. (Bhattacharyya et al., 1999; Lim et al., 2001; Fukuzawa et al., 2002; Wuthrich and Fascio, 2005; Sarkar et al., 2006). But now the main challenge is to control the gas film built around the two-electrode in which the discharges happen, and to find the stability and dynamics of this film conditions.

Abrasive waterjet (AWJ) machining uses a high-pressure waterjet mixed with abrasive particles, such as garnet or silica sand, to cut or drill the hard materials. The quality of the cut area and the material removal rate are associated with the abrasive material, abrasive particle size, nozzle dimension, and waterjet pressure and velocity (Tuersley, 1994). In AWJ, there are no thermal stresses, low machining forces on the workpiece, and no cutting tool degradation (Guo and Ramulu, 2001). The disadvantages are stray cutting, low nozzle life, high noise level and equipment cost, hazards from rebounding abrasives (Jain et al., 2001), and low machining precision (Guo, 1998).

Laser machining (LM), also called laser beam machining, is a non-contact process, and thereby has no tool wear, cutting forces and tool deflections. Lasers can be easily automated and adapted to a flexible manufacturing system. It can be used as a complementary process to the traditional diamond grinding especially in high speed machining of complicated shapes and geometries. However, laser machining can reduce material strength (Sheppard, 1987) and decreases micro-hardness, flexural strength, and fracture toughness (Lavrinovich et al., 1990). The machined surface usually does not have good properties as the abrasively machined one (Ito et al., 1987).

In order to take advantages of the various methods of ceramic machining mentioned above, some combined machining processes were developed. For example, Uematsu et al. (1988) applied ultrasonic grinding and electrical discharge grinding to an electrically conductive

ceramic workpiece, and found that the new complex grinding method could remarkably reduce grinding force and increase material removal rate in ceramic material TiB_2 . Jia et al. (1995) used ultrasonic machining (USM) along with electrical discharge machining and demonstrated that this technique can obtain high efficiency and surface integrity for conductive hard and brittle materials. Zhang et al. (1996) combined diamond wheel grinding with electrical discharge machining (EDM) for ceramics and concluded that both the machining efficiency and the part quality are increased.

The single-point turning operation for ceramic machining was also studied in laboratory. Kiso et al. (1987) found that turning with sintered polycrystalline diamond tool is a promising machining process for ZrO_2 , but not for Si_3N_4 because of short tool life. Various researches (Strenkowski and Hiatt, 1990; Blackley and Scattergood, 1991; Zhao et al., 1998; Beltrao et al., 1999; Ajjarapu et al., 2004) investigated that, in single-point turning, there is a critical-depth parameter which defines the transition from brittle to ductile behavior in the machined workpiece surface, and in this ductile manner the sub-surface damage can be reduced.

In addition, there are some other machining methods in some particular applications. For example, electron-beam machining (Spector, 1977; Desilets, 1978; Sarfaraz et al., 1993) was used to drill holes or mill pockets in ceramics; ion-beam machining (Clinton, 1971; Miyamoto et al., 1984) was applied to obtain fine machining of ceramic surfaces; microwave machining (Jerby et al., 2003) was employed to micro-pierce or drill ceramic materials.

1.2.2 Laser-Assisted Machining of Ceramics

Laser-assisted machining (LAM) is one kind of hot machining (König and Zaboklibki, 1993) or thermally assisted machining technique (Shin et al., 2000) in which the materials are heated by an external energy source and then machined. The purpose to heat materials is to enhance their machinability, especially for “difficult to machine” materials. Plasma-assisted machining is another kind of hot machining, which combines plasma arc technique with conventional machining operations. For example, Poduraev et al. (1989) applied plasma-assisted machining to cut high-strength steels and alloys and found that the production rate and accuracy of machining were considerably increased. Miyasaka et al. (1991) used plasma arc to heat a Si_3N_4 workpiece over $1000^\circ C$ and successfully cut with turning operation.

In comparison to plasma arc, laser can generate higher temperatures at the cutting zone of

the workpieces for its intense and highly localized energy source, thus more and more “difficult to machine” materials were machined with laser assistance, such as tool steels (Koshy et al., 2006; Singh and Melkote, 2007), stainless steels (Bass et al., 1979; Copley, 1985; Jeon and Pfefferkorn, 2005; Anderson and Shin, 2006), hardened steels (Jen et al., 2004; Sakai, et al., 2005) and alloys (Bass et al., 1979; Jau et al., 1981; Rajagopal, 1982; Copley, 1985; König and Zaboklicki, 1993; Shin et al., 2006; Germain et al., 2006).

From the 1990's, researchers began focusing on ceramics. König and Zaboklicki (1993) first studied laser-assisted turning of silicon nitride with Nd:YAG laser. They found that as the laser power is fixed, with cutting speed increasing, the surface temperature rises and the cutting forces decrease. The machined surface has good quality ($R_z < 3 \mu\text{m}$ and $R_a < 0.5 \mu\text{m}$). The tool wear modes are mainly flank wear, crater wear on the tool face, and rounding of the cutting edge. Chip morphology shows that plastic deformation controls the chip formation in hot machining.

Hibi et al. (1995) utilized an excimer laser to irradiate a SiC ceramic in deionized water. It was indicated that laser heating facilitates the formation of a soft hydrous oxide layer by photochemical reaction, thus enhancing machining effectiveness with a diamond tool. The machined surface has a mirror surface finish without brittle fractures and excess laser ablation.

Westkämper (1995) applied Nd:YAG laser in grinding silicon nitride ceramics. It was noted that the use of laser assistance is to reduce the thermal gradients during grinding. Comparing with grinding tests with and without laser assistance, the author concluded that the applied heat energy has no significant influence on the grinding forces, but the feed of diamond roller during truing can be reduced and in-feed depth of the grinding wheel increased and there is no crack occurring. The surface roughness of the machined workpiece is almost the same as that of without assistance ($R_z = 2.5 \mu\text{m}$).

Marinescu (1998) employed a diode laser in laser-assisted grinding of ceramics including Al_2O_3 , Ferrite, ZrO_2 and Si_3N_4 . It was found that heating ceramic materials can help the material removal process and the surface quality is also improved. Through some chips collected, the author presumed that the material removal is achieved through partly brittle fracture and partly plastic deformation.

Janvrin (1996) reported on the results of laser-assisted turning of silicon nitride ceramics with both carbide and coated carbide tools. It was found that with the assistance of Nd:YAG laser, coated carbide tool can provide better machining of silicon nitride since the thermal barrier

coating can reduce the tool wear and increase the tool life. Analyzing the machined samples by SEM, the author pointed out that both the grains and grain boundaries of silicon nitride are softened in hot machining at higher temperatures. The softening of grain boundaries can provide a built up edge so as to protect the insulated coated tool edge from wearing. Also the built up edge can fill surface imperfections and cracks, and thus resulting in a very smooth surface on laser-assisted turning of silicon nitride.

Rozzi (1997) conducted a study with CO₂ laser to evaluate laser-assisted turning of silicon nitride. It was found that if the temperatures at the cutting zone fall below the YSiALON glass transition temperature (920-970 °C), there will be significant tool wear or tool failure. With the temperatures at the cutting zone increasing, the types of chip change from small, fragmented chips to large continuous chips, which suggests deformation from brittle fracture to plastic flow. Also, increasing temperature can facilitate the movement of softened glassy material in the silicon nitride and reduce cutting forces and tool wear drastically.

Lei et al. (2001) performed some experiments with CO₂ laser assistance on turning of silicon nitride. They indicated that tool wear mainly happens on the flank face and crater wear on the rake face is so small that it can be neglected, and the dominant mode of tool wear is adhesion. The thickness of the affected layer of the workpiece (2-4 μm) is considerably smaller than that in grinding. They proposed that material removal in LAM is: (1) from a workpiece surface layer by laser heating due to oxidation, melting and vaporization, (2) from machining by a cutter with plastic deformation in the shear zone, and (3) from segmented chips due to initiation, coalescence and propagation of intergranular microcracks.

Rebro et al. (2002) investigated laser-assisted turning of mullite ceramics using CO₂ laser and reported that the specific cutting energy is reduced by 30% and 40% at the laser power of 170 W and 190 W, respectively, and has little dependence on depth of cut, laser beam diameter and laser-tool lead. From the chip morphology, they explained that the chip formation is associated with material removal temperature (T_{rm}) and cutting force ratio (ratio of the feed force to the main cutting force, F_f/F_c), which can be summarized as: for combined brittle fracture and semi-continuous chip formation, $F_f/F_c > 1$ and $800\text{ °C} < T_{rm} < 1000\text{ °C}$; for semi-continuous chip formation, $F_f/F_c < 1$ and $1000\text{ °C} < T_{rm} < 1300\text{ °C}$, and for continuous chip formation, $F_f/F_c < 1$ and $T_{rm} > 1300\text{ °C}$. The surface roughness of machined workpiece ($R_a=2.8\text{ μm}$) has great improvement for a laser power of 210 W compared with that of 0 W ($R_a=5.9\text{ μm}$). The tool life

is in the range of 40 minutes and has a significant increase compared with that without laser assistance and comparable to those found in metal cutting operations. The surface roughness is very close to that of the ground surface. Also, they conducted comparative assessment of mullite, partially-stabilized zirconia (PSZ), and silicon nitride in laser-assisted turning. Due to different thermophysical and mechanical properties of these three kinds of ceramics, mullite and silicon nitride were heated gradually and PSZ was heated with a constant laser power. They found that mullite is machinable with a carbide cutter, whereas silicon nitride and PSZ require cubic boron nitride insert. Experimental results show that above a sufficient material removal temperature, continuous chips occur in silicon nitride and mullite while PSZ only has fragmented chips. The surface roughness of all these three ceramics is close to that of grinding without visible subsurface cracks.

Tian and Shin (2006) employed CO₂ laser to perform laser-assisted turning of silicon nitride workpiece with complex features. Due to the variations of the geometric features of the workpiece, the laser power was correspondingly regulated according to the surface temperatures measured. They found that the cutting forces in LAM are strongly influenced by the material removal temperature and the specific cutting energy is significantly determined by size effect. As depth of cut and undeformed chip thickness decrease, specific cutting energy increases. They also noted that compared with the tool life found by Lei et al. (2001) the tool life becomes longer, and the machined workpiece has good finish surface, moderate compressive residual stress, and no thermal damage and phase transformation from β -Si₃N₄ to α -Si₃N₄. Tian et al. (2006) further studied laser-assisted milling of silicon nitride. The cutter was TiAlN coated solid carbide end mill with two flutes. They found that the machined surface by milling also has a good finish and no cracks. The tool wear rate is strongly associated with laser power. With the lowest laser power (1000 W), the tool wear is very fast. As the laser power increases, the tool wear considerably reduces. But once the laser power reaches 1300 W, more wear with chipping on the tool is observed. They reported that the TiAlN coated carbide cutters at material removal temperature from about 1200 °C to 1300 °C do not have a good life.

In order to investigate the machining mechanism of laser-assisted milling of silicon nitride ceramics, Yang et al. (2007) did a series of experiments with a diode laser and a self-made cutter which has only one tooth and one polycrystalline cubic boron nitride (PCBN) tipped insert. They found that with increasing cutting temperature, both the cutting forces and specific

cutting energy decrease. When temperature at the cutting zone increases from 838 °C to 1319 °C, the tangential force and radial force decrease by about 50% and 45%, respectively. With temperature high enough to soften the glassy grain-boundary phase, laser-assisted milling shows more plastic deformation. Once the temperature is higher than 800 °C, no entry edge chipping and interior edge chipping occurs and the size of exit edge chipping decreases greatly.

Chang and Kuo (2007) analyzed laser-assisted planing as well as turning of Al₂O₃ ceramics with the help of a CO₂ laser. In planing, their experimental results showed that the cutting force is reduced by about 10-16% compared with conventional machining. The machined workpiece has a better finish (2.98 μm) and tool wear is relatively reduced. In turning, they indicated that the smaller the tool wear at the cutting edge, the better the surface quality. Similar to planing, the cutting force is considerably reduced and good surface roughness is achieved.

1.2.3 Models for Laser-Assisted Machining of Ceramics

Thermal Model

Laser heating can cause material softening, local yielding, melting, burning, or evaporation. The different material removal methods determine the difference of laser heating in laser machining and laser-assisted machining. Generally speaking, laser machining needs high temperature to achieve material removal and it is accompanied with phase change from solid to fluid or vapor, and/or plasma generation. While in laser-assisted machining, the laser is used as an intense heat source to change the material's behavior from brittle to ductile, and phase change mainly occurs for a small part of the material on a workpiece surface (Lei et al., 2001). Since the laser heating is a complicated process in laser machining, more assumptions are applied than those in laser-assisted machining. For example, Atanasov et al. (2001) developed a one-dimensional analytical heat transfer model to describe laser drilling of silicon nitride and alumina ceramics. They indicated that the plasma absorption formed during drilling should be taken into account, and when the plasma absorption was considered, the theoretical results agreed well with the experimental ones. Roy and Modest (1993) built a three-dimensional model with finite difference method. This model was used to predict the groove shapes and temperature distribution during evaporative scribing of a silicon nitride workpiece subject to a moving CW laser. They assumed that phase change from solid to vapor occurs in a single step at the evaporation temperature. They further noted that real materials may display significantly

different behavior such as liquefaction followed by evaporation, decomposition into liquid and gas, gradual evaporation over a wide range of temperatures, outgassing followed by microexplosive removal of solid particles, etc.

At present, a few methods are used to develop the thermal models of laser-assisted machining, such as analytical method, lattice Boltzmann method (LBM), finite volume method (FVM), finite difference method (FDM) and finite element analysis (FEA). The following will give a literature review on the models of laser-assisted machining associated with these methods.

Janvrin (1996) developed a three-dimensional heat conduction model of laser-assisted turning of silicon nitride without material removal. The distribution of laser intensity used was uniform and the absorptivity of silicon nitride was 0.7. In order to simplify the model and obtain a solution of the governing differential equations, it was assumed that there was no change of temperature on the workpiece surface where the laser beam covers, thereby making the variable in r -direction being eliminated. Additionally, radiation and convection to the surroundings are neglected, and the thermal conductivity and specific heat of the workpiece are kept constant during laser heating. An explicit finite difference method (FDM) was applied to solve the governing equations. The objective of developing the model was to find optimal turning speeds for different values of depth of cut. Unfortunately, there is no model validation in his study and no publications could be found.

Gutierrez and Araya (2004) also developed a transient three-dimensional conduction model for laser-assisted machining of silicon nitride ceramics. The boundary conditions had the same assumptions as Janvrin (1996): constant thermal properties, and no radiation and convection. No material removal was considered and no validation was included in the model. The difference is that Gutierrez and Araya assumed that all the energy from the laser source was absorbed by the workpiece, namely, the absorptivity of the material is 1.0 and Janvrin estimated it to be 0.7. Gutierrez and Araya obtained an analytical solution through the method of separation of variables while Janvrin used finite difference method.

Similar to Janvrin (1996) and Gutierrez and Araya (2004), Chang and Kuo (2006) established a transient heat conduction model for laser-assisted machining without considering radiation and convection, and validated the model through experiments. In this two-dimensional model for planing of Al_2O_3 ceramics, lattice Boltzmann method (LBM) was used to calculate the temperature distribution inside the ceramic workpiece. Through this model they found that the

surface temperature reaches to 850 °C in 4 s, which explains why, given appropriate irradiation of laser power, the workpiece surface can be softened quickly and efficiently. They also calculated the perpendicular temperature distribution in order to ensure that intense heating will not damage the subsurface from the workpiece surface. For example, at a depth of 0.1 mm, the temperature rapidly decreases to less than 100 °C, which means that the high temperature caused by the laser power has little effects on the sublayer.

Rozzi (1997) developed a transient, three-dimensional thermal model for laser-assisted turning of silicon nitride with and without material removal, respectively. Compared with the model by Janvrin (1996), Rozzi considered radiation and convection of the workpiece and also treated thermal conductivity and specific heat temperature dependent. In fact, silicon nitride ceramics are temperature-dependent materials and their properties of conductivity and specific heat vary with temperature (Hampshire, 1991; Smotriskii et al., 1996). The fully implicit finite volume method (FVM) was applied to discretize the energy equation and the computational domain was divided into a set of nonoverlapping control volumes. The model was validated through comparing the simulation results with experimental ones. In validation, the surface temperatures of 5 special points were measured. The author reported that the effect of rotational speed on the surface temperature distribution decreases with increasing circumferential location from the laser spot and near-laser temperatures decrease with increasing beam diameter, decreasing laser moving speed or laser power. Also, parametric effects were conducted including workpiece rotational speed and laser moving speed on temperature distribution, and thermophysical properties and surface thermal conditions on the maximum temperature within the laser spot. It was concluded that the thermal layer thickness decreases with increasing the workpiece rotational speed. The forced convection associated with a gas assist jet and changes in thermophysical properties can considerably influence the maximum surface temperature beneath the laser spot. In addition, an approximate model was developed in order to calculate the radial temperature distribution at various circumferential locations, and then obtain the simplified relations for on-line control of the laser-assisted machining process. In 1998, Rozzi et al. published two important papers, and they were the first group that successfully analyzed the temperature distributions of the laser-assisted turning through a numerical model.

Based on the model developed by Rozzi (1997), Rebro et al. (2004) modified this model to study mullite ceramic. Since silicon nitride and mullite are two different kinds of ceramics,

they analyzed the thermophysical properties of mullite in detail including density, thermal conductivity, specific heat, spectral emissivity and absorptivity. Axial and radial thermal gradients were evaluated through this model and also validated by comparing the predicted temperature and measured ones. They noted that the thermal diffusivity of mullite is roughly one-third that of silicon nitride. Due to its relative inability to conduct thermal energy, mullite would develop much higher thermal gradients during laser heating and thus operating conditions were different with those of Rozzi's (1997). By comparing laser-assisted turning with constant, one-ramp and two-ramp laser powers, they found that the method with two-ramp laser power consistently avoided thermal fracture and crack formation.

Pfefferkorn et al. (2005) extended Rozzi's model to partially-stabilized zirconia (PSZ) ceramics. Both discrete ordinate method and diffusion approximation, respectively, were used to account for the internal radiation inside the semi-transparent workpiece. They indicated that laser power, feed and depth of cut have considerable impact on the temperature distribution, and thus these three parameters were the most concerned in model validation. In addition, a parametric study was performed on laser power, feedrate, depth of cut, spindle speed, laser diameter, and preheat time. They concluded that surface temperature is almost linearly varied with laser power. Higher feedrate results in less energy absorption. Depth of cut has a significant effect on the material removal temperature. Surface temperature decreases with increasing spindle speed and the effect of variation in spindle speed are larger near the workpiece surface than at the depth of cut. Surface temperature increases as laser diameter decreases. Increasing preheat time increases the amount of energy deposited in the workpiece and temperature at the initial position.

Since Rozzi's thermal model is only suitable to a straight cylindrical workpiece with a constant machined diameter along the axial direction, Tian and Shin (2006) modified the model to adapt to complex features. The workpiece was in straight cylindrical shape with a round-cap end before machining. The machined workpiece was produced with a 4 mm straight cutting at a constant depth of cut of 0.7 mm and a 20 mm sinusoidal cutting with wavelength of 16 mm and varying depth of cut between 0.2 mm to 1.2 mm. They validated the modified model through the variations of laser power, spindle speed and feed, respectively, and pointed out that laser power has the most significant influence on the workpiece temperature. Spindle speed has little influence on the steady state maximum temperature at the measurement centerline. Feed has much larger influence on the workpiece surface temperature than spindle speed and much less

than laser power. Also, they pointed out that among all the uncertainty factors such as laser absorption, feed, spindle speed, CO₂ laser power, workpiece surface properties and cutting energy, the major one is from the workpiece absorptivity. Tian et al. (2006) again extended Rozzi's model to laser-assisted milling and the material was sintered reaction-bonded silicon nitride. They noted that since the properties of sintered silicon nitride and sintered reaction-bonded silicon nitride have almost identical chemical composition and microstructure, the properties of the former were used as those of latter. The model was validated through comparing surface temperature measurement as the laser power varied.

Westkämper (1995) developed a special finite element analysis (FEA) model for laser-assisted grinding of silicon nitride, but detailed description of the model was not given. Two kinds of materials were considered in the study: silicon nitride and steel (90MnV8). The ceramic workpiece has almost the same thermal conductivity of the steel, twice the specific heat and 30 times of the thermal expansion coefficient. As a result, the ceramic workpiece had a slightly higher peak temperature and was more likely to generate grinding cracks due to the low ductility.

Machining Model

Ehmann et al. (1997) gave a good summary on machining process modeling, especially for metal cutting. They classified dynamic cutting process modeling into analytical, experimental, mechanistic, and finite element methods. Material removal mechanism in brittle materials, however, usually shows brittle fracture or a hybrid of plastic deformation and brittle fracture. So far, only a few studies found in the literature deal with modeling for brittle materials. The modeling methods for brittle materials are mainly focused on finite element analysis (FEA), molecular dynamics (MD) and distinct element method (DEM).

Zhang and Cao (2000) developed a finite element model to simulate the material removal process of glass ceramics and applied the theories of contact mechanics and fracture mechanics to formulate it. They found that strength degradation of a machined product occurs after machining. The model can be used to assess the microcracks embedded beneath the machined surface and evaluate the surface integrity. Promotion of shear-driven quasi-plastic deformation during machining improves surface quality and reduces the depth of damage layer formed during machining.

Kumbera et al. (2001) concluded research on a two-dimensional finite element model

with a commercial package ADVANEDGE for orthogonal cutting of silicon nitride. This model incorporates power-law strain-hardening, thermal softening and rate sensitivity, and uses adaptive remeshing technique to overcome excessive element distortions. They noted that silicon nitride ceramics behave in a ductile fashion under high pressures and when depths of cut are very small. The primary objective of developing the model was to study the effect of various process parameters on the pressure distribution within the workpiece and find operating conditions under which ductile regime machining is possible. Therefore, a parametric study was conducted to investigate the effects of cutting speed, tool-tip radius, rake angle and feed. It is reported that when the feed, tool-tip radius and cutting speed are small, conditions of brittle-to-ductile transformation of silicon nitride exist. Negative rake angles are also more likely to promote transformation than positive rake angles. Based on Kumbera's model, Ajjarapu et al. (2004) replaced the Mises yield criterion with the Drucker-Prager yield criterion, and found that when the depths of cut are small and the pressure in the workpiece approaches the hardness value of silicon nitride in the region near the workpiece-tool interface, material transition to ductile mode occurs in this region. As the cutting speed increase, thermal effects become more and more dominant and inelastic deformation of silicon nitride will increase due to thermal softening.

Liu and Zhang (2002) incorporated continuum damage mechanics with finite element analysis to predict workpiece subsurface damage induced in ceramic grinding. The model consists of a set of parallel Maxwell-type elements arranged in series with a spring. It not only considers the respective contributions of the volumetric and deviatoric stresses, but also the coupling effect between the stresses on damage development. They reported that the model can satisfactorily predict damage depth and give a reasonable prediction of lateral damage, and the machining direction has an important influence on the distributions of damage and residual stresses.

Tian and Shin (2007) established a multiscale finite element model to simulate the chip formation in laser-assisted machining of silicon nitride ceramics. The silicon nitride workpiece was modeled with hexagonal cells of continuum elements imbedded in thin interfacial cohesive elements. A hexagonal cell represents a cluster of silicon nitride, which consists of silicon nitride grains and the intergranular glass phase inside the cell. These cells of silicon nitride are connected by four-node cohesive interfacial elements, which are governed by a cohesive model to simulate the potential crack formation between the continuum cells. Their simulation results

show that the chip formation and machined surface generation are dominated by different mechanism. The formation of discontinuous chips is caused by the propagation of cracks in the shear zone while only a small amount of deformation occurs in the chips. In addition, they pointed out that the machined surface is generated by plastic deformation of the workpiece material under confined high pressure, which results in a crack-free subsurface.

Komanduri et al. (2001) performed molecular dynamics (MD) simulations of nanometric cutting of single-crystal, defect-free, pure silicon and investigated the nature of material removal and surface generation process in ultraprecision machining and grinding. They noted that the essence of the MD simulation method is the numerical solution of Newton's equations of motion for an ensemble of atoms. In MD simulation, the workpiece is divided into three different zones: the moving zone, the peripheral zone and the boundary zone (Chandrasekaran, 1997). The motion of the atoms in the moving zone is only determined by forces produced by the interaction potential and the direct solution of classical Hamiltonian motion equations. The motions of the peripheral zone are modified by the presence of the velocity reset functions associated with each atom in the peripheral zone. The boundary atoms are fixed in position and serve to reduce the edge effects and maintain proper symmetry of the lattice. Molecular dynamics (MD) simulations are usually used in ultraprecision machining.

Another method applied in machining simulation is distinct element method (DEM). The DEM was first introduced by Cundall for the analysis of rock-mechanics and then applied to soils (Cundall, 1971; Cundall, 1981). One commercial package, PFC^{2D} (Itasca Consulting Group, Inc., 2002), can model the movement and interaction of circular particles by the distinct element method. In PFC^{2D}, a rectangular specimen containing densely-packed, circular particles is generated and the particles are rigid and bonded together to form a solid. The interaction of the particles is treated as a dynamic process with states of equilibrium developing whenever the internal forces balance. Huang (1999) used PFC^{2D} to model the rock material. Lei and Kaitkay (2002) and Kaitkay (2002) used it to simulate rock cutting and found that the cutting forces from the simulation agree well with the experimental results. Lei and Yang (2005) applied it to simulate ceramic machining and indicated that the material removal in ceramic machining is mainly realized by brittle fracture and most cracks are initiated close to the cutting tool. Both the median and lateral cracks are very similar to the cracks observed in the experiments. A summary of the main methods and studies in machining modeling of brittle materials is given in Table 1.1.

Although they have achieved various degrees of success in machining simulation of brittle materials, there are some disadvantages associated with each method.

Table 1.1 Limitations in machining models for brittle materials

Authors	Model	Material Type	Limitations
Zhang and Cao (2000)	FEA	Continuum	The method does not show how the cracks propagate and how the cutting forces influence the cracks.
Kumbera et al. (2001) Ajjarapu et al. (2004)	FEA	Continuum	The method is based on the ductile machining of ceramics and needs to find the operating conditions of ductile machining. High pressures and very small depths of cut are required, thus having low material removal rate (MRR).
Liu and Zhang (2002)	FEA	Continuum	The method can only predict damage depth and lateral damage, and cannot show the crack formation and propagation and cannot analyze the surface integrity.
Tian and Shin (2007)	FEA	Continuum	The authors only showed the first and second cracks with a too short cutting length. They used average forces over 5 mm cutting length to compare with the measured ones, and did not show variations of the crack formation and propagation with the cutting forces in a continuous mode. In addition, the surface integrity is not evaluated.
Komanduri et al. (2001)	MD	Noncontinuum	The method is applied mainly to nanometric cutting. Due to the long processing time, the cutting speed used is extremely high (500 m/s), which is somewhat unrealistic.
Lei and Yang (2005)	DEM	Noncontinuum	The authors did not apply the fracture toughness test to evaluate the properties of the synthetic material, and did not consider the effects of cutting forces on crack formation and propagation, and surface integrity.

1.3 Objectives of This Research

The major limitation listed in Table 1.1 for the existing models is the lack of treatment of the material microstructures. As is known, the thermal-mechanical dynamic behavior of the brittle materials, such as in LAM, is controlled by their microstructures (Rühle, Manfred, 1985; Lee and Rainforth, 1994). That is, simulations without microstructural modeling cannot fully reveal machining characteristics like material removal, and crack formation and propagation. Although Tian and Shin (2007) made an improvement for FEA by imbedding thin interfacial cohesive elements in continuum elements as the intergranular glass phase in silicon nitride and thus successfully simulated the chip formation, the model still does not reflect the actual microstructure of the material, especially grain shapes.

However, the distinct element method (DEM) is an effective approach to model the microstructures of brittle materials at grain level. The DEM treats a brittle material as an assembly with densely packed and arbitrarily sized circular particles bonded together. When the bonds break, cracks form or propagate. For silicon nitride ceramics, particle clusters can be used to model the real grain shapes. The bonds among clusters can be used to simulate the intergranular glass phase. Moreover, the material removal and crack formation and propagation can be achieved through bond breaking.

Hence, the objectives of this research are as follows:

- (1) To develop and validate a three-dimensional (3D) transient thermal model with FEA, thus accomplishing the temperature control at the cutting zone in the workpiece.
- (2) To develop a two-dimensional (2D) machining model with the DEM to simulate the material removal process of laser-assisted machining, and then validate it through comparing simulation results with experimental ones.
- (3) To provide guidelines on parameter selection for future laser-assisted machining from experimental, thermal and machining aspects.

1.4 Organization of Dissertation

In chapter 2, the operating temperature of laser-assisted machining (LAM) of silicon nitride ceramics is investigated through heating and machining experiments, respectively. Guidelines on parameter selection for LAM are provided according to laser-silicon nitride interaction mechanism, effect of parameters on temperature, and evaluation of surface quality of

the machined workpieces.

Chapter 3 focuses on the temperature prediction using a three-dimensional (3D) transient finite element thermal model. The model development and validation are introduced in detail. Guidelines on parameter selection from thermal aspect are provided.

Chapter 4 elaborates the creation process of the synthetic material used for machining simulation, and finally gives the dimensional requirements for a reasonable specimen.

Chapter 5 concentrates on the establishment of the DEM machining model. Guidelines on parameter selection from machining aspect are provided.

Chapter 2 - Experimental Study on Operating Temperature in Laser-Assisted Machining of Silicon Nitride Ceramics *

Operating temperature plays a significant role in laser-assisted machining (LAM) of silicon nitride ceramics. Understanding the features of temperature variation in LAM can improve the machining process. Note that laser-assisted milling (LAMill) will be focused in this study. In this chapter, the investigation of operating temperature will be conducted through heating and machining experiments, respectively. Guidelines on parameter selection for LAM will be provided from the following aspects: laser-silicon nitride interaction mechanism, effect of parameters on temperature, and evaluation of surface quality of the machined workpieces. First, the laser-silicon nitride interaction mechanism is explored via heating experiments. Then, the trends of temperature variations in LAM are obtained through a parametric study. At last, the surface quality of the machined workpieces under different operating temperatures is evaluated in terms of edge chipping, surface finish and surface residual stress.

2.1 Introduction

From the 1990's, researchers in laser-assisted machining (LAM) began to focus on advanced ceramics. König and Zaboklicki (1993) first studied laser-assisted turning of silicon nitride and found that the cutting forces decrease as the surface temperature rises. Westkäemper (1995) applied a Nd:YAG laser in grinding silicon nitride ceramics to reduce the temperature gradients during grinding. Marinescu (1998) also conducted laser-assisted grinding of ceramics and pointed out that laser heating can facilitate the material removal process and improve the surface quality. Rozzi et al. (1998) evaluated laser-assisted turning of silicon nitride and concluded that increasing temperature can drastically reduce cutting force and tool wear. Through experiments of laser-assisted turning of silicon nitride, Lei et al. (2001) found that the dominant mode of tool wear is adhesion, which depends on workpiece temperature. Rebro et al.

The contents of this Chapter are from my following journal paper:

* **Shen, Xinwei** and Lei, Shuting (2010). Experimental study on operating temperature in laser-assisted milling of silicon nitride ceramics. *International Journal of Advanced Manufacturing Technology* (in press, DOI: 10.1007/s00170-010-2702-7)

(2004) reported that the chip formation in laser-assisted turning of mullite ceramics is associated with material removal temperature and cutting force ratio. Pfefferkorn et al. (2004) indicated that high material removal temperature can reduce the specific cutting energy, improve tool life in laser-assisted turning of partially-stabilized zirconia. Tian and Shin (2006) performed laser-assisted turning of silicon nitride with complex features and indicated that the cutting forces in LAM are strongly influenced by the material removal temperature. Chang and Kuo (2007) revealed that laser-assisted planing of Al_2O_3 ceramics can greatly reduce cutting force and improve surface quality compared with conventional planing.

For laser-assisted milling (LAMill) of ceramics, Shen et al. (2005) first used a finite element analysis (FEA) thermal model to analyze the temperature distribution of the workpiece and predict the potential surface/subsurface cracks through thermal stress analysis. However, the model only focused on laser heating without considering the material removal and was not validated. Later on, Yang and Lei (2008) did a series of experiments of laser-assisted milling. The authors found that both the cutting forces and specific cutting energy decrease with high cutting temperature. Also, Tian et al. (2008) conducted some experiments of laser-assisted end milling of silicon nitride. They pointed out that there was a narrow range of material removal temperature (about 1200-1300°C) with the TiAlN coated carbide tools. Recently, Shen and Lei (2009) developed a three-dimensional FEA heat transfer model including material removal. The validated model successfully predicts the temperature variations of the workpiece.

All the above research shows that temperature plays a significant role in LAM of ceramics. However, there is no literature available to find detailed guidelines on parameter selection based on the analysis of operating temperature which incorporates the thermal aspects from laser-ceramic interaction mechanism, effect of parameters on temperature, and evaluation of surface quality of the machined workpieces. Therefore, an efficient approach for the selection of operating conditions in LAMill is definitely needed for successful LAMill operation. To this end, this Chapter first explores the laser-silicon nitride interaction mechanism by a series of heating experiments. Since different applications of laser materials processing have different temperature requirements, understanding the laser-ceramic interaction mechanism can help us select more reasonable temperatures for LAM. So far some studies have been reported on laser-ceramic interaction mechanisms in some applications such as surface treatment, welding, shaping and machining (Heuvelman et al., 1992; Mikhailova et al., 2004; Tsai et al., 2004;

Samant et al., 2008a, 2008b, 2009a, 2009b, 2009c, 2009d); however, little literature highlights on LAM of ceramics. Tian and Shin (2006) investigated the effect of oxidation of silicon nitride on the microstructure of the workpiece surface under different temperatures in LAM, but they did not elaborate on how oxidation influences the workpiece temperature. In this study, another aspect from the effect of parameters on temperature is achieved through a parametric study of key parameters including laser power, laser beam diameter, feed rate and preheat time, and the purpose is to obtain the trends of temperature variations. The last aspect of surface quality evaluation of the machined workpieces arises from the fact that the quality of the machined workpiece strongly depends on the temperature.

In the following sections, laser-ceramic interaction mechanism is first investigated. Then, a parametric study is conducted through a series of heating experiments, and surface quality is evaluated in terms of edge chipping, surface roughness and surface residual stress, respectively. Finally, guidelines on parameter selection for LAMill are provided from these three aspects.

2.2 Experimental Setup of LAMill

The experimental setup for laser-assisted milling of silicon nitride is illustrated in Figure 2.1. The milling operation is carried out on a CNC machine (Haas Automation Inc.). A diode laser (Visotek Inc., DFL500) in continuous wave mode is used to generate a high power laser beam with a top hat power distribution. An infrared pyrometer (Williamson Inc., Model 91-20-C-23D) with a range of 475-1750 °C is applied to concurrently measure the surface temperature of the workpiece. Since the pyrometer measures at the wavelength of 1.5 μm and the laser's wavelength used in this study is 0.94 μm , the pyrometer measurement should not be affected by the laser radiation. The dynamometer (Kistler Inc., Type 9257B) is fixed on the worktable and utilized with a charge amplifier (Kistler Inc., Type 5010) to measure the cutting forces in the global x , y , and z directions. Both the pyrometer and the laser optics are installed through holders on the spindle. The workpiece is fed into the milling cutter at a feed rate (V_f) and clamped with a vice mounted on the dynamometer. Between the workpiece and vice, insulating materials are used to prevent heat loss. The workpieces used in this study are a sintered bonded silicon nitride ceramic (Si_3N_4) with 8wt% additives such as Y_2O_3 and Al_2O_3 (Ceradyne Inc.). The dimensions are 4.3×5.3×48 mm.

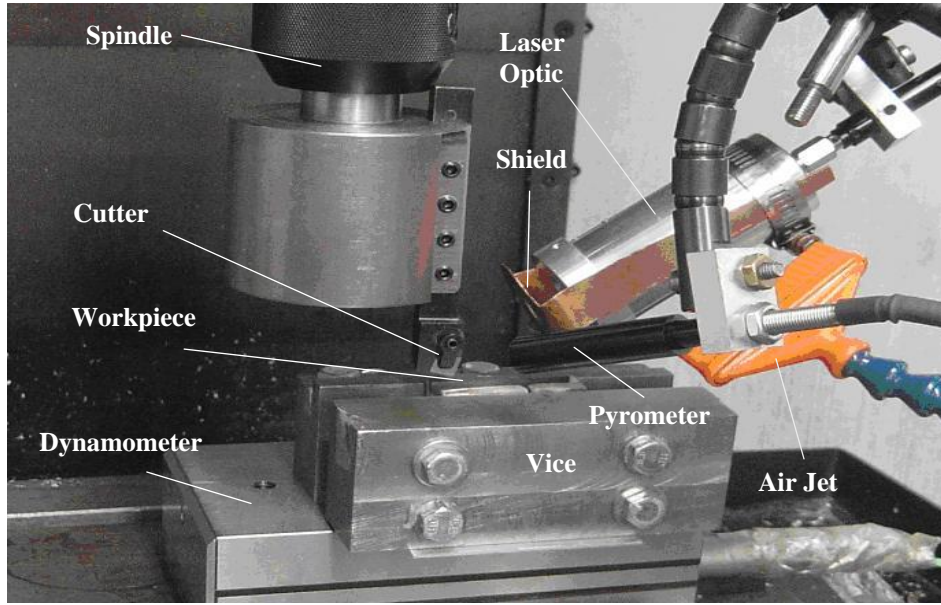


Figure 2.1 Experimental setup of laser-assisted milling (LAMill)

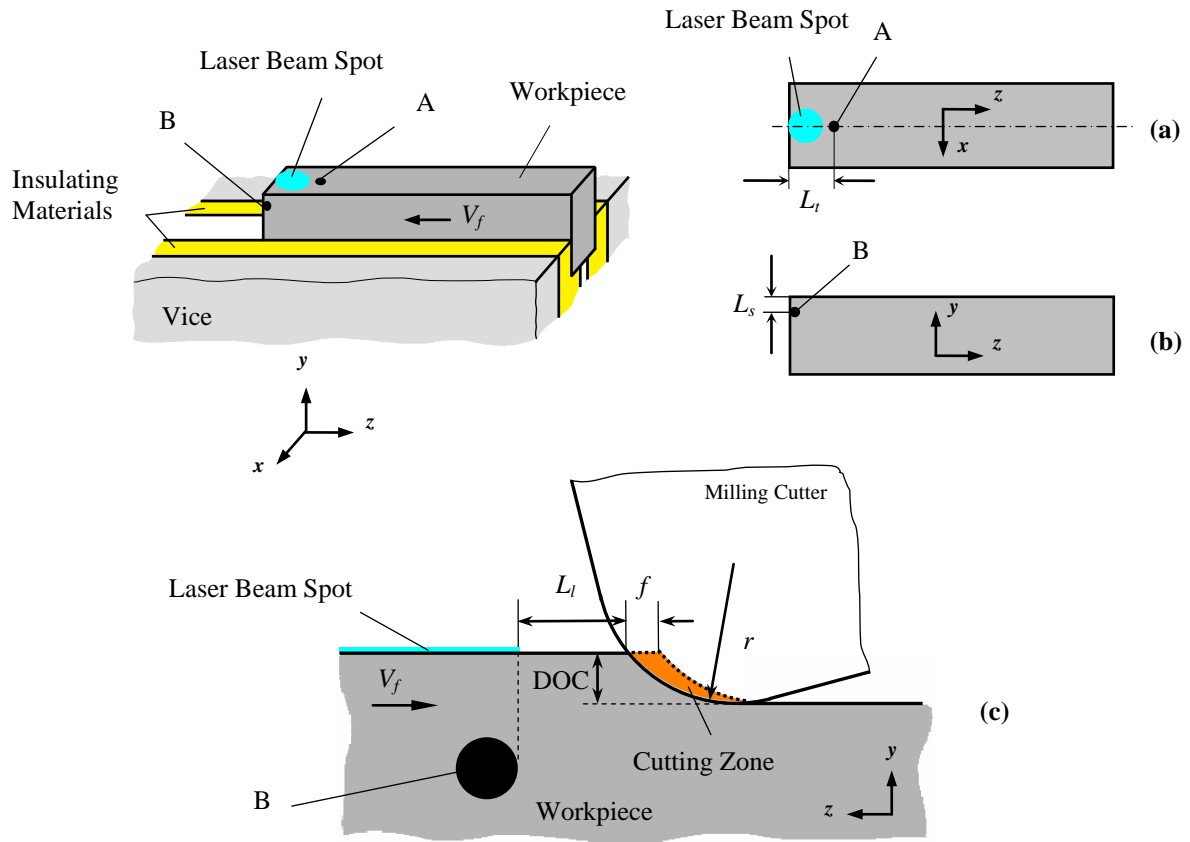


Figure 2.2 Schematic of LAMill setup (a) Top face (b) Side face (c) Cutter and cutting zone

Figure 2.2 schematically shows the relationship between the workpiece and the spots of the laser beam and the pyrometer. Between the laser spot and the cutter, a small distance, laser-cutter allowance (L_l), is maintained in case the laser spot overlaps and damages the cutter. In this study, two measurement points are selected for the pyrometer: Points A and B. The measurement point in LAM is commonly selected to be at the laser beam spot (Rozzi et al., 1998; Lei et al., 2001; Rebro et al., 2004; Pfefferkorn et al., 2004; Tian and Shin, 2006). However, the formation of silica bubbles induced by laser heating in LAMill of silicon nitride discussed later in Section 2.3.1 will affect the measurement at the laser beam spot. Hence, the position of Point A is away from the areas possibly covered with the bubbles. The other reason to select Point B as a measurement point is that the point-wise temperatures over the cutting zone in LAMill are expected to exceed the softening temperature, say 1000°C (Lange, 1972; Hampshire, 1991), because the hardness and the strength of silicon nitride ceramics have considerable reduction above that temperature. Thus, the minimum temperature of the cutting zone which occurs at the side faces of the workpiece is specially focused (Shen and Lei, 2009). In this study, Point A is used in heating experiments for investigating laser-Si₃N₄ interaction mechanism. Point B is used in heating experiments for the parametric study and machining experiments. In Figure 2.2, the positions of Points A and B on the workpiece are the initial positions. The length, L_t , from the center of Point A to the left end of the workpiece is 6 mm, and the length, L_s , from the center of Point B to the top surface is 1.5 mm.

2.3 Investigation on Laser-Si₃N₄ Interaction Mechanism

2.3.1 Heating Experiments

The heating experiments are conducted so as to explore the interaction mechanism between the laser and the silicon nitride. The beam diameter is measured with the knife edge technique (Khosrofian and Garetz, 1983). Based on our experience in laser-assisted machining experiments the operating conditions are selected as follows: feed rate (V_f) of 12 mm/min, laser beam diameter (D_l) of 2.1 mm, preheat time (t_p) of 0 s and laser power (P_l) with four levels of 175 W, 200 W, 225 W and 250 W.

Figure 2.3a displays an as-received workpiece surface and Figures 2.3b-f show five heated surfaces under different heating conditions. At the laser power of 175 W, the heated surface turns white (Figure 2.3b) but shows no trace of material removal. As the laser power

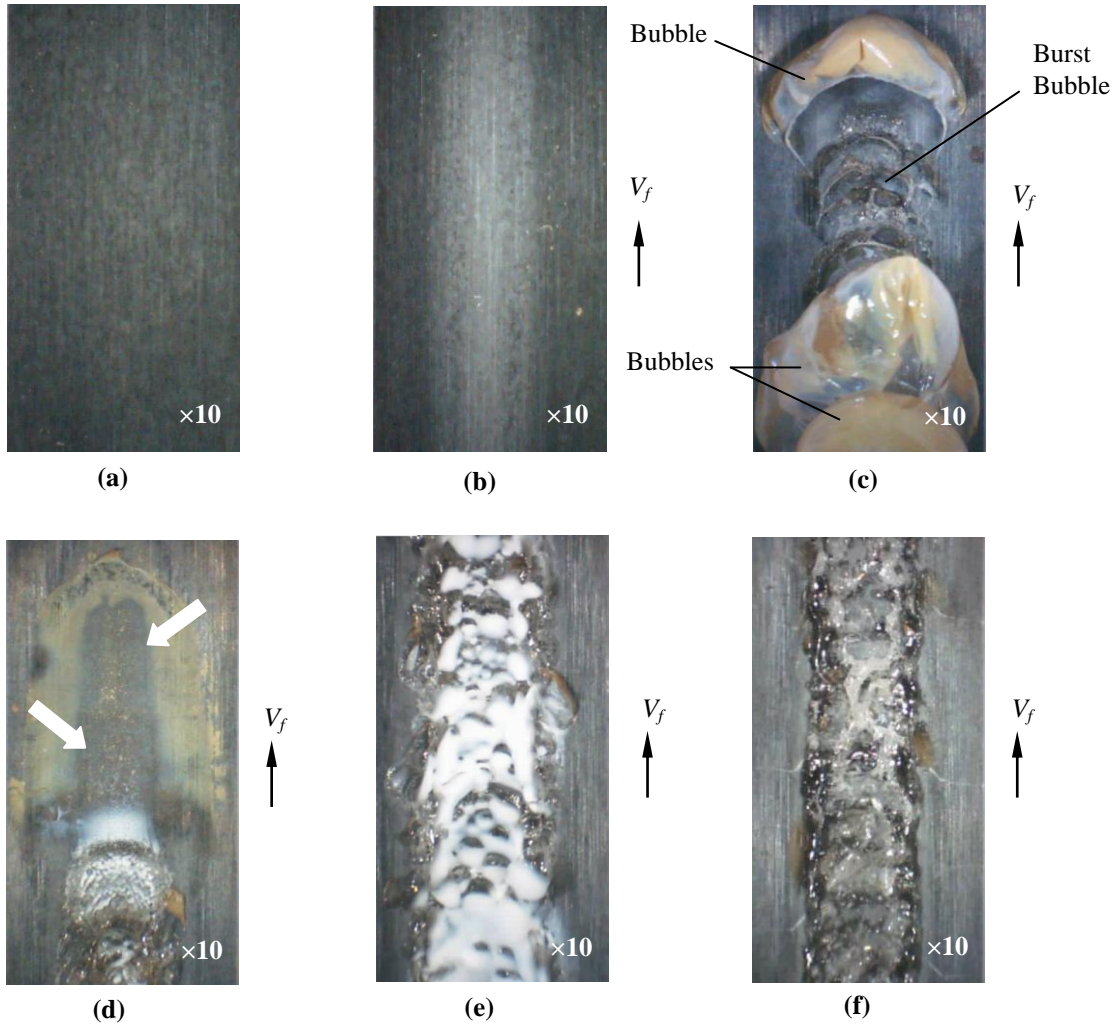


Figure 2.3 Workpiece surfaces (a) As-received (b) White color (175 W) (c) Bubbles (200 W) (d) Bubble-covered surface (225 W) (e) White silica powders (250 W) (f) Groove (250 W)

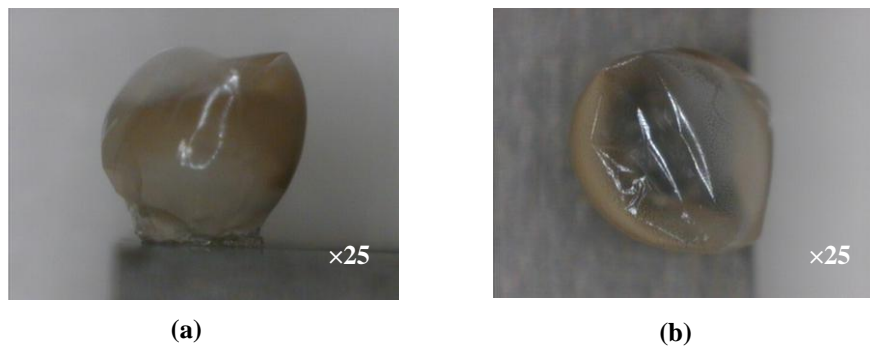


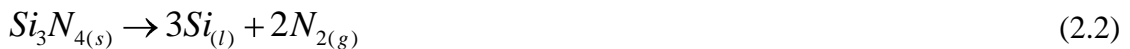
Figure 2.4 Silica bubble (a) Side face (b) Top face

reaches 200 W, a series of bubbles form and then burst along the feed rate direction (Figure 2.3c). A clear one is shown in Figure 2.4. The EDS (Energy-Dispersive X-Ray Spectroscopy) elemental analysis, shown in Figures 2.5 and 2.6, suggests that the white material in Figure 2.3b and the bubbles in Figure 2.4 are all silica. As the temperature increases, the top layer of the workpiece starts oxidizing, thus forming a thin silica film. This process can be simplified as the following Equation (2.1) (Lavrenko et al., 1985; Howlett et al., 1986; Bushby, 1994) due to the complexity of oxidation. Note that SiO_2 is thermodynamically more stable than the other species such as SiO (Taguchi and Ribeiro, 2004). As the temperature further rises, the softened silica film is gradually blown bigger and bigger by the released nitrogen gas. Consequently a silica bubble forms. With the temperature continuously going up, the pressure of nitrogen gas increases as well, thus destroying the bubble. The region once covered by a bubble is indicated by the arrows in Figure 2.3d.



Up to 250 W, a wisp of smoke-like material is observed and then turns into white powders after cooling. These powders and those located on the heated surface (Figure 2.3e) are both proved to be silica from the EDS analysis (Figure 2.7). After several repeated heating on the same surface, the silica powders located on the heated surface disappear and instead a very clear shallow groove forms (Figure 2.3f) due to the material removal with high laser intensity.

Actually, as the temperature exceeds approximately 1878°C (decomposition temperature of silicon nitride) (Singhal, 1976), silicon nitride starts decomposing into liquid silicon and nitrogen gas following Equation (2.2) (Maruo et al., 1992; Morita, 1993). The liquid silicon is then blown off by the high pressure nitrogen gas. Since silicon has a high affinity towards oxygen, the expelled liquid silicon is quickly oxidized by the oxygen in air following Equation (2.3), thus forming the smoke-like material mentioned above. With temperature further increasing, plasma may occur (Batha and Whitney, 1973; Howlett et al., 1986), but this situation may not happen in LAM, because the purpose of laser heating is to make the material softened rather than melted or vaporized.



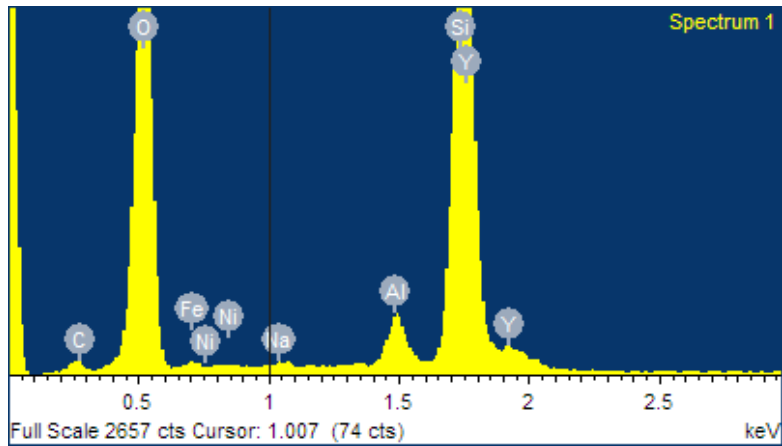


Figure 2.5 EDS spectrum of elements detected in the heated zone

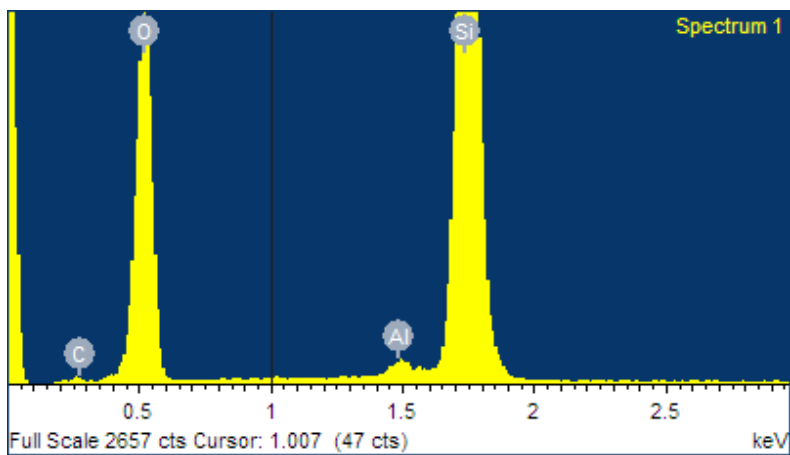


Figure 2.6 EDS spectrum of elements detected in the bubble

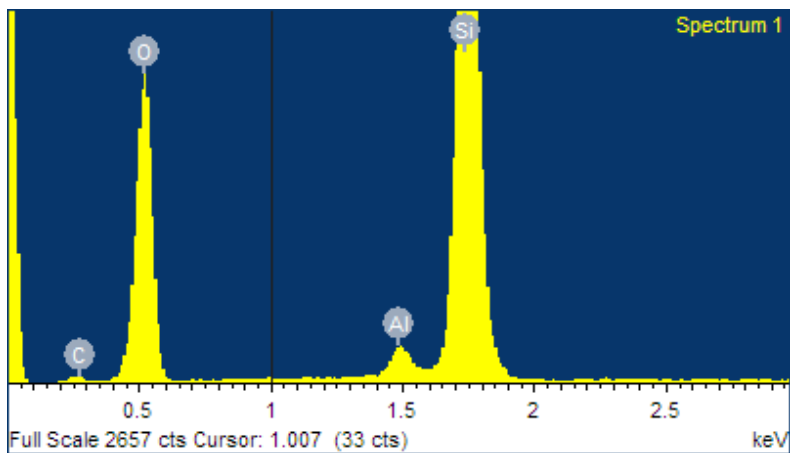


Figure 2.7 EDS spectrum of elements detected in the powders

2.3.2 Effect of Silica Bubble on Heating

Zhang and Modest (1983) found that below the decomposition temperature, the absorptivity of silicon nitride remains almost at a constant value of 0.85 at laser wavelength of 1.06 μm , which is close to 0.94 μm used in this study. Therefore, this study ignores the effect of the absorptivity on temperature and focuses on silica bubble.

In order to examine the effect of silica bubble on workpiece temperature, repeated laser heating experiments are conducted. Since considerable amount of silica bubbles are discovered in the heating experiments in Section 2.3.1 under the conditions of $P_l = 250 \text{ W}$, $V_f = 12 \text{ mm/min}$, $D_l = 2.5 \text{ mm}$, $t_p = 0 \text{ s}$, this set of operating conditions is used in the repeated heating experiments.

Figure 2.8 provides the temperature variations in the repeated laser heating experiments. When the as-received workpiece is first heated, some temperature fluctuations show in Curve 1. Experimental observation reveals that these fluctuations are associated with bubble formation rather than absorptivity. Once bubbles form, the temperature goes up. The reason is that the

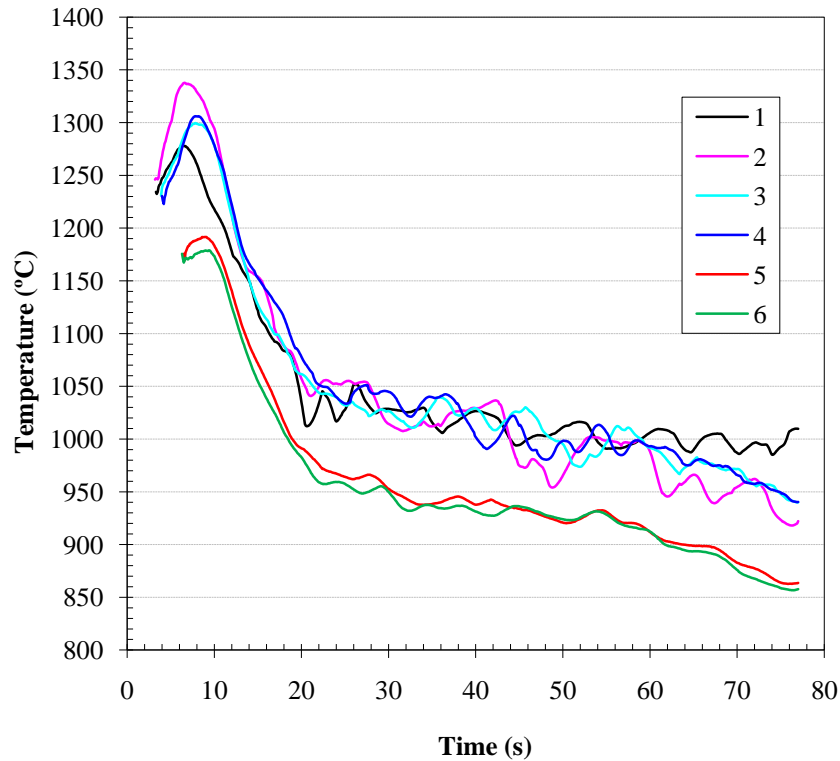


Figure 2.8 Effect of silica bubble on temperature
($P_l = 250 \text{ W}$, $V_f = 12 \text{ mm/min}$, $D_l = 2.5 \text{ mm}$, $t_p = 0 \text{ s}$)

bubble formation (Equation (2.1)) induced by the oxidation of silicon nitride is an exothermic process (McColm, 1983). The heat energy released (roughly 800 J/mol (Themelin et al., 1993)) can help raise the workpiece temperature. So far no literature has been found to report a quantitative relationship between the energy released and the temperature rise. Because the material around the laser-covered region in each heating pass is only partially oxidized due to the protection from bubbles (Figure 2.3d), some fluctuations are also found in the following repeated heating tests such as Curves 2, 3 and 4. However, the temperature tends to decrease as shown in Curves 2, 3 and 4. After four repeated heating tests no bubble forms. In this situation the temperature variation gradually goes smooth (Curves 5 and 6). It is found that the temperature differences between the first (Curve 1) and the last (Curve 6) heating are around 100°C, which suggests that, to some extent, bubble formation is beneficial to LAMill.

Bubble formation in laser heating indicates that material removal happens, which depends on a threshold value of laser intensity (Töenshoff and Gedrat, 1991). Below this threshold, the absorbed heat energy through the workpiece top surface is mainly transferred into the material through conduction, with some loss due to convection and radiation. In this study, the threshold intensity was roughly calculated to be around $4 \times 10^3 \text{ W/cm}^2$ by the laser power and the beam diameter through a series of heating experiments.

2.4 Parametric Study on Heating Experiments

In this section, a parametric study is conducted to analyze how the parameters in LAMill affect the temperature. The purpose is to obtain the trends of temperature variations in LAMill and serve the parameter selection in the next step. It should be mentioned that in this section the measurement point is selected to be Point B. That is, all the temperatures in this parametric study are the temperatures at Point B.

2.4.1 Parameters in LAMill

For the laser with continuous wave mode, the parameters in LAMill can be classified into two groups: (1) parameters associated with laser and (2) parameters associated with machining. The former mainly includes laser power (P_l), laser beam diameter (D_l), preheat time (t_p), and laser moving speed. The latter mainly consists of depth of cut (DOC), feed rate (feed, V_f), cutting speed (V_c) and laser-cutter allowance (L_l). According to the relative motion of the workpiece and the laser, the value of the feed rate is the same as the laser moving speed; therefore, for

Table 2.1 Operating conditions in the parametric study

Laser power (W)	Laser Beam Diameter (mm)	Feed rate (mm/min)	Preheat time (s)
<i>300</i> <i>340</i> <i>410</i>	3.3	6	13
340	<i>1.8</i> <i>2.6</i> <i>3.3</i>	6	13
340	3.3	<i>3</i> <i>6</i> <i>12</i>	13
340	3.3	6	<i>4</i> <i>8</i> <i>13</i>

convenience, the following sections will use the term “feed rate” instead of “laser moving speed”. Since the quality of the machined workpiece is dominantly determined by operating temperature, the key parameters associated with laser (Table 2.1) are considered in this parametric study.

2.4.2 Preheat Time

The purpose of preheating is to elevate the temperature at the cutting zone, thus softening the material before milling. In considering the distance (L_l) between the laser spot and the cutter, the selection of the preheat time should ensure that the minimum temperature in the cutting zone is still higher than the softening temperature once the cutter starts to contact the workpiece.

Figure 2.9 shows the temperature variations with t_p of 4 s, 8 s and 13 s and with the other parameters fixed ($V_f = 6$ mm/min, $D_l = 3.3$ mm, and $P_l = 340$ W). In the preheating stage, the workpiece is stationary and thus the temperature rises quickly. The peak temperature occurs right

after preheat time and then gradually drops as the workpiece begins to move. With the workpiece moving forward, the laser beam gradually moves away from the left end of the workpiece (Figure 2.2) and towards the middle of the workpiece. In this situation, the temperature continues to slightly drop in that more heat energy is conducted from the beam spot to the two ends of the workpiece. From Figure 2.9, it can be seen that a longer preheat time can cause higher temperatures in the preheating stage. With the workpiece moving, the influence of preheat time on the temperature becomes weaker and weaker, and then the three curves gradually converge.

2.4.3 Laser Power

Figure 2.10 shows the temperature variations with P_l of 300 W, 340 W and 410 W while the other parameters are fixed ($t_p = 13$ s, $V_f = 6$ mm/min, and $D_l = 3.3$ mm). For the three cases, it can be seen that the higher the laser power, the more heat energy the workpiece absorbs, and then the higher temperature the workpiece has.

2.4.4 Laser Beam Diameter

Figure 2.11 illustrates the temperature variations with D_l of 3.3 mm, 2.6 mm and 1.8 mm and with the other parameters fixed ($t_p = 13$ s, $V_f = 6$ mm/min, and $P_l = 340$ W). The average laser intensity for the three diameter is approximately 4×10^3 , 7×10^3 , and 1.7×10^4 W/cm², respectively. Although the laser power is the same, the smaller beam diameter gives higher temperature. One reason is that there is a smaller region covered with laser beam. The other reason is that the laser with a smaller beam diameter has higher laser intensity, thus causing more energy released from oxidation reaction.

2.4.5 Feed Rate

Figure 2.12 shows the temperature variations with V_f of 3 mm/min, 6 mm/min and 12 mm/min while the other parameters are fixed ($t_p = 13$ s, $D_l = 3.3$ mm, and $P_l = 340$ W). The moving length is 13.7 mm. As the feed rate decreases, more heat energy is deposited in the workpiece thus obtaining higher temperatures. In other words, within the same moving length, the time that the laser beam stays on the workpiece is getting longer. That is, with a low feed rate, a high temperature can be obtained in machining process, thus enhancing the machinability of silicon nitride and decreasing the cutting force. Hence, as the laser power is fixed, to adjust the feed rate can obtain a high operating temperature.

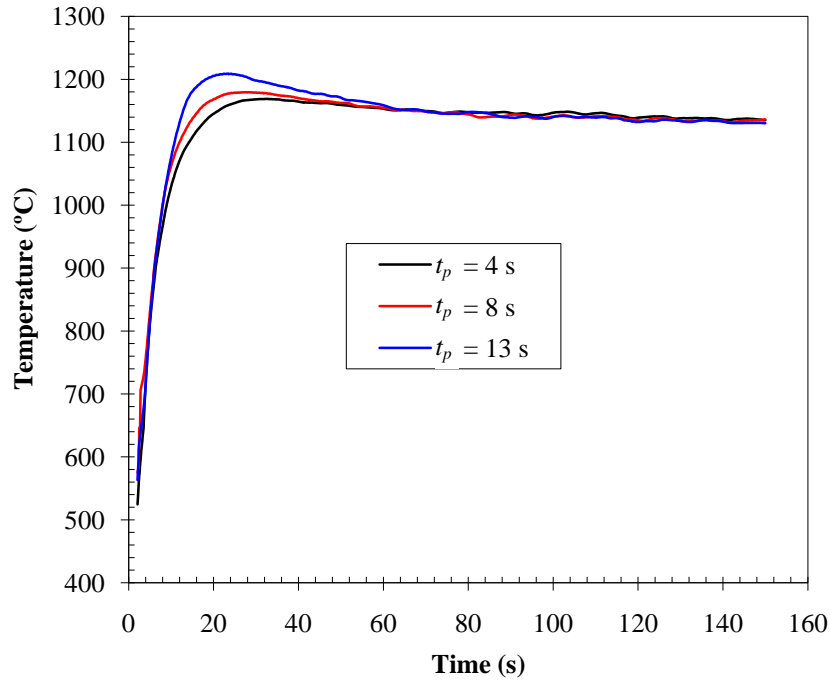


Figure 2.9 Effect of preheat time on temperature
 ($P_l = 340$ W, $D_l = 3.3$ mm, $V_f = 6$ mm/min)

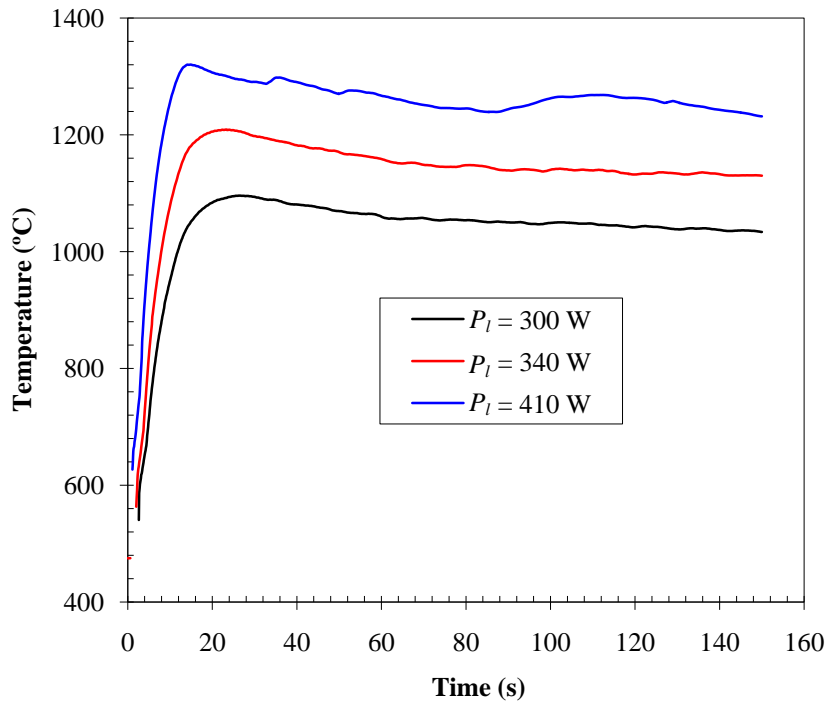


Figure 2.10 Effect of laser power on temperature
 ($V_f = 6$ mm/min, $D_l = 3.3$ mm, $t_p = 13$ s)

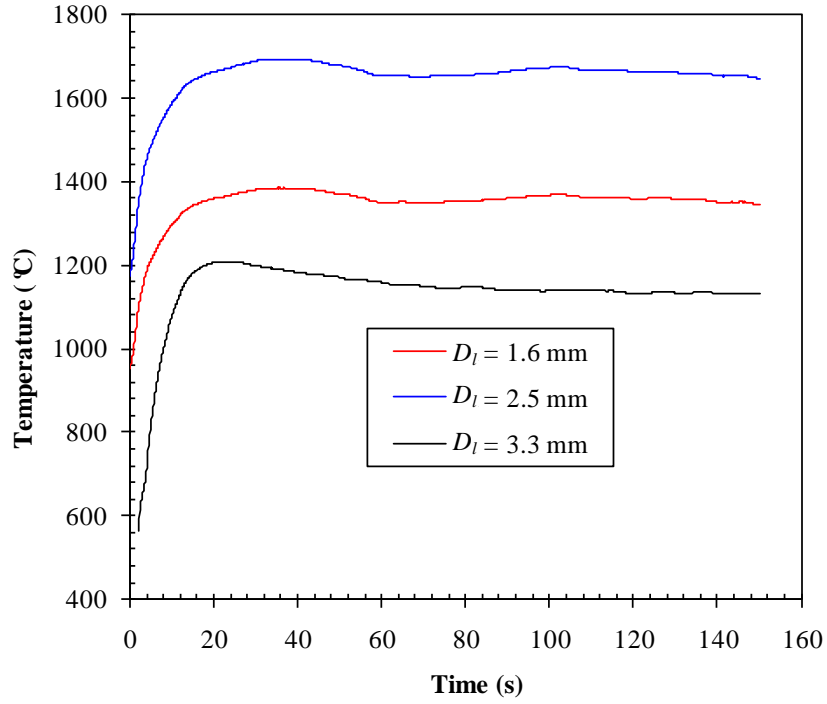


Figure 2.11 Effect of laser beam diameter on temperature
 ($P_l = 340$ W, $V_f = 6$ mm/min, $t_p = 13$ s)

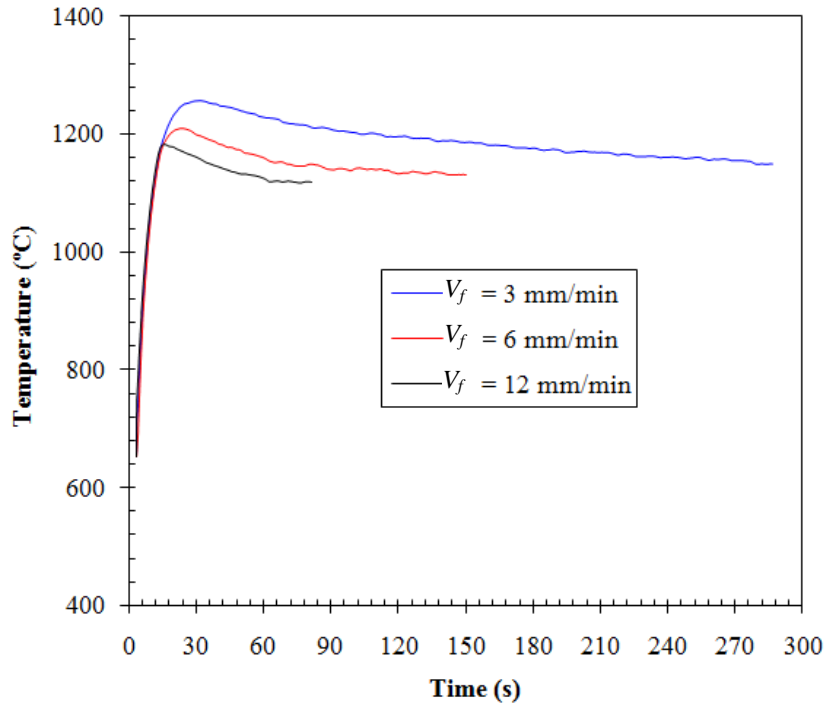


Figure 2.12 Effect of feed rate on temperature
 ($P_l = 340$ W, $D_l = 3.3$ mm, $t_p = 13$ s)

2.4.6 Laser Intensity

The above parametric study shows that both the increase of laser power and the decrease of laser beam diameter essentially enhance the laser intensity. Under a certain fixed laser intensity, both the decrease of feed rate and the increase of preheat time relatively prolong heating time on the workpiece.

Section 2.3.2 indicates that small material removal is desired in LAMill which is preceded by bubble formation; and too much material removal usually needs high laser intensity, which may damage the machined surface of the workpiece. As shown in Figure 2.3f, a groove is generated due to high laser intensity. If the groove could not be removed by milling, the machined surface would be the situation indicated by the arrows in Figure 2.13. Of course, the appearance of damages in milling depends on the value of depth of cut. Depth of cut is a machining parameter which is set before each cut. A large depth of cut can eliminate the damage layer, but cause high cutting force as well. Hence, the selection of depth of cut, to some extent, strongly affects the machining process. However, for a given depth of cut in LAMill, the selection of laser intensity should not only ensure the bubble formation but also prevent the damages induced by heating.

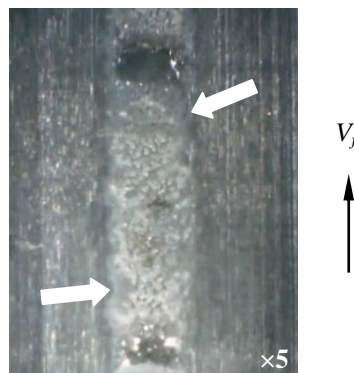


Figure 2.13 Damage in a machined surface

2.5 Evaluation of Surface Quality under Different Operating Temperatures

In order to study how the temperature affects the quality of the machined workpiece, a series of LAMill are conducted. The measurement point is selected to be Point B. As is known, silicon nitride is a temperature-dependent material whose properties (e.g. hardness and strength)

considerably degrade over the softening temperature, say 1000°C (Lange, 1972; Hampshire, 1991). It means that a better performance of LAMill can be achieved if the point-wise temperatures over the cutting zone are above that value. Hence, the minimum temperature over the cutting zone is of great concern in this study. The point that has the minimum temperature is defined as the minimum temperature point (MTP).

2.5.1 Operating Temperature and Cutting Force

Although the actual temperatures over the cutting zone are not the temperatures measured at Point B, they were successfully predicted through a three-dimensional transient FEA thermal model (Shen and Lei, 2009) developed with the finite element code ANSYS 11.0. In this model, the considered boundary conditions include convection, radiation, laser heat flux, and heat generation induced by machining. The model was validated with a series of experiments in terms of the parameters of laser power, feed and cutting speed. It was found that the maximum temperature over the workpiece occurs at the laser spot. The temperature gradually decreases from laser spot to its surrounding portion, thus causing temperature gradients (Note that too large temperature gradients may cause surface/subsurface cracks in the workpiece). Moreover, the temperature at Point B shares the same trend with the cutting zone, which suggests that Figures 2.9-2.12 can reflect the trends of operating temperatures over the cutting zone.

Figure 2.14 illustrates the temperature histories at the MTP predicted in our previous work (Shen and Lei, 2009) under three sets of operating conditions: (a) $P_l = 300$ W, $t_p = 15$ s; (b) $P_l = 410$ W, $t_p = 12$ s; and (c) $P_l = 470$ W, $t_p = 8$ s, and the fixed parameters include D_l of 3.6 mm, V_f of 6.0 mm/min, V_c of 1.0 m/s and DOC of 0.2 mm. The maximum temperature difference over the cutting zone is about 100°C. Case (c) has the highest temperatures and Case (b) the next. Although the temperature slightly decreases in each case because of more material participating in heat conduction as the workpiece moves forward, the temperature differences among the three cases do not have too much change, since once the thermal system is in quasi-steady state, the differences tend to maintain a constant value (Shen and Lei, 2009).

In order to clearly show the relationship between operating temperature and cutting force, the averaged temperature and main cutting force are calculated within the initial cutting length of 2 mm, respectively. The reason to use the short cutting length is to reduce the effects from tool wear and edge chipping on cutting force. Figure 2.15 shows that the temperature difference

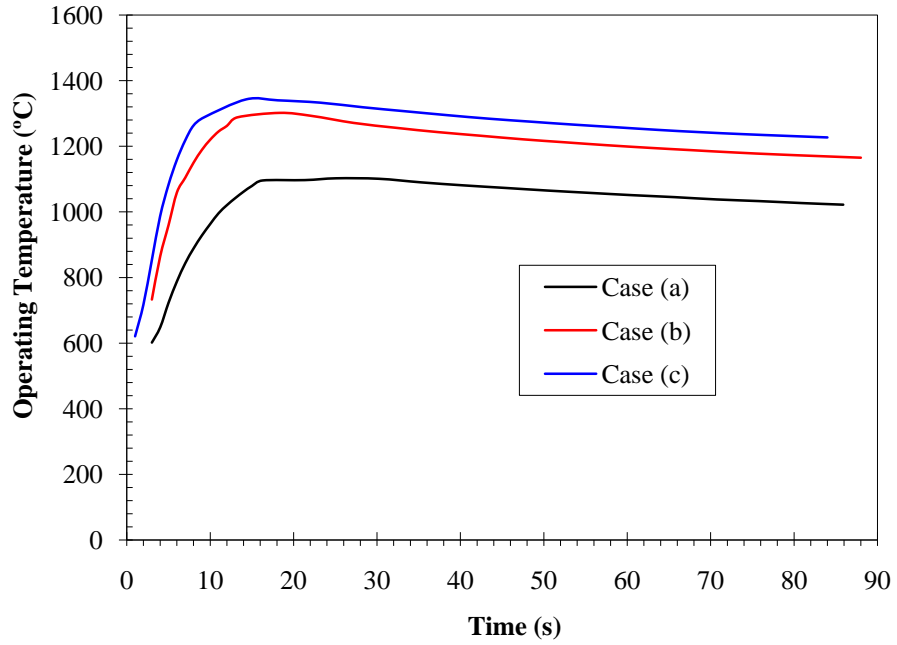


Figure 2.14 Predicted temperature histories

($D_l = 3.6$ mm, $V_f = 6.0$ mm/min, $V_c = 1.0$ m/s, $DOC = 0.2$ mm, and Case (a): $P_l = 300$ W, $t_p = 15$ s, Case (b): $P_l = 410$ W, $t_p = 12$ s, Case (c): $P_l = 470$ W, $t_p = 8$ s)

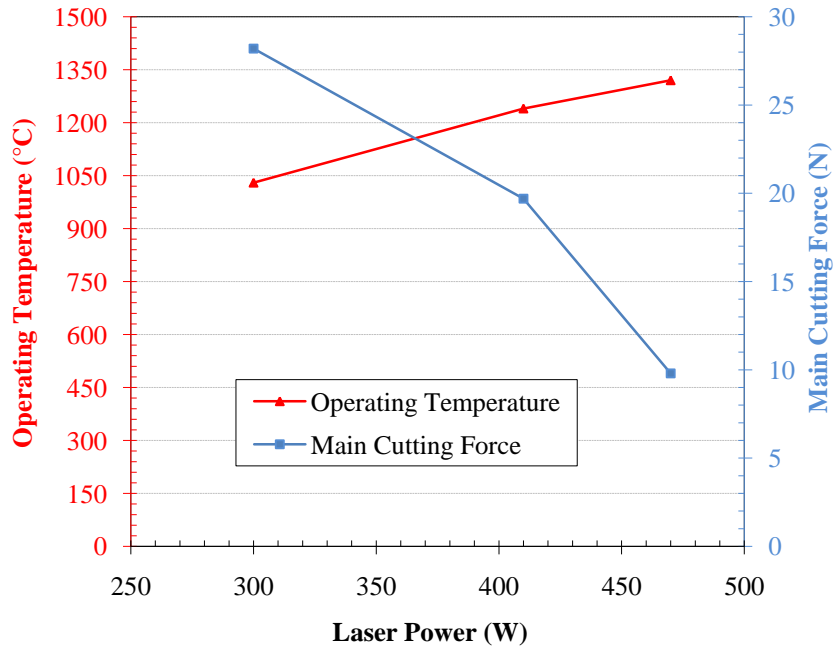


Figure 2.15 Relationship between temperature and main cutting force

($D_l = 3.6$ mm, $V_f = 6.0$ mm/min, $V_c = 1.0$ m/s, $DOC = 0.2$ mm, and Case (a): $P_l = 300$ W, $t_p = 15$ s, Case (b): $P_l = 410$ W, $t_p = 12$ s, Case (c): $P_l = 470$ W, $t_p = 8$ s)

between Cases (b) and (c) is not as large as expected with respect to the power differences between the three cases. The reason is that both Cases (b) and (c) have bubble formation and Case (a) does not. Moreover, although the temperature difference between Cases (b) and (c) is much smaller than that between Cases (b) and (a), the cutting force difference is larger than that between Cases (b) and (a). As discussed in next paragraph, this can be explained by the fact that, for silicon nitride, the brittle-to-ductile transition occurs at Case (b), which causes the large increase of fracture toughness and thus the cutting force does not decrease as rapidly as expected.

Mutoh et al. (1993) revealed that the brittle-to-ductile transition takes place between the temperature range of 1200-1275°C. Figure 2.16 shows that when the temperature is above 800°C but below the transition point, the fracture toughness decreases with increasing temperature due to the degradation of the strength of the intergranular glass phase. In this stage, intergranular fracture is dominant in silicon nitride. Once the temperature is up to the softening point of the glass phase (about 1200°C), the intergranular glass phase becomes adequately soft and the brittle-to-ductile transition of fracture occurs. At this temperature range, the fracture toughness rapidly increases from 4 MPam^{1/2} to exceed the value at room temperature due to the increase of resistance to brittle fracture, which causes the slow decrease of cutting force in machining. Once

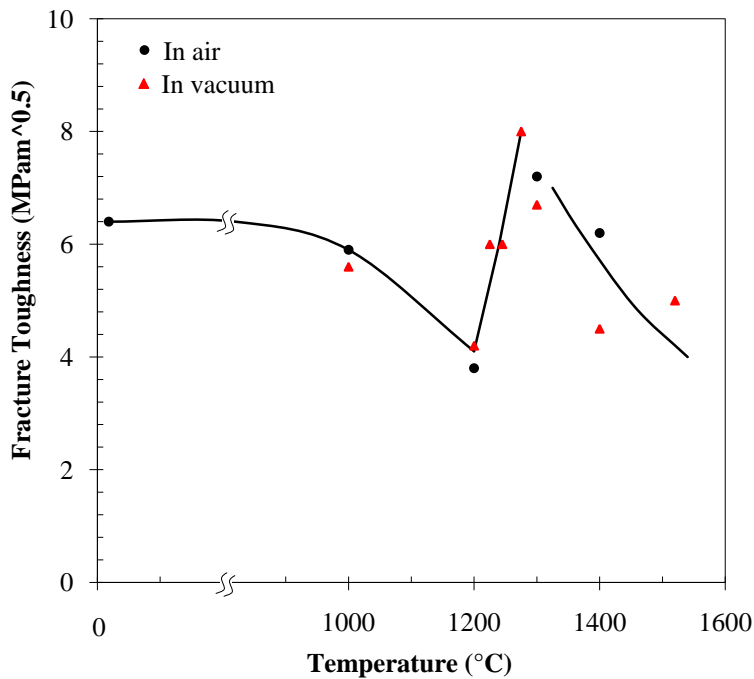


Figure 2.16 Relationship between fracture toughness and temperature (Mutoh et al., 1993)

the temperature is above the transition temperature, the decrease of viscosity is promoted and consequently the resistance to shear deformation of the intergranular glass phase decreases with increasing temperature. The variation of fracture toughness with temperature suggests that the brittle-to-ductile transition should be avoided as much as possible in LAMill.

2.5.2 Evaluation of Surface Quality

In the following, the surface quality is evaluated in terms of edge chipping, surface roughness and surface residual stress, respectively. The machined surfaces in Cases (a), (b) and (c) are shown in Figure 2.13.

Edge Chipping

Exit edge chipping is found in all these three cases, which is indicated by the arrows in Figure 2.17. Edge chipping is a sudden macroscale or microscale edge damage and arises from the sudden release of the energy built in the machining process. Three kinds of edge chipping for brittle materials are described: entry edge chipping, interior edge chipping and exit edge chipping. Exit edge chipping occurs when the cutter is leaving the workpiece. More detailed description on edge chipping can be found in (Yang et al., 2009). Figure 2.18 shows the variations of chipping width with the cutting length. It is clearly observed that with high operating temperature, the chipping width decreases and the curve goes smoothly. This is because the hardness and the strength of silicon nitride have a large decrease with high temperature.

Surface Roughness

Figure 2.19 provides the machined surfaces under these three cases. The surface roughness R_a was evaluated with a Sufitest-402 surface profilometer (Mitutoyo Corporation). The profilometer was calibrated using a standard reference specimen, then set to travel at a speed of 0.1 mm/s with a range of 4 mm during testing. To measure the R_a value, the diamond stylus (5- μm tip radius) was moved across each machined surface 20 times in longitudinal and transverse directions, respectively. The surface analyzer was used to determine the roughness profile of each measure. Finally, the average value was calculated and considered to be the R_a value. For Cases (a)-(c), the average values are 0.72 μm , 0.62 μm and 0.42 μm , respectively. It can be seen that with high operating temperature, good surface finish can be obtained.

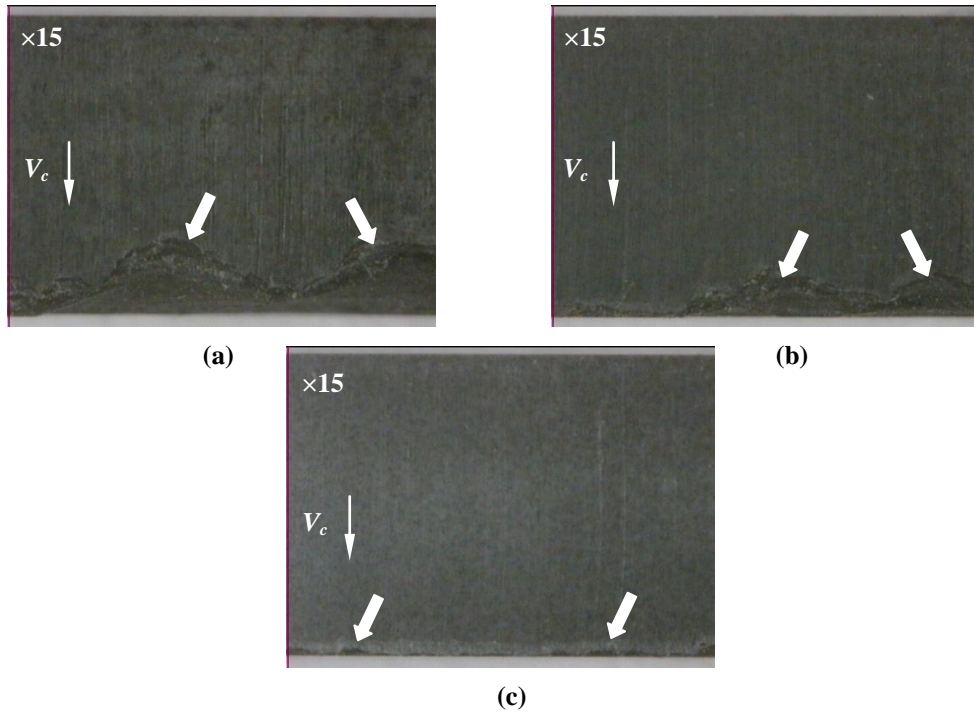


Figure 2.17 Machined surfaces under different operating temperatures (top view) ($D_t = 3.6$ mm, $V_f = 6.0$ mm/min, $V_c = 1.0$ m/s, $DOC = 0.2$ mm, and Case (a): $P_l = 300$ W, $t_p = 15$ s, Case (b): $P_l = 410$ W, $t_p = 12$ s, Case (c): $P_l = 470$ W, $t_p = 8$ s)

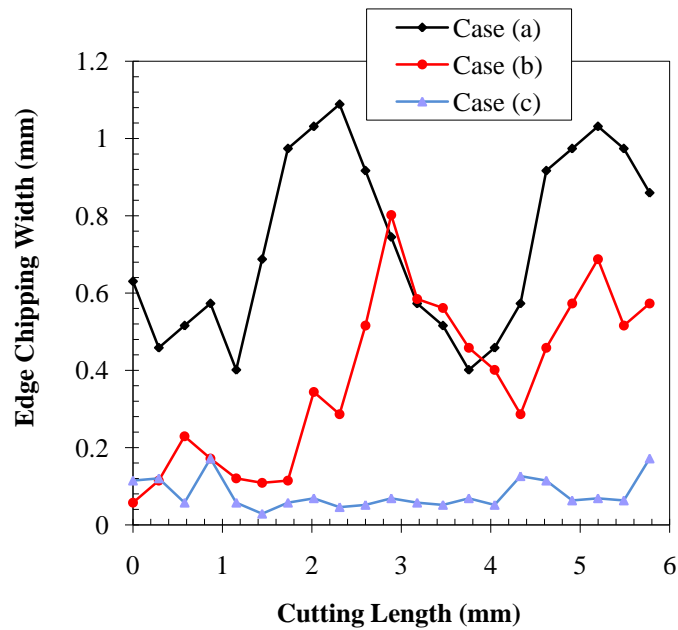


Figure 2.18 Variations of edge chipping width with the cutting length ($D_t = 3.6$ mm, $V_f = 6.0$ mm/min, $V_c = 1.0$ m/s, $DOC = 0.2$ mm, and Case (a): $P_l = 300$ W, $t_p = 15$ s, Case (b): $P_l = 410$ W, $t_p = 12$ s, Case (c): $P_l = 470$ W, $t_p = 8$ s)

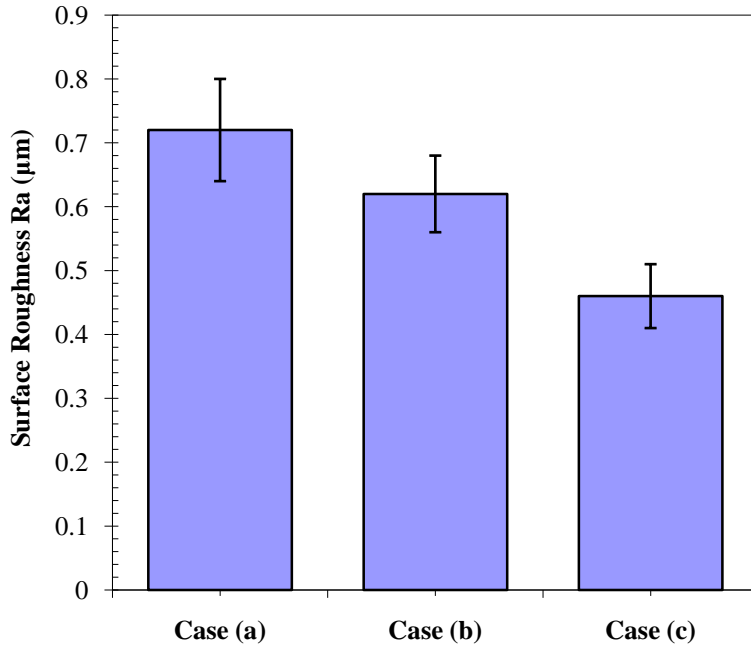


Figure 2.19 Surface roughness and operating temperature

Case (a): $P_l = 300$ W, $t_p = 15$ s; Case (b): $P_l = 410$ W, $t_p = 12$ s; Case (c): $P_l = 470$ W, $t_p = 8$ s

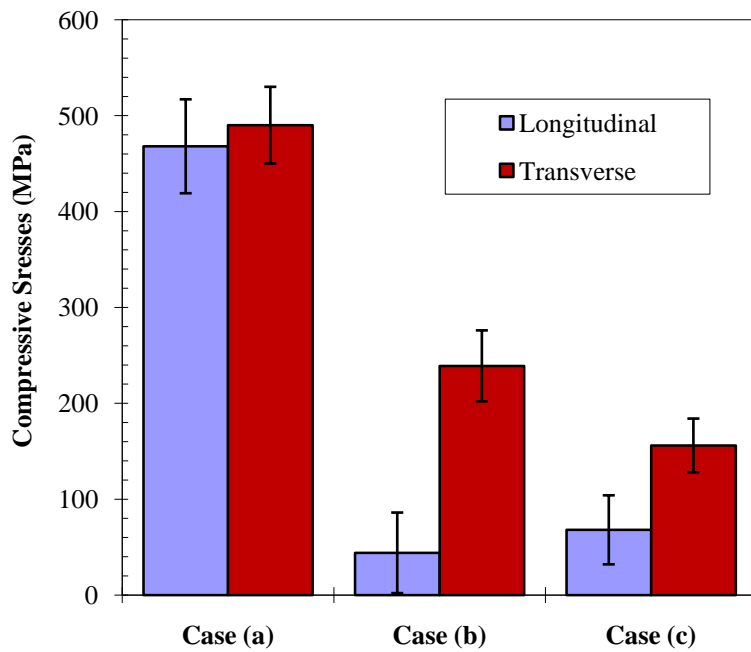


Figure 2.20 Surface residual stress under different operating temperatures

($D_l = 3.6$ mm, $V_f = 6.0$ mm/min, $V_c = 1.0$ m/s, $DOC = 0.2$ mm, and Case (a): $P_l = 300$ W, $t_p = 15$ s, Case (b): $P_l = 410$ W, $t_p = 12$ s, Case (c): $P_l = 470$ W, $t_p = 8$ s)

The machined surface produced by LAM mainly consists of amorphous glassy phase materials, cavities resulting from grain pullout, and dislodged β -Si₃N₄ grains (Lei et al., 2001). With a higher temperature, the intergranular glass phase is easier to redistribute via viscous flow process, and β -Si₃N₄ grains are liable to slide and thus dislocate in the silicon nitride crystallites. The cavities resulting from grain pullout will decrease. Moreover, the cavities are more likely to be filled with the intergranular glass phase. Thus, the machined surface looks smoother.

Residual Stress

Residual stresses were measured in collaboration with Lambda Technologies Inc. (Yang et al., 2009). X-ray diffraction residual stress measurements were performed using a multi-angle sine-squared-psi technique employing the diffraction of chromium K-alpha radiation from the (41.1) planes of the HCP crystal structure of Si₃N₄. The value of the x-ray elastic constant, $E/(1+\nu)$, required to calculate the macroscopic residual stress from the strain measured normal to the (41.1) planes of β -Si₃N₄ was determined empirically by employing a simple rectangular beam manufactured from β -Si₃N₄ loaded in four-point bending on the diffractometer to known stress levels and measuring the resulting change in the spacing of the (41.1) planes in accordance with ASTM E1426 (ASTM, 2003).

For the workpieces machined under Cases (a)-(c), the surface residual stresses were measured in the longitudinal and the transverse directions, respectively. As is known, the surface residual stresses of the machined workpiece by LAM are determined by the compressive residual stresses induced by the mechanical loading and the tensile residual stresses induced by thermal loading. Under high temperatures (above the softening point of the glassy phase), the mechanical loading produces larger microplastic deformation in the transverse direction than in the longitudinal (feed) direction. Therefore, as shown in Figure 2.20, there are higher compressive residual stresses in the transverse direction than in the longitudinal (feed) direction. In contrast, the thermal loading in the cutting zone leads to tensile residual stresses without a preferential orientation. The higher the temperatures at the cutting zone, the larger the tensile residual stresses. This is why high temperature has lower compressive residual stresses in Figure 2.20.

In summary, high operating temperature can reduce the cutting force and thereby decrease edge chipping, improve surface roughness and lower surface residual stress. However, high operating temperature can also reduce the material strength, hardness and so on. Hence,

when meeting the requirements of a specific application, the higher operating temperature the better; otherwise a compromise must be made between operating temperature and material strength; however, so far no technical data have been found on the relationship between the strength and temperature.

2.6 Guidelines on Parameter Selection

The evaluation of the machined workpieces shows that, in some extent, the higher the operating temperature below the decomposition temperature of the silicon nitride, the better the surface quality. Moreover, the temperatures over the cutting zone are recommended to be higher than the temperature range of brittle-to-ductile transition, thus avoiding the slow decrease of cutting force. According to the parametric study on heating experiments, a high operating temperature can be obtained by increasing the laser intensity. However, the laser-silicon nitride interaction mechanism indicates that laser intensity has a range for the successful operation of LAMill. That is, for a given depth of cut, the lower limit of the laser intensity is the threshold for silica bubble formation and upper limit is the value that causes the damage of the machined workpiece induced by heating.

The ways to increase the laser intensity include: (1) to increase laser power for a given beam diameter, (2) to decrease laser beam diameter for a given laser power, and (3) both of them. However, our previous work (Shen and Lei, 2009) shows that if the laser beam diameter is too small, it can result in large temperature gradients over the cutting zone. Correspondingly, the laser beam diameter is recommended to be as large as possible and then laser power is selected to be large enough so as to meet the requirement of laser intensity mentioned above. Once the laser power and beam diameter are decided, the expected operating temperature in LAMill can be obtained by adjusting feed rate. The operating temperature in the preheating stage can be achieved by regulating preheat time. Since the maximum operating temperature occurs right after preheat time (Figures 2.9-2.12), the surface damage induced by heating can only be focused on this stage. A numerical thermal model can be used to predict the temperature at the depth of cut. Once the temperature reaches the decomposition temperature of silicon nitride, the damage appears.

2.7 Conclusions

Some conclusions are summarized as follows:

(1) Laser-Si₃N₄ interaction mechanism indicates that laser heating gives rise to the silica formation at high temperatures in air. Silica bubble formation is desired in LAMill because the heat energy released from the oxidation reaction can increase the workpiece temperature.

(2) The parametric study on heating experiments reveals that high laser power, small laser beam diameter, small feed rate and large preheat time can cause high operating temperatures.

(3) The quality of the machined surface is strongly related to the operating temperature. High operating temperatures can cause small edge chipping, good surface finish, and low residual stress.

(4) The operating temperature in LAMill is recommended to be above the temperature range of brittle-to-ductile transition at which the fracture toughness has a rapid increase. The laser intensity should be in the range higher than the threshold for silica bubble formation and lower than the value that causes the surface damage induced by heating.

(5) There is still some work to be done in the next step, for example, the studies on the effect of laser intensity on the damage depth, the relationship between temperature and the strength of the machined workpieces, etc.

Chapter 2 - Thermal Modeling and Experimental Investigation for Laser-Assisted Milling of Silicon Nitride Ceramics *

As indicated in Chapter 2, temperature control is very important for the success of laser-assisted milling. Thus, in this Chapter, a transient three-dimensional (3D) thermal model is developed using finite element analysis (FEA) so as to explore the thermal characteristics in laser-assisted milling (LAMill) of silicon nitride ceramics. Furthermore, the effects of laser power, feed and cutting speed on temperature are investigated and the model is validated through a series of experiments of LAMill. Note that heat generation associated with machining is considered in this model.

3.1 Introduction

Laser-assisted machining (LAM) can potentially decrease machining cost, improve efficiency and reduce surface/subsurface flaws of ceramics. König and Zaboklicki (1993, 1994) demonstrated the feasibility of LAM for advanced ceramics and pointed out that LAM is one kind of hot machining. Shin et al., (2000) also indicated that LAM is one kind of thermally assisted machining techniques and temperature is critical to the successful operation of LAM. Apparently, temperature analysis is necessary and very important in LAM. Currently, the effective approach to achieve it is through numerical modeling.

The modeling methods involve analytical treatment, finite difference method (FDM), finite volume method (FVM), and finite element analysis (FEA). Westkämper (1995) developed a two-dimensional finite element analysis (FEA) model for laser-assisted grinding of silicon nitride, but detailed description of the model was not given. Janvrin (1996) built a three-dimensional heat conduction model for laser-assisted turning of silicon nitride using finite difference method (FDM). In this model, a constant temperature at the laser-beam covered region was assumed. Thermal radiation and convection were neglected and the material removal

The contents of this Chapter are from my following journal paper:

* **Shen, Xinwei** and Lei, Shuting (2009). Thermal modeling and experimental investigation for laser-assisted milling of silicon nitride ceramics. *Journal of Manufacturing Science and Engineering, Transactions of the ASME*, 131(5), 051007-1-10

was not considered. Gutierrez and Araya (2004) established an analytical conduction model for laser-assisted machining of silicon nitride. They also neglected thermal radiation, convection and the material removal. In order to find the temperature distribution for laser-assisted planing of Al_2O_3 ceramics, Chang and Kuo (2006) developed a two-dimensional transient heat conduction model and applied Lattice Boltzmann method (LBM) to calculate the temperatures inside the ceramic workpiece. They did not consider thermal radiation and convection. A quasi-steady-state analytical thermal model was established by Ching et al. (2007) for laser-assisted turning of zirconia ceramics. Similarly, they did not consider the material removal and boundary conditions of thermal radiation and convection. It should be noted that, in addition to thermal radiation and convection, all the above-mentioned models neglected the temperature-dependent thermophysical properties of the materials, especially thermal conductivity and specific heat.

However, the following thermal models made much improvement in dealing with these issues. Both the temperature-dependent thermophysical properties and the boundary conditions of thermal convection and radiation were considered. Rozzi et al. (1998) used finite volume method (FVM) to develop a transient three-dimensional thermal model for laser-assisted turning of silicon nitride. They pointed out that laser translational speed, laser power, cutting speed and laser beam will affect the workpiece surface temperatures. Rebro et al. (2004) extended the model (Rozzi et al., 1998) to mullite ceramics. Through evaluating the axial and radial thermal gradients, they presented a two-step power method for applying laser power thus avoiding thermal fracture and crack formation. Also, Pfefferkorn et al. (2005) extended the model (Rozzi et al., 1998a) to partially-stabilized zirconia (PSZ) ceramics. Internal radiation, diffusion and convection are specially considered because of semi-transparent zirconia (PSZ) ceramics. They found that laser power, feed and depth of cut have considerable impact on the temperature distribution. Tian and Shin (2006) improved the model (Rozzi et al., 1998) to the complex feature. They concluded that laser power has the most significant influence on the workpiece temperature, then feed and lastly spindle speed. Also, Singh et al. (2008) developed a three-dimensional transient FEA model for laser-assisted micro-grooving of a mold steel and successfully predicted the temperature distributions of the heat-affected zone (HAZ) in the workpiece.

All the literature mentioned above is focused on laser-assisted turning, grinding, planing and micro-grooving. As for laser-assisted milling (LAMill), König and Zaboklicki (1992) first

showed its feasibility of cutting “difficult to machine” materials such as stellite 6. Jeon and Pfefferkorn (2008) successfully conducted laser-assisted micro end milling to improve the chip load and productivity in metal cutting. For ceramic materials, Shen and Lei (2004) initially did some numerical simulations for laser-assisted milling of silicon nitride, which were conducted through a transient three-dimensional heat transfer model using finite element analysis (FEA). With this model, a parametric study was conducted involving parameters of laser power, laser beam diameter, laser moving speed and preheat time. After this, Shen et al. (2005) improved that model (Shen and Lei, 2004) so that it could be used to predict the potential surface/subsurface cracks through thermal stress analysis. However, neither the material removal nor model validation was performed for both models. Later on, Yang et al. (2007) conducted a number of experiments of laser-assisted milling, but no thermal model was built for this operation. They indicated that as operating temperature increases, both the cutting force and specific cutting energy decrease. Yang and Lei (2008) further pointed out that once the operating temperature is higher than 1000°C, entry edge chipping was not observed. Exit edge chipping decreases considerably as the temperature increases. Tian et al. (2006, 2008) also did some experiments of laser-assisted milling of silicon nitride. The TiAlN coated carbide end mills were used. They indicated that there was a narrow range of material removal temperature (about 1200-1300°C) with the TiAlN coated carbide tools. Also, a transient three-dimensional thermal model was developed using finite volume method (FVM). However, the model only focused on laser heating without the material removal, and only the effect of laser power was discussed.

This study improves our previous FEA thermal model (Shen et al., 2005) by considering material removal, and the new model is validated through a series of experiments of laser-assisted milling of silicon nitride ceramics. Temperature simulation reveals that thermal gradients exist inside the workpiece in LAMill due to localized laser heating. Basically, for a successful LAMill, small thermal gradients in the workpiece are expected, especially over the cutting zone. They are strongly affected by the parameters of LAMill such as laser power, laser beam diameter, feed rate, feed, and cutting speed. Hence, through thermal analysis, guidelines for the parameter selection can be made and thus the thermal gradients over the cutting zone can be reduced. So far no literature has reported on the thermal analysis of the cutting zone in detail for LAMill. In addition, previous researchers usually neglected heat generation associated with machining in their thermal models, because they argued that the value was very small compared

with the energy from the laser source, while this study conducts simulations to explore its effect on the temperature at the cutting zone.

In the following sections, the FEA model is first introduced in detail and an example of temperature distribution is illustrated. Then, model validation is conducted via varying the parameters of laser power, feed and cutting speed. Finally, a guideline on parameter selection is provided for future laser-assisted milling operations.

3.2 Transient Three-Dimensional FEA Model

3.2.1 Mathematical Description of the Model

Figure 3.1 illustrates the schematic of laser-assisted milling of silicon nitride ceramics in this study. The laser is positioned in front of the milling cutter. Between the laser spot and the cutter, a small distance, laser-cutter allowance, is maintained in case the laser spot overlaps and damages the cutter. The workpiece is fed into the milling cutter along the z direction, which is clamped by an insulated vise so as to prevent the heat dissipation from the workpiece. The clamped areas (S_1) are shown in gray in Figure 3.1. The remaining areas on the workpiece surfaces are exposed to the surroundings.

The heat transfer model can be described by the following governing equation integrating over the volume of the workpiece:

$$\begin{aligned}
 & \underbrace{\int_{vol} \left(\rho c(T) \left(\frac{\partial T}{\partial t} \right) \right) d(vol)}_{\text{Change of the Internal Energy}} + \underbrace{\int_{S_4} (q_{con}'' d(S_2))}_{\text{Convection Energy}} + \underbrace{\int_{S_4} (q_{rad}'' d(S_2))}_{\text{Radiation Energy}} \\
 & = \underbrace{\int_{S_2} (q_l'' d(S_3))}_{\text{Energy from Laser Source}} + \underbrace{\int_{S_3} (q_{gen}'' d(S_4))}_{\text{Energy from Heat Generation in Machining}} + \\
 & \underbrace{\int_{vol} \left(\frac{\partial}{\partial x} \left(k(T) \frac{\partial T}{\partial x} \right) + \frac{\partial}{\partial y} \left(k(T) \frac{\partial T}{\partial y} \right) + \frac{\partial}{\partial z} \left(k(T) \frac{\partial T}{\partial z} \right) \right) d(vol)}_{\text{Conduction Energy}} \quad (3.1)
 \end{aligned}$$

where S_2 is the area covered by the laser beam (laser spot);

S_3 is the area where the cutter is in contact with the workpiece in one cut;

S_4 is the areas including all the workpiece surfaces open to the surroundings except S_2 , S_3 .

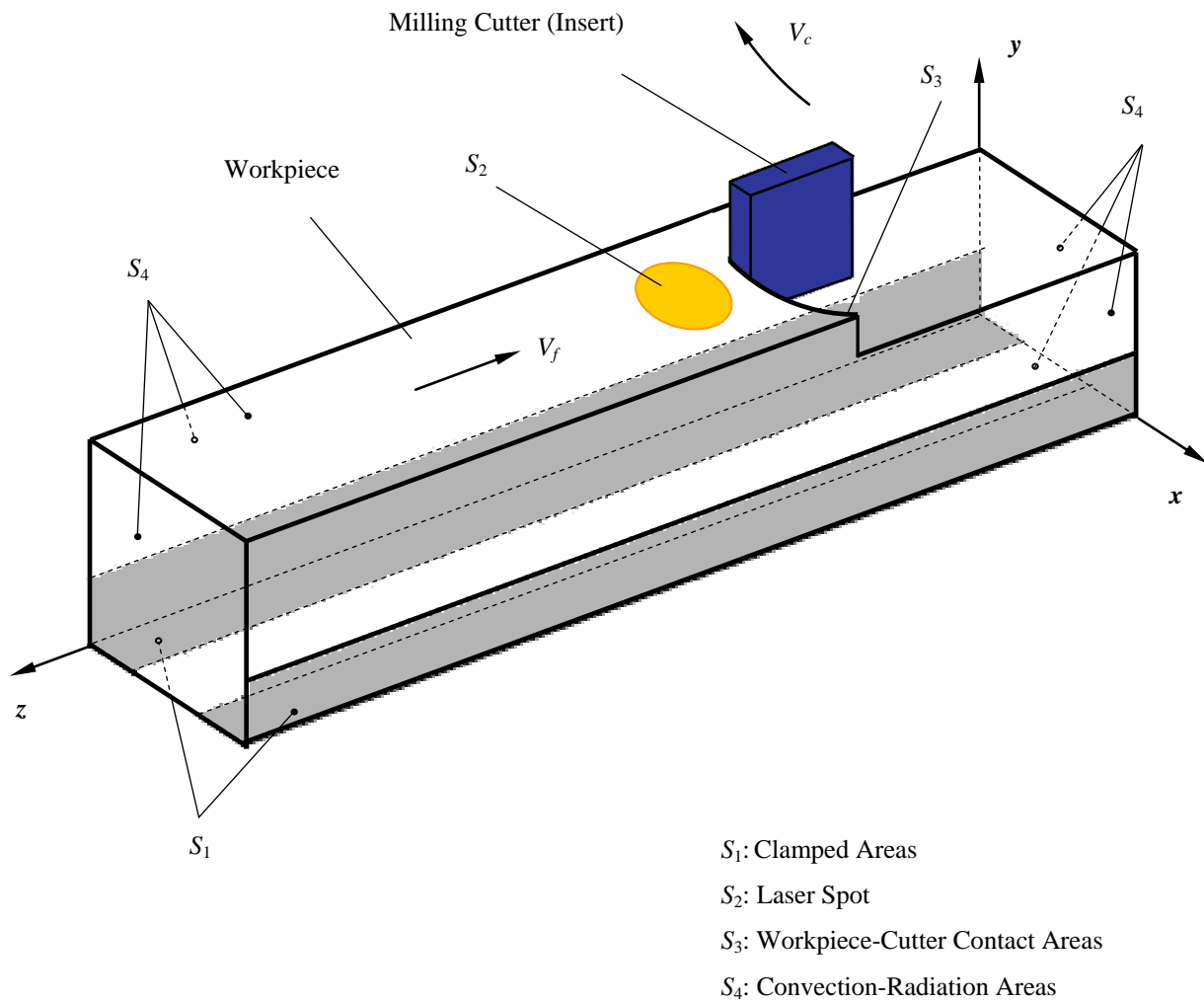


Figure 3.1 Schematic of laser assisted milling (LAMill)

In Equation (3.1), the first, second and third terms on the left-hand side represent the change of the internal energy, energy convection and radiation, respectively. The first term on the right-hand side represents input heat flux from the laser source. The second term shows the energy from the heat generation due to plastic deformation and tool-workpiece friction, which is associated with machining. The last term represents the energy conduction across the workpiece surfaces. Actually, for the whole volume of the workpiece, the final integration result of the last term is equal to zero because nothing contacts the workpiece except the insulating materials, which is considered to be adiabatic. However, for an element (or very small volume) inside the workpiece, the final integration result of the term is not zero.

The initial condition of the thermal model is

$$T(x, y, z, t)|_{t=0} = T_{\infty} \quad (3.2)$$

For the areas of S_1 , the boundary condition is considered adiabatic and defined by

$$\frac{\partial T}{\partial n} \Big|_{S_1} = 0 \quad (3.3)$$

In the area of S_2 , in addition to free convection and thermal radiation, there is also a heat flux from the laser source. Thus the boundary condition can be defined as

$$k \frac{\partial T}{\partial n} \Big|_{S_2, t>0} = q_l'' - q_{con}'' - q_{rad}'' \quad (3.4)$$

where q_l'' is heat flux from the laser;

q_{con}'' is convective heat flux, $q_{con}'' = h(T_s - T_{\infty})$;

q_{rad}'' is radiation heat flux, $q_{rad}'' = \varepsilon \sigma (T_s^4 - T_{\infty}^4)$.

For the area of S_3 , besides free convection and thermal radiation, there exists generated heat due to plastic deformation and tool-workpiece friction in machining. Thus the boundary condition can be represented by

$$k \frac{\partial T}{\partial n} \Big|_{S_3, t>t_p} = q_{gen}'' - q_{con}'' - q_{rad}'' \quad (3.5)$$

It should be noted that the surface of S_3 moves with the laser beam.

For the areas of S_4 , only free convection and thermal radiation exist and thereby the boundary condition can be expressed as

$$k \frac{\partial T}{\partial n} \Big|_{s_4} = -q_{con}'' - q_{rad}'' \quad (3.6)$$

3.2.2 Model Development Using FEA

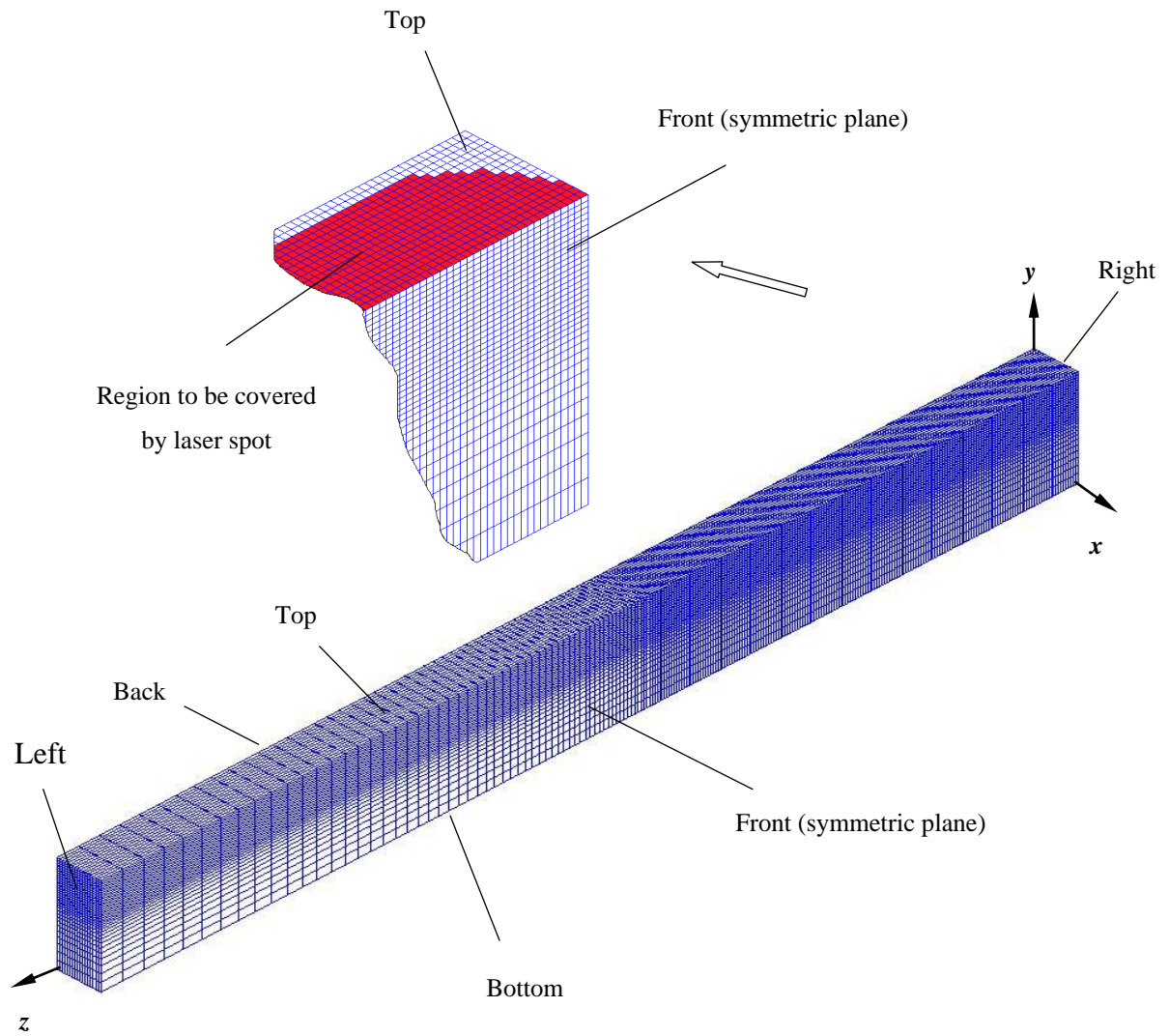
In this study, the thermal model is developed using the finite element package ANSYS 11.0 (ANSYS Inc.). The Finite element discretization solution: Newton-Raphson procedure is applied (see Appendix B). The dimensions of the model are the same as those of the actual workpiece with 4.3 mm in width (x direction), 5.3 mm in height (y direction) and 48 mm in length (z direction). Because of symmetry considerations only one-half of the workpiece is used in the model. As shown in Figure 3.2, the z direction is the laser moving direction. The region to be covered with laser beam is a long quasi-rectangular area located on the top face of the workpiece. Around the target machining portion, fine uniform meshes with brick shape are generated with the dimensions of $0.12_x \times 0.12_z \times 0.1_y$ mm, and beyond this portion, non-uniform meshes are used. The model has a total of $17_x \times 236_z \times 34_y$ elements and 149,310 nodes.

Still, some other features of the model are specified in the following.

(1) In this study, allowing for the existence of thermal gradients in the workpiece, the minimum temperature over the cutting zone is used as the operating temperature for material removal rather than the average one that some other work used (Rozzi et al., 1998a; Rebro et al., 2004; Pfeifferkorn et al., 2005; Tian and Shin, 2006; Tian et al., 2008). The purpose is to ensure that point-wise temperatures over the cutting zone exceed the softening temperature, say 1000°C (Lange, 1972; Hampshire, 1991), because there is considerable degradation of hardness and strength over that temperature for silicon nitride ceramics.

(2) In this study, the top-hat distribution of laser intensity replaces the Gaussian distribution in our previous work based on the laser profile measurement from the manufacturer (Visotek Inc.). As a result, an approximately uniform heat flux input, q_i'' , yields, assuming that the top-hat distribution is not altered for the inclination angle of 70 deg between the laser beam and the top face of the workpiece.

In order to apply the heat flux to the elements within the elliptic laser spot, it is roughly divided into $30_x \times 32_z$ square divisions due to the laser inclination. The division size (in the x and z directions), δ , is the same as the element size (in the x and z directions). The relative error



Element Number: $17_x \times 236_z \times 34_y$

Node Number: 149,310

Figure 3.2 FEA model with one half of the workpiece

between the power input for the simulation and the experimental value is 0.5%. Each division is specific to a corresponding element. As the laser spot moves, the location of each division is changed and the division corresponds to another element. In each moving step, the heat flux is applied to every laser-beam covered element and removed from every newly uncovered one. Note that the distance that the laser spot moves in each step is equal to the element size.

(3) Material removal in ANSYS is achieved through “killing” elements, which are deactivated by multiplying their stiffness (or conductivity, or other analogous quantity) by a severe reduction factor (say 1.0×10^{-8}). All the effects associated with deactivated elements are set to zero, such as element loads, mass, damping, specific heat, and others. But in the actual material removal process, the milling cutter contacts the workpiece with only one part of its nose edge (Figure 3.3), because the nose radius, r , of the cutter (0.787 mm) is much larger than the depth of cut of 0.2 mm. It is also noted that the cutter diameter of 76.2 mm is considerably larger than the workpiece width of 4.3 mm. Therefore, the cutting path on the workpiece can be approximated as a straight line, and the cross section of the cutting zone in any y - z plane can be seen in Figure 3.3.

The FEA mesh adopted in this study for the cutting zone is shown in Figure 3.4. The element size (in the x and z directions) and height (in the y direction) are selected to be five times the feed and half of the depth of cut, respectively. That is, two layers of elements beneath the top face of the workpiece will be “killed” once the cutter moves forward by five times of the feed. It should be mentioned that, in a mesh dependence study with an approximately 10-fold finer mesh for the cutting zone, the difference in simulation results was found to be about 1.2%, thus justifying the use of the course mesh in this study for the sake of computing efficiency.

(4) Heat generation associated with machining is considered in this model. The cutting energy, G_c , from the cutter in each cut can be approximated by the product of the main cutting force, F_c , and the moving length, L_w , as follows:

$$G_c = F_c L_w \times 10^{-3} \quad (3.7)$$

Since the mechanism of heat transfer at the cutting zone in LAMill is not fully understood at present, for simplification, the generated heat is assumed to transfer to the workpiece in a uniform heat flux, q''_{gen} . The area and the time of heat transfer in one step, δ , can be defined by the following equations, respectively:

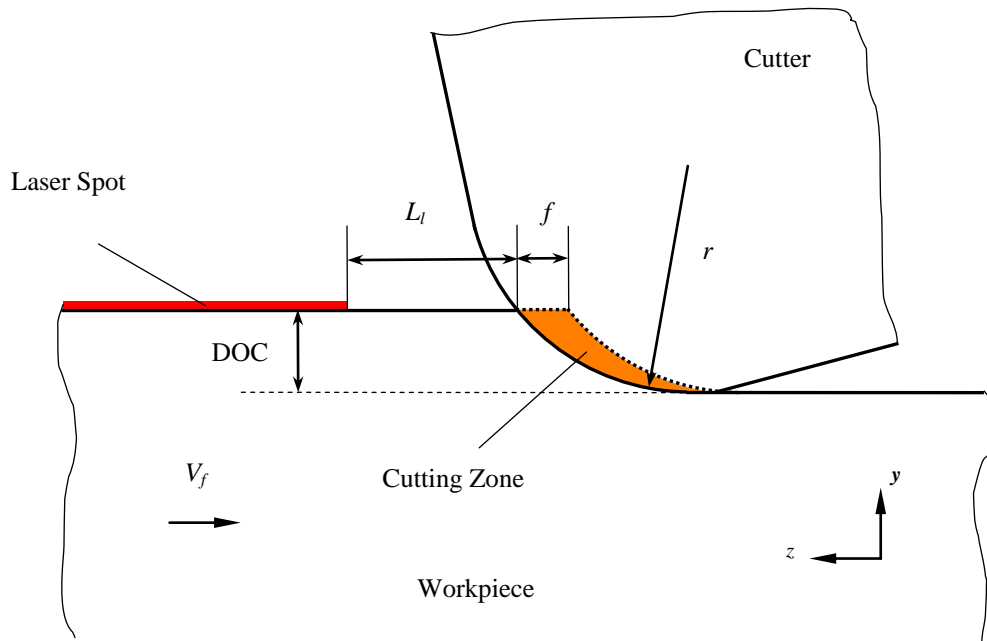


Figure 3.3 Schematic of cutting zone in face milling

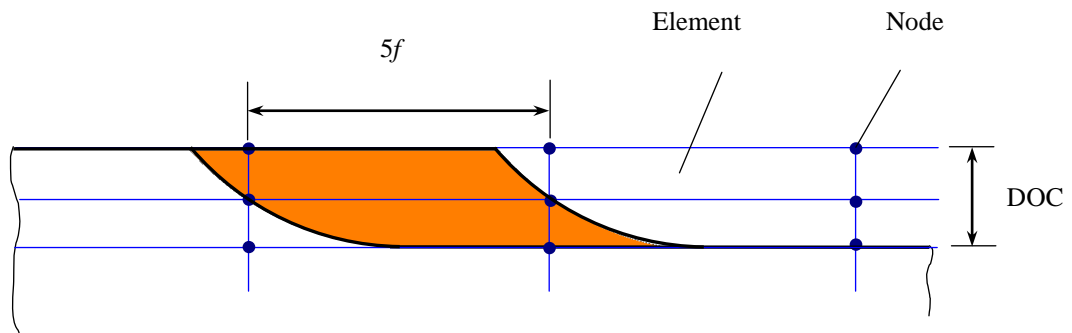


Figure 3.4 FEA mesh for the cutting zone

$$A_c = (L_w \cdot DOC) \times 10^{-6} \quad (3.8)$$

$$t_s = \frac{\delta}{V_f/60} \quad (3.9)$$

Actually, as the laser spot moves one step in simulation, correspondingly there are δ/f cuts in the actual machining. Hence, combining Equations (3.7-3.9), q_{gen}'' can be expressed as:

$$q_{gen}'' = \eta_h \eta_w \frac{E_c}{t_s A_c} \cdot \frac{\delta}{f} = \eta_h \eta_w \frac{16.7 F_c V_f}{f \cdot DOC} \quad (3.10)$$

where η_h is the ratio of the cutting energy eventually converted to heat;

η_w , is the ratio of the generated heat transferred to the workpiece.

Note that Equation (3.10) is only suitable for simulations.

(5) Free convection is reasonably assumed for the slow feed rate of the workpiece (< 1.0 mm/s). Localized laser heating in LAMill induces non-uniform temperatures on the workpiece surfaces; hence, for simplification, an average convection coefficient, \bar{h} , is used for the heated workpiece (Table 3.1). It is calculated by using the empirical correlations of Churchill and Chu (1975) for the vertical plate with external free convection flows and correlations of Goldstein et al. (1973) and Lloyd and Moran (1974) for the horizontal plate (Incropera and Dewitt, 1996).

The temperature-dependent emissivity values used in this study, ε , are obtained according to Touloukian (1967) and Sala (1986), which are listed in Table 3.1 together with a couple of extrapolated points for the high and low temperature end. The data of the temperature-dependent thermophysical properties of thermal conductivity and specific heat were provided by Ceradyne Inc. (Table 3.1).

The absorptivity of sintered silicon nitrides at 25°C (wavelength of 937 nm) found in the literature is 0.72 (Touloukian, 1967) and 0.56~0.75 (Touloukian and DeWitt, 1972). Zhang and Modest (1998) recommended 0.85 by measurements made for a hot-pressed silicon nitride. The laser wavelength they used is 1.06 μm , which is close to 937 nm in this study. They found that the absorptivity remains almost constant at 0.85 from 26°C to 1897°C. The above different values of absorptivity suggest that the surface absorptivity is affected by the compositions and production process of silicon nitride ceramic. The above values are somewhat not exactly the one our material has. Hence, based on plenty of experimental data, Shen and Lei (2008) indirectly obtained the absorptivity of 0.8 for sintered reaction bonded silicon nitride from a validated heat

Table 3.1 Thermal properties of silicon nitride

Temperature (K)	Emissivity, ε^*	Thermal Expansion Coefficient, β	Thermal Conductivity, k (W/m · K)	Specific Heat, c (J/kg · K)
400	0.94 [#]	0.22	25.1	810
600	0.9	0.51	21.4	960
800	0.86	1.20	20.0	1050
1000	0.83	1.93	19.2	1080
1200	0.8	2.62	18.1	1100
1400	0.77	3.40	17.3	1110
1600	0.75 [#]	3.80	17.0	1115

Note: *: Values from Touloukian (1967) and Sala (1986) and [#] from extrapolation;

Values of thermal expansion coefficient, thermal conductivity and specific heat provided by Ceradyne Inc.

transfer model, which was carried out via adjusting the absorptivity to match the predicted results with the measured ones. Note that the absorptivity is also affected by temperature (Siegal and Howell, 1981; Geng, 2004). However, the experiments of Zhang and Modest (1998) depicted that, below the decomposition temperature, the absorptivity of silicon nitride has very small variation. In addition, it should be mentioned that the surface oxidation and possibly generated silica (Shen and Lei, 2008) are ignored due to the very thin layer on the top face around the laser spot.

3.3 Experimental Setup

The experimental setup for laser-assisted milling of silicon nitride is illustrated in Figure 2.1. The milling operation is carried out on a CNC machine (Haas Automation Inc.). A diode

laser (Visotek Inc., DFL500, wavelength 937 nm) with a top hat power distribution is used to generate a high power laser beam, which is delivered through the optical fiber and strikes on the workpiece surface at the angle of 70 deg. A dynamometer (Kistler Inc., Type 9257B) is fixed on the worktable and utilized to measure the cutting forces in the x , y , and z directions. The air jet and shield are employed to prevent the optics from being overheated. The workpiece is clamped with an insulated vise which is mounted on the dynamometer. An infrared pyrometer (Williamson Inc., model 91-20-C-23D) with a range of 475-1750°C is used to concurrently measure the workpiece temperatures. Both the pyrometer and the laser are installed through holders on the spindle. All the data of temperature and force are digitally recorded by a computer.

Dozens of our experiments demonstrated that there was severe tool wear in laser-assisted milling of silicon nitride with commercial carbide mills; therefore, a house-made cutter with only one tooth and a polycrystalline cubic boron nitride (PCBN) insert was utilized. The purpose of this special design is to simplify the machining process and thus facilitate the analysis, because it always ensures that only one tooth contacts the workpiece during the milling process.

Figure 3.5 shows the initial positions of the laser and the pyrometer spots. Both of them are tangential to the edge of the right end face of the workpiece. For two reasons the measurement point of the pyrometer is not selected at the cutting zone on the top face of the workpiece. One reason is that, as the laser beam shines on the workpiece, silica bubbles may

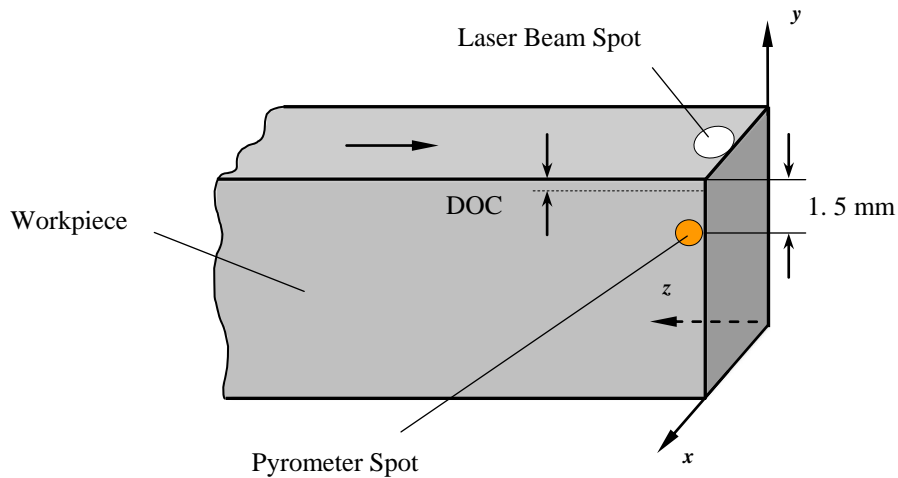


Figure 3.5 Positions of laser spot and pyrometer

continuously form on the top face of the workpiece (Shen and Lei, 2008), which may decrease the measurement accuracy of the infrared pyrometer. The other reason is that the minimum temperature over the cutting zone is of great concern in this study. Thus, the pyrometer spot is positioned on the side (front) face with a distance of 1.5 mm to the top face.

The Si_3N_4 workpiece (Ceradyne Inc, Ceralloy 147-31N) is a sintered reaction bonded ceramic (~8wt% additives) with dimensions of 4.3×5.3×48 mm, and its properties are provided by Ceradyne Inc. (Table 3.2).

Table 3.2 Properties of silicon nitride (25°C) (Ceradyne Inc.)

Property	Value
Density (kg/m^3)	3200
Flexural Strength (MPa)	800
Elastic Modulus (GPa)	310
Poisson Ratio	0.27
Fracture Toughness ($\text{MPam}^{1/2}$)	6.0

3.4 Simulation Results

3.4.1 Temperature Distributions of the Workpiece

Simulations are performed with different operating conditions. One typical simulation result is illustrated with temperature distributions in Figure 3.6. The cutting length, L_c , is 7.0 mm, and the operating conditions are: $P_l = 410 \text{ W}$, $V_c = 1.0 \text{ m/s}$, $f = 0.024 \text{ mm/tooth/rev}$, $V_f = 6 \text{ mm/min}$, $t_p = 12 \text{ s}$, $D_l = 3.6 \text{ mm}$, $DOC = 0.2$, and $L_l = 0.5 \text{ mm}$.

In Figure 3.6, the MN and MX symbols identify the locations of the minimum and maximum temperatures (the left face of the workpiece and the laser spot center), respectively. Note that the uniform interval is used in the contour display. The contour interval, defined as the difference between two adjacent contour lines, is around 140°C . Obviously, the region near the laser spot has higher temperatures (over 1000°C), which is verified by experimental

observations. In the experiments, the color of the material in that region turns into red and fades away to the surroundings. The approaching portion of the laser spot continuously absorbs energy from heat conduction and as a result, temperatures increase quickly, while the newly uncovered region is gradually cooling down due to free convection and thermal radiation. The geometrical widths of the contours in the x , y and z directions are not uniform and instead tend to increase from the laser spot to the surrounding portion. That is, along the x , y and z directions, the thermal gradients are becoming smaller. Contour display reveals that the laser heat source has a strong influence on the region around the laser spot and a weaker influence on the region beyond. Section A-A in Figure 3.6 passes through the cutting zone at the top face of the workpiece.

The minimum temperature point (MTP), as the term suggests, is defined as the point with the minimum temperature at the cutting zone. Usually, it is farthest from the laser spot center among the points in the cutting zone. It depends on the relative positions of the workpiece and the cutter, and it moves with the cutting zone. The temperatures at the MTPs should be kept higher than the material softening temperature in the milling process.

Figures 3.7 (a), (b) illustrate the cutting zone and its temperature contours obtained from simulations, respectively. Due to the very small feed, the surface area OCDE is considered here to represent the temperature distribution for the cutting zone. Point O is the location of the MTP and Point D is the maximum temperature point over the cutting zone. The temperature difference between them, also the maximum temperature difference over the cutting zone, is 120°C .

Figure 3.8 illustrates the temperature contours of the back face obtained from simulation. Point F is the MTP with a temperature of 1165°C . Assuming that another cutting is conducted, all the operating conditions are the same except that the depth of cut is set to be the nose radius of 0.787 mm. Then Point G is the MTP of the new cutting with a temperature of 1147°C . It means that, from the thermal aspects, a larger *DOC* is feasible under the current operating conditions. However, from the machining aspects, a very large *DOC* may cause severe surface/subsurface damage, which means that too much energy is deposited in the region not to be machined. The approach to prevent it is either to increase laser power or feed rate or both.

3.4.2 Effect of Heat Generation in Machining

As mentioned in Section 3.2.1, another factor that affects the thermal model is heat generation due to plastic deformation and tool-workpiece friction, which is associated with

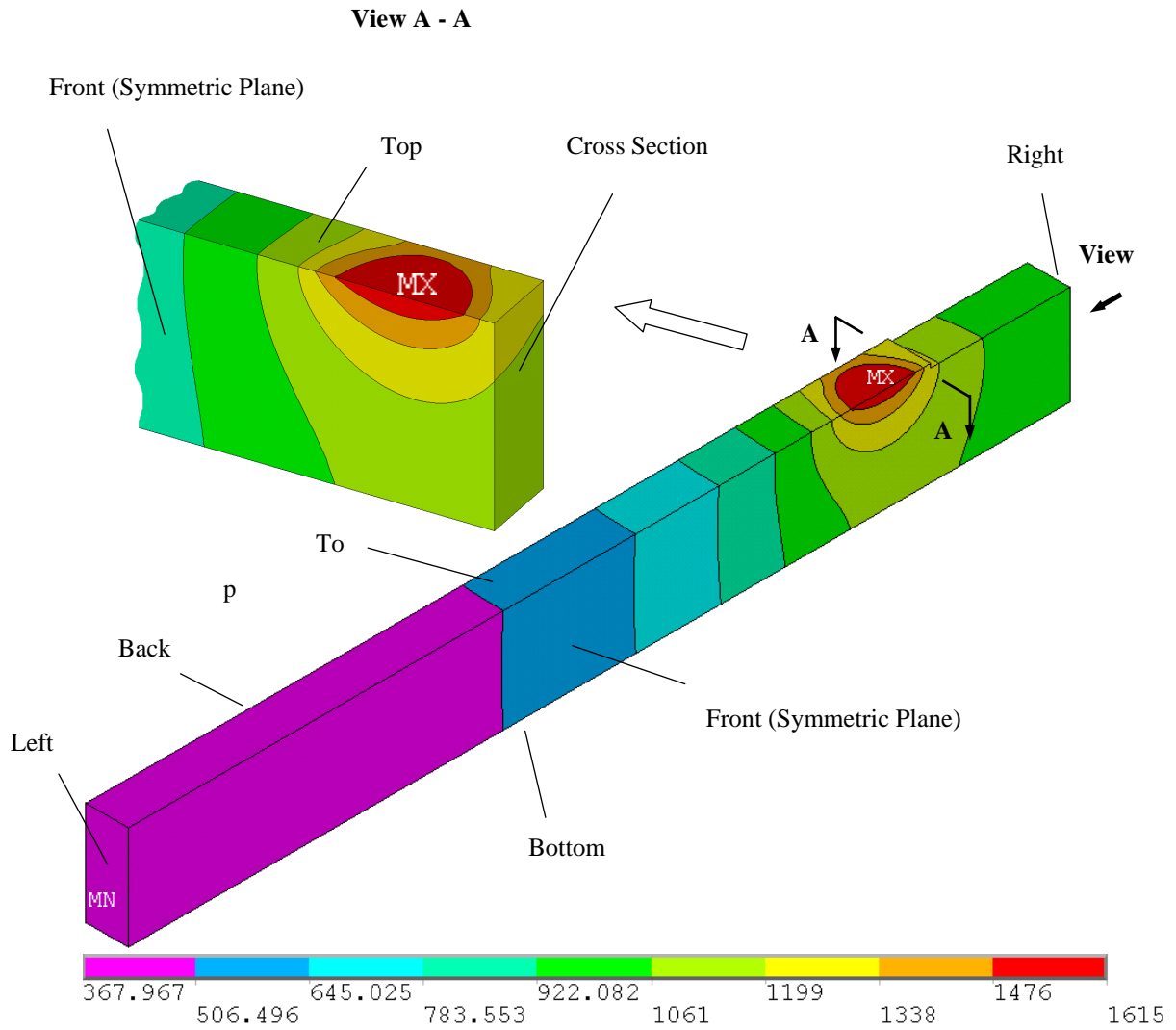


Figure 3.6 Temperature contours of the workpiece obtained from simulation
 ($P_l = 410$ W, $V_c = 1.0$ m/s, $f = 0.024$ mm/tooth/rev, $V_f = 6$ mm/min, and $t_p = 12$ s, $L_c = 7.0$ mm)

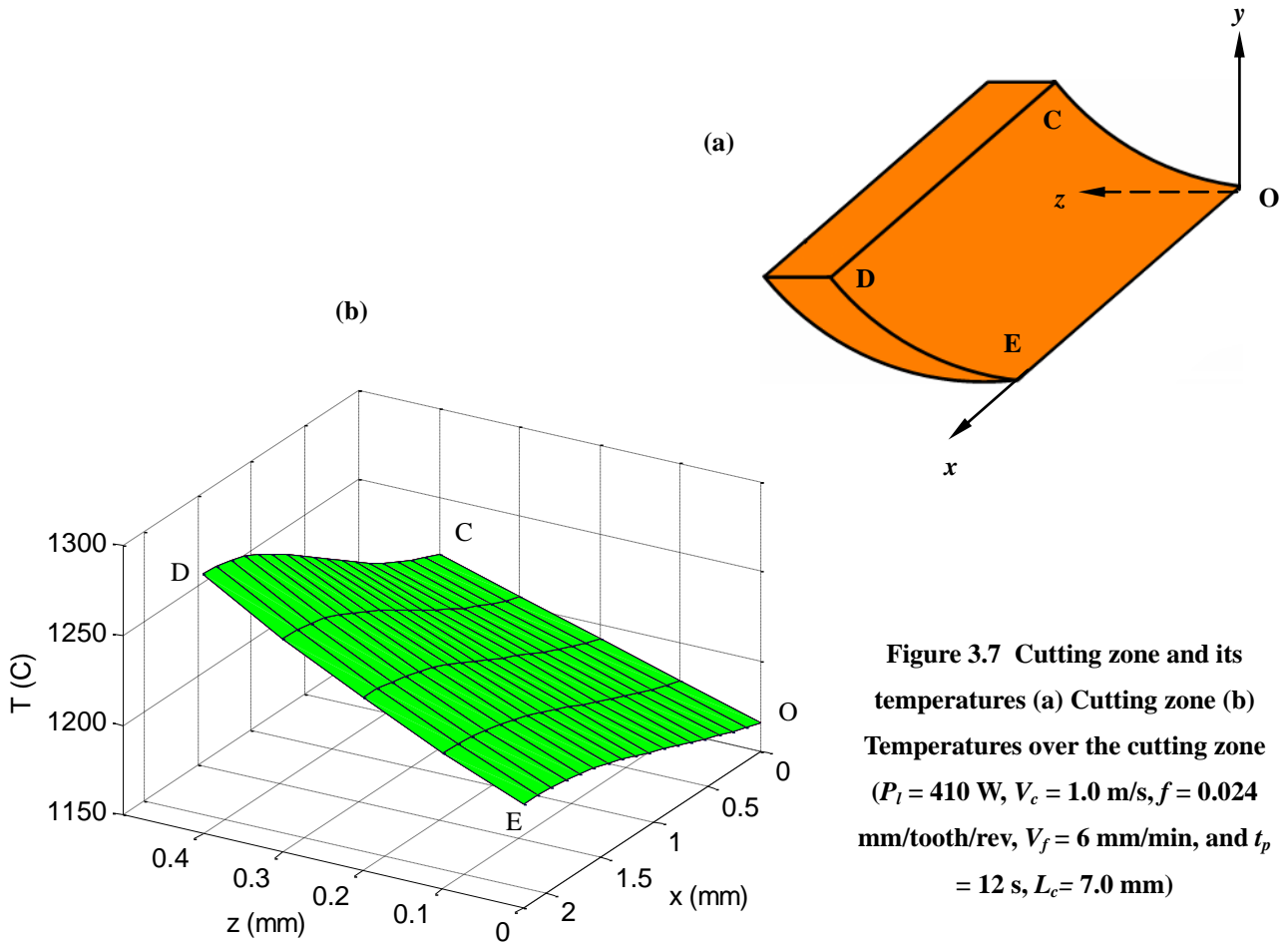


Figure 3.7 Cutting zone and its temperatures (a) Cutting zone (b) Temperatures over the cutting zone ($P_t = 410$ W, $V_c = 1.0$ m/s, $f = 0.024$ mm/tooth/rev, $V_f = 6$ mm/min, and $t_p = 12$ s, $L_c = 7.0$ mm)

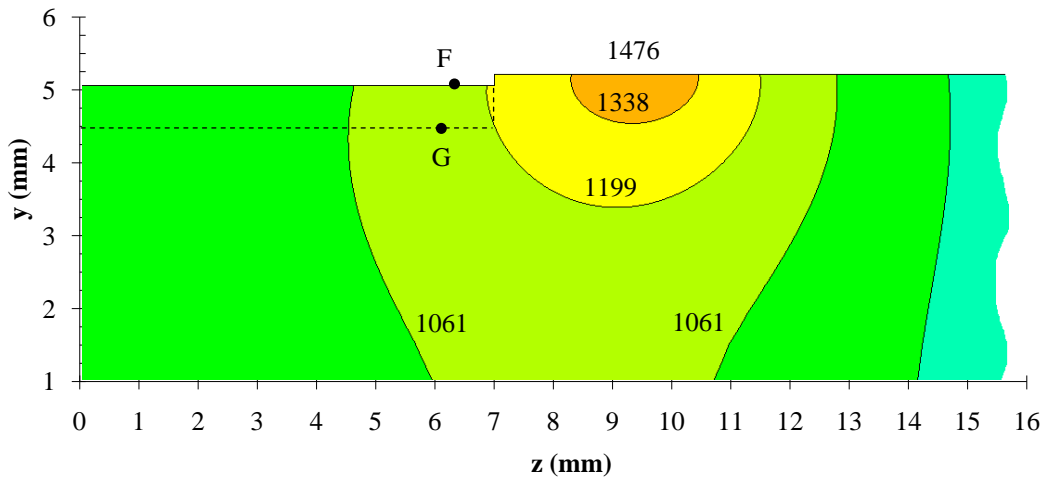


Figure 3.8 Temperature contours obtained on the back face from simulation ($P_t = 410$ W, $V_c = 1.0$ m/s, $f = 0.024$ mm/tooth/rev, $V_f = 6$ mm/min, and $t_p = 12$ s, $L_c = 7.0$ mm)

machining. In this model, heat generation is being treated. Although many studies indicate that the value is very small, few of them calculate it in detail. Since the ratio of the cutting energy converting to heat, η_h , and the ratios of the generated heat transferring to the cutter, the chips and the workpiece, respectively, are not well known, in order to assess the maximum possible effect of generated heat on the workpiece temperatures, the model assumes that all the cutting energy is converted to heat which dissipates into the workpiece ($\eta_h\eta_w = 1$).

Equation (3.7) indicates that the cutting energy is proportional to the main cutting force, F_c . our experimental results show that the average main cutting forces with depth of cut of 0.2 mm and cutting length of 1 mm are 8.6 N, 6.4 N and 2.2 N at operating temperatures of 1140°C, 1320°C and 1400°C, respectively. As expected, the average cutting force decreases as the operating temperature increases. In order to evaluate the effect of heat generation, the average cutting force of 9.8 N at the operating temperature of 1400°C is used as an example in this Section. The heat flux q_{gen}'' thereby yields $2.0 \times 10^5 \text{ W/m}^2$ according to Equation (3.10). However, comparing the results from considering heat generation with those not, the temperature discrepancies at MTP and maximum temperature point over the cutting zone are about 0.3°C and 2°C, respectively. That is, q_{gen}'' indeed can be neglected. In fact, the heat flux input from the laser source, q_l'' , is about 150 times of q_{gen}'' under these operating conditions, even with all the cutting energy being assumed to dissipate into the workpiece.

3.4.3 Uncertainty Analysis

There are some uncertainties involved in this study. These uncertainties originate from both measurements and simulations. For measurements, the uncertainty is mainly from pyrometer system error, $\pm 0.5\%$. For simulations, the uncertainties are mainly from: (1) laser beam diameter determination, $\pm 11.1\%$, which comes from the actual measurements of laser beam diameter; (2) the absorptivity of the workpiece (Zhang and Modest, 1998), $\pm 3.2\%$, which is considered due to temperature variations; (3) meshing and discretization of the model, 1.2%, which is from model meshing and calculations; (4) average convection coefficient (Incropera and Dewitt, 1996), $\pm 11.8\%$, which arises from non-uniform temperatures and different convection surfaces of the workpiece; and (5) laser power input, 0.5%, which is considered due to power difference between the simulation and the experiment (Section 3.2.2 (2)). The contributions of

these uncertainties to the simulation error also rank as above. For example, under the operating conditions: $P_l = 410$ W, $V_c = 1.0$ m/s, $f = 0.024$ mm/tooth/rev, $V_f = 6$ mm/min, $t_p = 12$ s, $D_l = 3.6$ mm, $DOC = 0.2$ and $L_c = 7.0$ mm, the temperature at MTP is 1165°C and the corresponding simulation error has upper and lower limits of 4.2% and 4.6%, respectively, which are determined via several simulations using all the possible combinations of the limit values of the above factors that can result in the uncertainties in LAMill and then finding the upper and lower limits. In addition, there are some uncertainties neglected in this model such as inhomogeneous properties of the material, surface oxidation, the air jet, and the insulating material.

3.5 Model Validation

To develop confidence in our FEA model, a series of experiments were conducted for validation purpose. Three groups of them are listed in Table 3.3. The operating conditions include the following parameters: laser power, P_l , laser beam diameter, D_l , laser moving speed, V_l , preheat time, t_p , depth of cut, DOC , feed, f , cutting speed, V_c , and tooth number, Z , laser-cutter allowance, L_l . V_l and V_f are linked through the following equation:

$$V_l = V_f = Zf \cdot RPM \quad (3.11)$$

Because of the relative motion between the laser and the workpiece, V_l is equal to feed rate, V_f . For convenience, in the following sections feed rate, V_f , will be used rather than the laser moving speed, V_l .

In this study, the parameters of laser power, feed, and cutting speed are the most important. The parameters of laser beam diameter, depth of cut, tooth number and laser-cutter allowance are fixed. The measurement points are shown in Figure 3.5. The temperatures at the MTP and maximum temperature point over the cutting zone are also predicted.

Figures 3.9-13 show the temperature histories under the operating conditions in Groups I and II (Table 3.3). Each of them includes four curves: Measurement, Simulation, Simu_MTP and Simu_Max, which represent experimental data, simulation data, predicted minimum and maximum data at the cutting zone, respectively. For uncertainty considerations, the curves of Measurement and Simulation are shown with the error bars. The curves of Simu_MTP and Simu_Max are not shown with the error bars because the difference between Simu_MTP and Simu_Max, also the maximum temperature difference over the cutting zone, is the most important. The curves of Measurement and Simulation show that the temperatures quickly rise to

Table 3.3 Operating conditions of laser-assisted milling of Si₃N₄

	Laser power (W)	Feed (mm/tooth/rev)	Cutting Speed (m/s)	Feed rate (mm/min)	Preheat time (s)	Laser Beam Diameter (mm)	Depth of Cut (mm)	Laser-Cutter Allowance (mm)
Group I	300	0.024	1.0	6	15	3.6	0.2	0.5
	410				12			
	470				8			
Group II	410	0.012	1.0	3	12	3.6	0.2	0.5
		0.024		6				
		0.048		12				
Group III	410	0.024	0.5	3	12	3.6	0.2	0.5
			1.0	6				
			2.0	12				

a peak value and then gradually go down. This is because during preheating, the position of the laser beam is fixed. After that time the measurement spots start to move with the workpiece. Furthermore, the maximum temperature differences over the cutting zone are found to increase gradually as the workpiece moves. The reason is that the insulating materials are not ideally adiabatic. The simplified boundary conditions in the model actually neglect the heat transfer between the insulating materials and the vise, thus causing the predicted temperatures higher than the measured ones. As the temperatures go up, the heat transfer speed increases and as a result, the differences further increase. However, once the thermal system is in a quasi-steady state, the differences tend to maintain a constant value, but they are still in the range of error bars shown in Figures 3.9-3.13. In addition, it is noted that the maximum temperature difference over the cutting zone maintains nearly constant as the thermal system is in a quasi-steady state condition, which means that the thermal gradients inside the cutting zone no longer change with the workpiece moving.

Figures 3.9-3.11 show the temperature histories with the laser power of 300, 410 and 470 W, respectively. The cutting speed and feed are fixed. As expected, the higher the laser power, the more heat energy the workpiece absorbs, and the higher temperatures the workpiece has. The

laser power of 470 W has the highest MTP temperatures among all these three cases. The maximum differences over the cutting zone for the power of 300, 410 and 470 W are 100°C, 120°C and 139°C, respectively. That is, the thermal gradients inside the cutting zone have a small increase as the laser power goes up.

Figures 3.12, 3.10 and 3.13 show the temperature histories with feed of 0.012, 0.024 and 0.048 mm/tooth/rev, respectively. The laser power and cutting speed are fixed. According to Equation (3.8), the feed variation is related to feed rate variation. Although the parameters in these three cases are the same except for the feed and feed rate, the peak temperatures are different. This is because the peak temperature does not usually occur at the preheating stage, instead it often happens at some time after the preheating stage. The value of the peak temperature depends on feed rate. A smaller feed rate can result in a higher value. It is noted that the maximum temperature differences over the cutting zone for these three cases are almost the same (120°C). The feed variation does not alter the thermal gradients inside the cutting zone as feed varies.

In Group III (Table 3.3), the parameters of laser power and feed are fixed, and cutting speed changes as 0.5, 1.0 and 2.0 m/s, respectively. Similar to the change of feed, cutting speed variation is also related to feed rate variation. Actually, both cutting speed and feed affect the temperatures via varying feed rate. However, once the feed rate is fixed, from the thermal aspects, they have little impact on temperatures because their contributions to heat generation are so small that it can be ignored. In fact, Groups II and III have almost the same thermal results, which are demonstrated via both experiments and simulations.

In summary, Figures 3.9-3.13 show that the predicted temperature results are in good agreement with the measured ones. It is reasonable to declare that the model can successfully predict temperature distributions of the workpiece under different operating conditions.

3.6 Guidelines on Parameter Selection

Three basic criteria are summarized for the smooth operation of laser-assisted milling: (1) the minimum temperatures over the cutting zone should exceed the material softening temperature in the milling process; (2) the thermal gradients over the cutting zone should be as small as possible; and (3) The temperatures of the workpiece should be lower than the decomposition temperature of silicon nitride so as to avoid possibly damaging the machined surface. To this end,

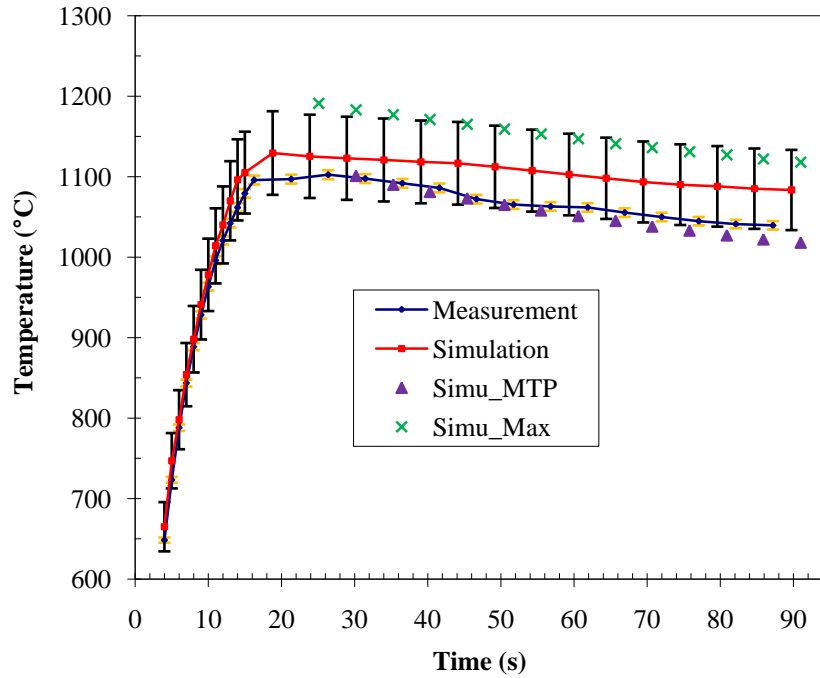


Figure 3.9 Temperature histories with $P_l = 300$ W
 ($V_c = 1.0$ m/s, $f = 0.024$ mm/tooth/rev, $V_f = 6$ mm/min, and $t_p = 15$ s)

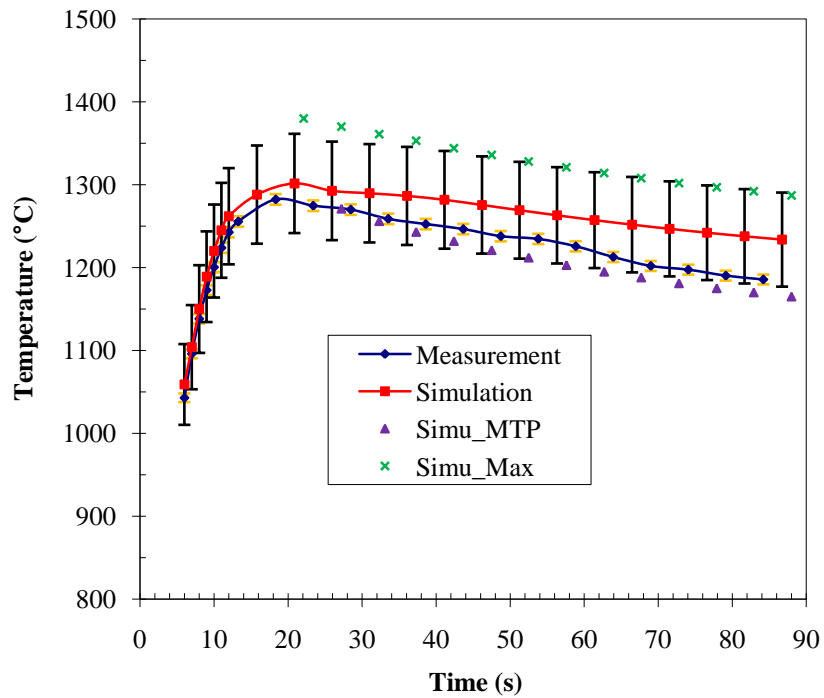


Figure 3.10 Temperature histories with $P_l = 410$ W
 ($V_c = 1.0$ m/s, $f = 0.024$ mm/tooth/rev, $V_f = 6$ mm/min, and $t_p = 12$ s)

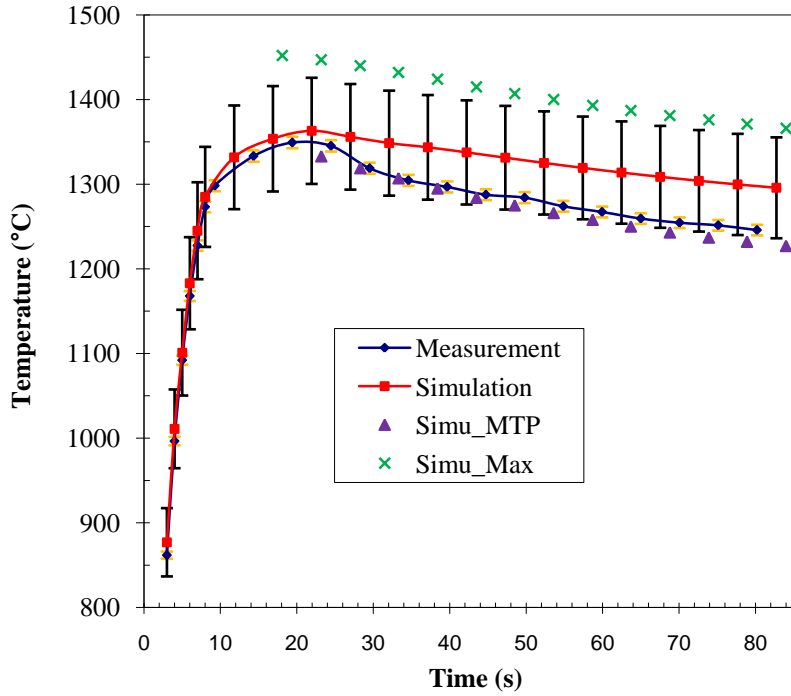


Figure 3.11 Temperature histories with $P_t = 470$ W
 ($V_c = 1.0$ m/s, $f = 0.024$ mm/tooth/rev, $V_f = 6$ mm/min, and $t_p = 8$ s)

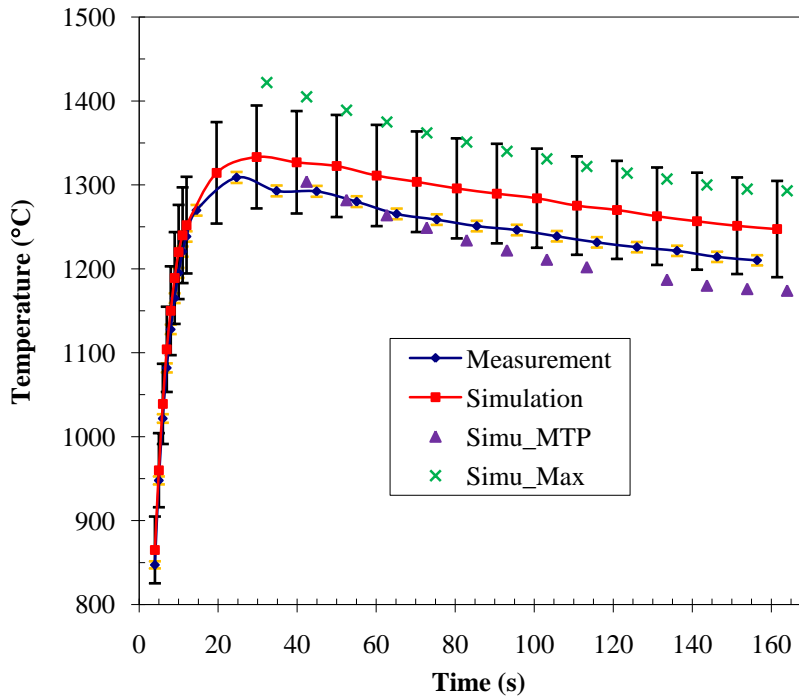


Figure 3.12 Temperature histories with $f = 0.012$ mm/tooth/rev
 ($P_t = 410$ W, $V_c = 1.0$ m/s, $V_f = 3$ mm/min, and $t_p = 12$ s)

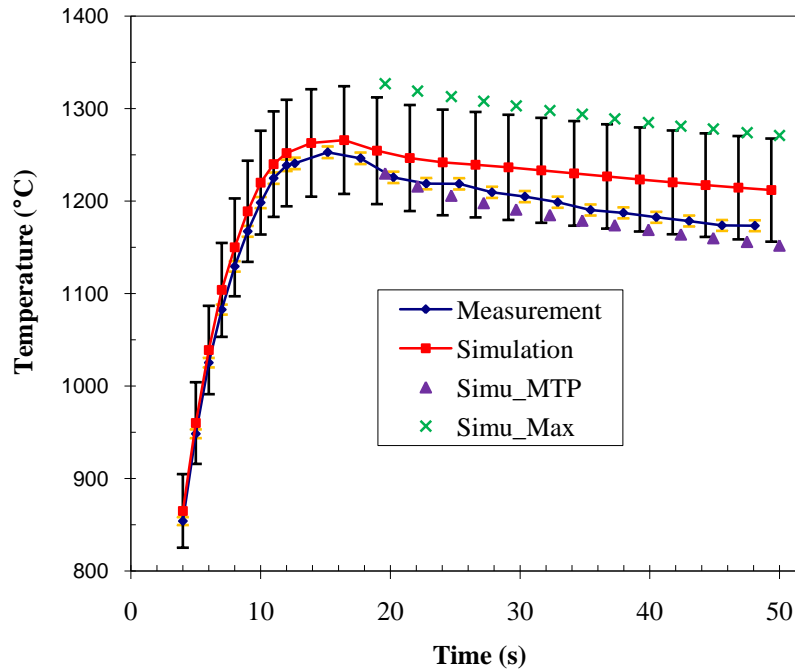


Figure 3.13 Temperature histories with $f = 0.048$ mm/tooth/rev

the parameters in laser-assisted milling should be selected carefully.

The forgoing analysis shows that the parameters of laser power and feed rate dominantly determine the temperature distribution of the workpiece. Feed and cutting speed can also play an important role via varying feed rate. However, once feed rate is fixed, feed and cutting speed themselves have little impact on workpiece temperature. Hence, to meet the three basic criteria, a high laser power is strongly recommended, but high laser power will increase the thermal gradients inside the cutting zone. Hence, a compromise should be made between them. Once laser power is determined, feed rate should be selected appropriately so as to keep the temperature change as small as possible. According to Equation (3.11), there are three ways to regulate feed rate: feed, spindle speed and tooth number.

Compared with depth of cut, the feed is so small over the cutting zone that the temperature difference can be neglected in the feed direction (Figure 3.3). That is, from the thermal aspects, the feed can be increased appropriately so that the material removal rate (MRR) can be improved.

It is noted that the nose radius of the milling cutter can also affect the temperatures at the MTPs. As shown in Figure 3.3, the smaller the nose radius, the shorter the distance from the

MTP to the laser spot, and thus the higher the temperatures at the MTPs. Thus the nose radius of the milling cutter is expected to be as small as possible.

3.7 Conclusions

A transient three-dimensional heat transfer model for laser-assisted milling is developed and validated through comparing the predicted temperatures with the experimental ones. Simulation results show that heat generation associated with machining can be neglected. The predicted temperatures at the MTPs can be used to evaluate the operating temperatures under various operating conditions. Laser power is one critical parameter for successful laser-assisted milling operations. High laser power is strongly recommended. Both feed and cutting speed can affect the operating temperatures by varying feed rate. Once feed rate is fixed, they have little impact on the operating temperatures.

Chapter 3 - Creation of the Synthetic Material for Machining Simulation Using Distinct Element Method *

In order to simulate the dynamic process of laser-assisted machining (LAM) of silicon nitride ceramics, a synthetic material must be first created with the distinct element method (or discrete element method, DEM), whose macroproperties are calibrated with the corresponding physical properties of the real silicon nitride material. Thus, in this chapter, the creation of the synthetic material is focused. The numerical tests (compression, bending, and fracture toughness tests) used in the calibration process are introduced in detail. Furthermore, the requirements for the reasonable specimen dimensions for machining simulation are provided.

4.1 Introduction

Advanced structural ceramics have high strength and hardness, outstanding wear resistance, good chemical stability, etc. Their thermal-mechanical dynamic behavior is well recognized as controlled by the microstructures (Rühle, 1985; Lee and Rainforth, 1994). In order to simulate the microstructures, various numerical models were developed for different purposes. Some models were used to study the microstructural development, thus improving the ceramic properties. For example, Monte Carlo method was applied to simulate sintering and grain growth formation (Matsubara, 1999; Wang et al., 2005). Probabilistic models, based on the closed random sets and tessellation, were used to describe the morphology of grains (Chermant and Coster, 2002). Some models were established to analyze the crack initiation and formation under loading. For example, Zavattieri et al. (2001) presented a dynamic finite element analysis (FEA) model to simulate microcracking at grain boundaries and subsequent large sliding opening and closing. Maiti and Geubelle (2004) developed a grain-based cohesive/volumetric FEA model to investigate dynamic propagation and branching of a mode I crack. Also, some models were developed with the distinct element method (or discrete element method, DEM) to study the

The contents of this Chapter are from my following journal paper:

* **Shen, Xinwei** and Lei, Shuting (2009). Numerical modeling and simulation of laser-assisted machining of silicon nitride ceramics with distinct element method: part I, creation of the synthetic specimen for machining simulation. *Journal of Manufacturing Science and Engineering, Transactions of the ASME*, (under review).

deformations and damages of brittle materials under dynamic loading.

As for the DEM, it was first introduced by Cundall for the analysis of rock-mechanics (Cundall, 1971). In recent years, besides rock (Hazzard et al., 2000; Potyondy and Cundall, 2004), the method was also applied to model other materials such as concrete (Tavarez et al., 2002; Shiu et al., 2008), silicon (Tan et al., 2008a), composite (Wittel et al., 2003) and ceramics (Kotrc and Uebel, 2005). Furthermore, it was extended to simulate the material removal of rock (Huang, 1999; Lei and Kaitkay, 2002; Ledgerwood, 2007), silicon (Tan et al., 2008a) and ceramics (Shen and Lei, 2005; Tan and et al., 2008b).

Different from our previous work (Shen and Lei, 2005, Shen and Lei, 2009a), this paper gives a complete description of microstructural modeling of β -Si₃N₄ ceramic. Cluster breakage in machining is considered, the calibration guidelines for the numerical tests are provided and the material strengths are selected from a Weibull distribution instead of a normal distribution. The objective is to provide an effective approach to model a ceramic material at the microstructural (grain) level for studying the deformation and damage evolutions of the material under dynamic loading. Especially material removal in laser-assisted machining (LAM) is investigated in the companion paper (Shen et al., 2009). In the following sections, the relationship between the DEM and advanced ceramics is first elucidated. Then, microstructural modeling of silicon nitride is conducted covering the synthetic material creation and the microstructural analysis. Finally, the requirements are presented for the creation of a reasonable synthetic specimen for machining.

4.2 DEM and Advanced Ceramics

The DEM (Itasca, 2002) argues that cracks occur once a large enough compression force is applied to rock as shown in Figures 4.1a and 4.1b. The similar crack-inducing mechanism also occurs when a rock is replaced by bonded circular particles as shown in Figure 4.1c. Imagine that many more similar breakages would occur inside an assembly which contains thousands of such bonded circular particles. This situation to some extent describes the occurrence of crack formation and propagation in a material under loading. Hence, it is suggested that the DEM can be used to model a rock and handle the crack interaction, constitutive behavior, fracturing bodies, etc. The above crack-inducing mechanism can also be applied to other brittle materials. Commonly, the particles in the DEM are treated as rigid bodies that are capable of “overlapping” at contact points as an alternative to reflect individual deformation. The interaction between

particles is treated as a dynamic process in which the equilibrium state is reached whenever the internal forces balance. The movement of particles can also be used to reflect the deformations of the material.

In contrast with continuum methods (e.g., FEA model), the DEM model can describe non-linear behavior and localization with accuracy and treat the material inhomogeneity as well. Moreover, it can handle the complex particle contact physical processes with coupled shear and bulk deformation effects. Hence, it has great advantages to model the microstructures of brittle materials such as advanced ceramics which are of great concern in this study. With inherent granular nature, advanced ceramics can be envisioned as an assembly with thousands of particles bonded together. Figure 4.2 illustrates the microstructure of a typical dense ceramic made from powders (Lee and Rainforth, 1994). It has a fine grain size with occasional pores and a grain boundary glassy phase. The grain boundary glassy phase arises from solidification of a liquid phase formed during densification. The grains account for the majority of the microstructure. In this study, a sintered reaction bonded silicon nitride (β -Si₃N₄) is used with 8wt% additives.

4.3 Microstructural Modeling of a Silicon Nitride Material

In this section, a distinct-element code, PFC^{2D}, is used to model the microstructure of a β -Si₃N₄. The resulting material, so called synthetic material, is evaluated through the numerical tests so that its behavior is imparted to resemble that of the real silicon nitride.

4.3.1 Creation of Synthetic Silicon Nitride Material

Table 4.1 lists the microparameters required to characterize a synthetic material with parallel bonds and clusters in the DEM. The material strengths are selected from a Weibull distribution rather than normal distribution in our previous work. Table 4.2 provides the parameters that are used to control the material-creation procedure including geometric and physical parameters such as specimen dimension, particle size and so on. A synthetic specimen is illustrated in Figure 4.3 containing 7468 circular particles which are densely packed and parallel-bonded.

The creation of the synthetic material follows the material-creation procedure which can be summarized as four steps (Itasca, 2002): (1) generating an initial compact assembly, (2) installing specified isotropic stress, (3) reducing the number of “floating” particles, and (4)

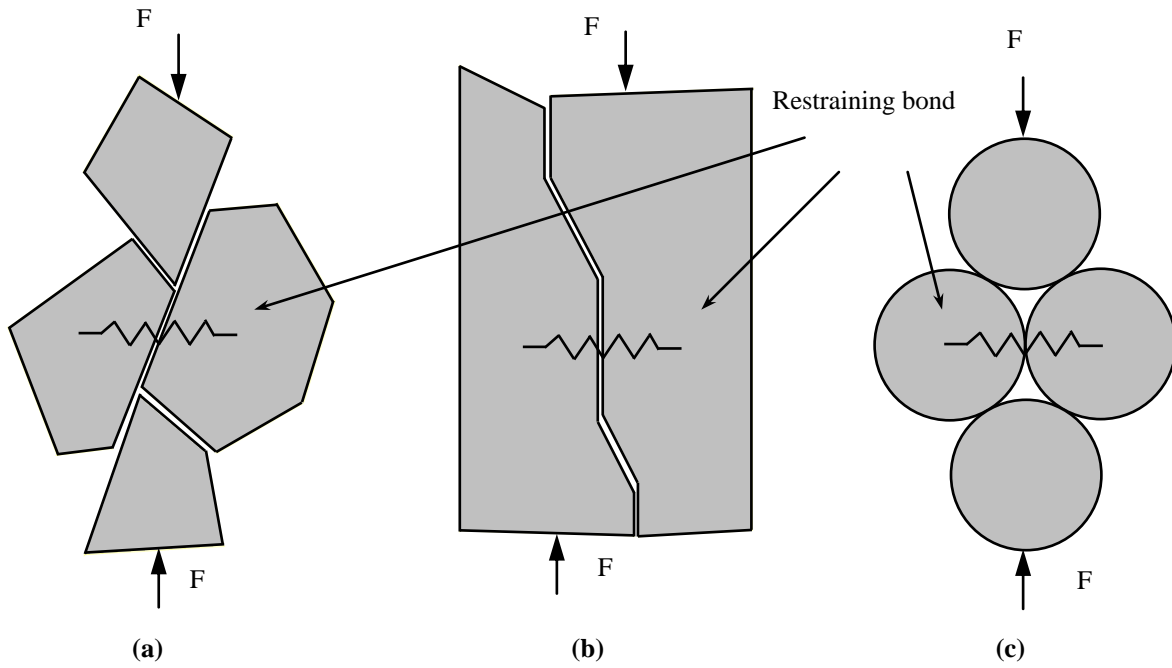


Figure 4.1 Physical mechanism for axial cracking (Itasca, 2002) (a) Wedge cracking (b) Staircase cracking (c) Idealization as bonded circular particles



Figure 4.2 The microstructure of a typical dense ceramic (Lee and Rainforth, 1994)

Table 4.1 Microparameters that define the DEM material

Parameter	Value
Particle density, ρ (kg/m ³)	3200
Particle-particle contact modulus, E_c (GPa)	272
Parallel-bond modulus, \bar{E}_c (GPa)	
Particle stiffness ratio, k_n/k_s	2.85
Parallel-bond stiffness ratio, \bar{k}^n/\bar{k}^s	
Particle friction coefficient, μ	0.4
Particle damping coefficient, η	0.012
Parallel-bond radius multiplier, $\bar{\lambda}$	1.0
Parallel-bond normal inter-cluster strength, mean, $\bar{\sigma}_{c,mean}$ (GPa)	2.1
Parallel-bond shear inter-cluster strength, mean, $\bar{\tau}_{c,mean}$ (GPa)	1.3
Parallel-bond normal intra-cluster strength, mean, $\bar{\sigma}'_{c,mean}$ (GPa)	10.5
Parallel-bond shear intra-cluster strength, mean, $\bar{\tau}'_{c,mean}$ (GPa)	6.5

finalizing the specimen. In Step (1), a rectangular specimen is generated consisting of arbitrarily-
place particles confined by four frictionless walls. In Step (2), the radii of all the particles are
changed uniformly to achieve a specified isotropic stress. The purpose is to reduce the magnitude
of the locked-in forces developing after the subsequent bond-installation and specimen-
unloading. In Step (3), the “floating” particles, defined as having less than three contacts, are
eliminated so that a denser network of bonds is obtained in the subsequent bond-installation step.
In Step (4), the parallel-bonds are installed throughout the assembly between all particles that are
in physical contact. All the particles are then assigned a friction coefficient. Note that packing

Table 4.2 Parameters that control the material-creation procedure

Parameter	Value
Specimen height, H (mm)	0.13
Specimen length, L (mm)	0.26
Specimen thickness, b (mm)	0.4
Average particle radius, R_{av} (μm)	1.1
Particle size ratio, R_{max}/R_{min}	1.2
Cluster size, N_c	5
Wall normal stiffness multiplier, β_w	1.1
Locked-in isotropic stress, σ_o (MPa)	-1
Remaining floaters ratio, N_f/N	0
Minimum number of contacts to be a non-floater, N_f	3

arrangement of the particles has a minor effect on the behavior of the DEM model (Potyondy and Cundall, 1999).

4.3.2 Microstructural Modeling of $\beta\text{-Si}_3\text{N}_4$

The microstructure of the $\beta\text{-Si}_3\text{N}_4$ can be characterized from the following aspects:

Parallel Bonds

As is known, silicon nitride ceramics are fabricated by alloying Si_3N_4 powder with sintering additives such as metal oxides and nitrides. At the sintering temperature, the additives combine with the SiO_2 oxidation layer on the Si_3N_4 powder raw material to form a liquid which wets the Si_3N_4 . After cooling, the liquid phase solidifies into intergranular glass phase at the grain boundaries (Hampshire, 1986; Falk et al., 2007). Figure 4.4 provides a clear image of the microstructure of the material used in this study. In this image, the physical adhesion among the rod-like grains is attained with the amorphous intergranular glass phase. This role is played by

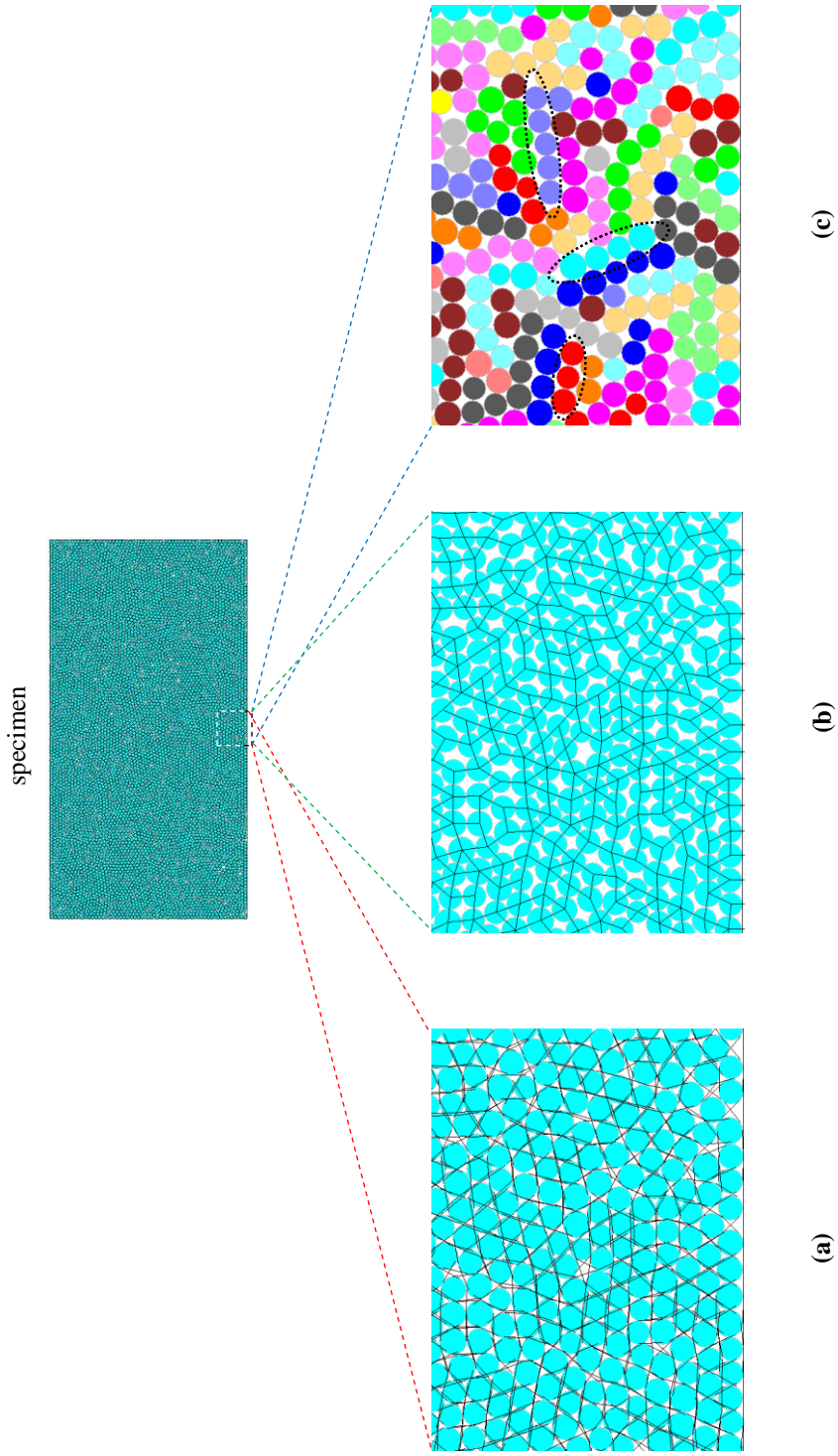


Figure 4.3 Synthetic specimen
(a) Colored clusters (b) Parallel-bond network (c) Contact network

parallel bonds (Figure 4.3b) in the microstructural modeling to join the clusters which mimic the grains. The voids between particles are imagined to fill with virtual intergranular glass phase. Jin et al. (2001) indicated that the intergranular glass phase occupies about 10% in the sample. Thus, the porosity of the assembly in this model is accordingly selected to be 10%.

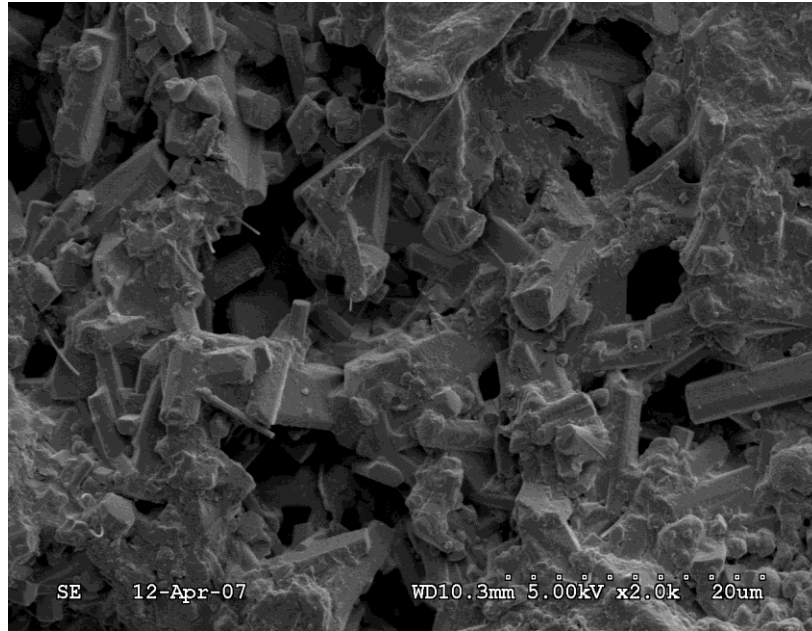


Figure 4.4 SEM image of a β -type silicon nitride ceramic

A parallel bond in the DEM approximates the physical behavior of a finite-sized piece of cementing material deposited between two particles (Itasca, 2002). It can be viewed as a set of elastic springs uniformly distributed over a rectangular cross section lying on the contact plane and centered at the contact point (Figure 4.5). Force and moment can be transmitted between particles via parallel bonds.

The force vector between particles can be resolved into normal and shear components with respect to the contact plane and expressed as

$$\bar{F}_i = \bar{F}_i^n + \bar{F}_i^s \quad (4.1)$$

where \bar{F}_i^n and \bar{F}_i^s denote the normal and shear component, respectively.

Thus, the maximum tensile and shear stresses acting on the bond periphery can be

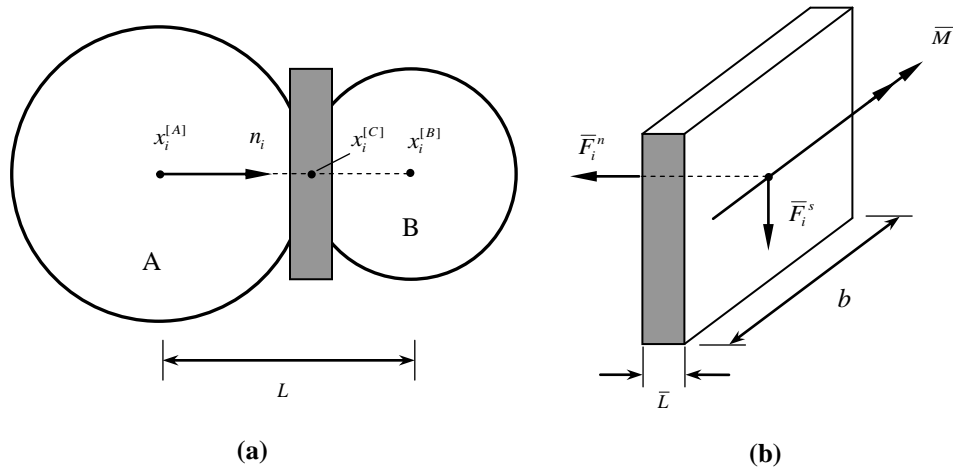


Figure 4.5 Parallel-bond (Itasca, 2002)

(a) Parallel-bond idealization (b) Forces carried in the bond material

derived as

$$\sigma_{\max} = \frac{-\bar{F}^n}{A} + \frac{|\bar{M}|}{I} \bar{R} \quad (4.2)$$

$$\tau_{\max} = \frac{|\bar{F}_i^s|}{A} \quad (4.3)$$

Where \bar{F}^n is the scalar value of \bar{F}_i^n ;

A is the area of the bond cross section with $A = 2\bar{R}b$;

I is the moment of inertia of the bond cross section with $I = (2/3)\bar{R}b^3$ (b is the particle thickness and also specimen thickness);

\bar{M} is the elastic moment developing in the parallel bond;

\bar{R} is the bond radius and equals radius multiplier ($\bar{\lambda}$) times the minimum radius of the two contacting particles.

Clusters

Clusters are groups of particles that are physically bonded together and thus form some different geometrical shapes. In this study, the particles in a single cluster are packed in a line so as to represent the individual real rod-like grain. Different clusters are painted by different colors

in Figure 4.3c. The intra-cluster strengths (i.e., the strengths of all bonds between two particles within a single cluster) are specified to such high values that the bond-breakage event is allowed to first occur between clusters rather than within clusters. The reason is that for a silicon nitride material, the intergranular glass phase may experience the situations such as glass transition phenomena, crystallization and liquid phase as the temperature changes. As a result, it has a direct effect on strength, fracture toughness, creep rate or thermomechanical stability (Rouxel, 2002). Also, the silicon nitride grains do not deform plastically due to very little dislocation movement (Petzow and Greil, 1988). This feature can be reflected in the synthetic material as well. In contrast with the inter-cluster strengths, the intra-cluster strengths are found to have very small effects on the macroproperties of the synthetic material. Note that the ratio between the intra- and inter-cluster strengths in this study is specified to 5 instead of a significant value (10^{20}) in our previous work. The purpose is to allow clusters to be broken during cutting. Although the accurate value of the ratio has not been found in literature so far, one truth is that the grain strength is much larger than that of the intergranular glass phase even at high temperatures (Wiederhorn et al., 1994).

In addition, the average grain size and the maximum grain aspect ratio are estimated to be $2.2 \mu\text{m}$ and 5, respectively. Note that the more detailed grain information can be obtained through stereological analysis (Müecklich et al., 1999). Accordingly, their corresponding parameters in the DEM model, the average particle diameter and cluster size, are selected to be $2.2 \mu\text{m}$ and 5, respectively. Cluster size is defined as the maximum particle number within a single cluster.

It should be mentioned that although there are some differences between the microstructures of the synthetic and the real materials due to lack of some knowledge so far, the ultimate macroproperties of the synthetic material are ensured to have a good agreement with the corresponding properties of the real material.

Failure Mechanism

In a parallel bond, relative motion at the contact causes a force and a moment to act on the two bonded particles, thus affecting the maximum normal and shear stresses at the particle bond periphery. If the maximum tensile stress exceeds the normal strength ($\sigma_{\text{max}} \geq \bar{\sigma}_c$) or the maximum shear stress exceeds the shear strength ($\tau_{\text{max}} \geq \bar{\tau}_c$), the parallel bond breaks and a

crack forms or propagates. Hence, two failure modes exist in material damage: parallel-bond normal failure and parallel-bond shear failure.

Material Inhomogeneity

Compared with normal distribution in strength, the Weibull distribution is a more reasonable distribution for ceramics (Fok et al., 2001; Lu et al., 2002). Thus, the Weibull distribution is applied to characterize the variations of the normal and shear strengths. In addition, the occasional pores among the grains in the real material can also affect the physical properties (Kawai and Yamakawa, 1997; Munz et al., 1986) such as flexural strength and fracture toughness. These pores can be mimicked by randomly deleting some particles in the DEM. Also, the surface/subsurface flaws of the workpieces induced by fabrication (Munakata and Senda, 1990) can be simulated by deleting the parallel bonds at the surface/subsurface of the specimen.

4.3.3 Calibration for the Synthetic Material

Calibration Process

Generally speaking, the synthetic material created in Section 4.3.1 does not resemble the real material, i.e., its macroproperties do not match the corresponding physical properties. Therefore, the correspondence between the synthetic and the real materials must be established through a calibration process. In the calibration process, the macroscopic responses of the synthetic material are compared directly with those of the real one. The first step is to perform numerical tests to evaluate the macroproperties of the current synthetic material. The second is to judge whether its macroproperties match the corresponding physical properties of the real material. If yes, the calibration process stops; otherwise it is necessary to create another synthetic material by adjusting the microparameters in Table 4.1 and then repeat the first step until a satisfactory material is reached. Usually several iterations are needed.

Since the behavior of silicon nitride ceramics in machining is mainly determined by the mechanical properties such as Young's modulus of elasticity, Poisson's ratio, flexural strength and fracture toughness, the corresponding numerical tests must be performed. They are described in detail in the following sections.

Numerical Compression Test (Biaxial Test)

Numerical compression test is developed so as to estimate Young's modulus of elasticity and Poisson's ratio of the synthetic material. Since the compression strength is usually much greater than the flexural strength and plays less important role in machining, it is not focused on in this study. The test environment is schematically shown in Figure 4.6a.

In the compression test, the four walls that confine the test specimen are used to load the specimen. The top and bottom walls act as loading platens, and the lateral walls are controlled by a servo-mechanism that maintains a specified confining stress. As the servo-mechanism is activated, the compression test begins, and thus confining and vertical stresses are applied to the specimen. The loading platens move towards one another at a uniform velocity V_p . The final velocity is achieved through adjusting the wall acceleration in a sequence of 10 stages over a total of 400 cycles. During the test, the deviatoric stress between the confining and vertical stress is monitored. Once the stress reaches some peak value, the specimen fails (Figure 4.6b) and the test is terminated as it drops to 0.8 times of the maximum (Figure 4.7). The parameters associated with the numerical compression test are presented in Table 4.3. The macroproperties of Young's modulus of elasticity and Poisson's ratio derived from the numerical compression test are listed in Table 4.4.

Numerical Bending Test

Numerical bending test is developed to estimate the flexural strength of the synthetic material. The ASTM standard (C1161-02c) is followed and the fixture span of configuration B is adopted. The four-point fixture test environment is schematized in Figure 4.8a. The wall in the fixture is used to mimic the loading member and the four particles act as the actual bearing cylinders. They are all frictionless. The two particles under the specimen are fixed in both the x and y directions, and the other two particles are fixed only in the x direction (ASTM, 2006a). The parameters associated with the numerical bending test are listed in Table 4.3.

A small uniform velocity is first applied to the wall. If this velocity is imposed in a single step, the inertial force due to large acceleration may damage the specimen. Thus, the velocity is achieved by adjusting the wall acceleration in a sequence of 100 stages over a total of 2000 cycles. As the wall moves downward, the load applied to the specimen gradually increases. The specimen fails as it reaches the peak force. One of the load histories in calibration process is

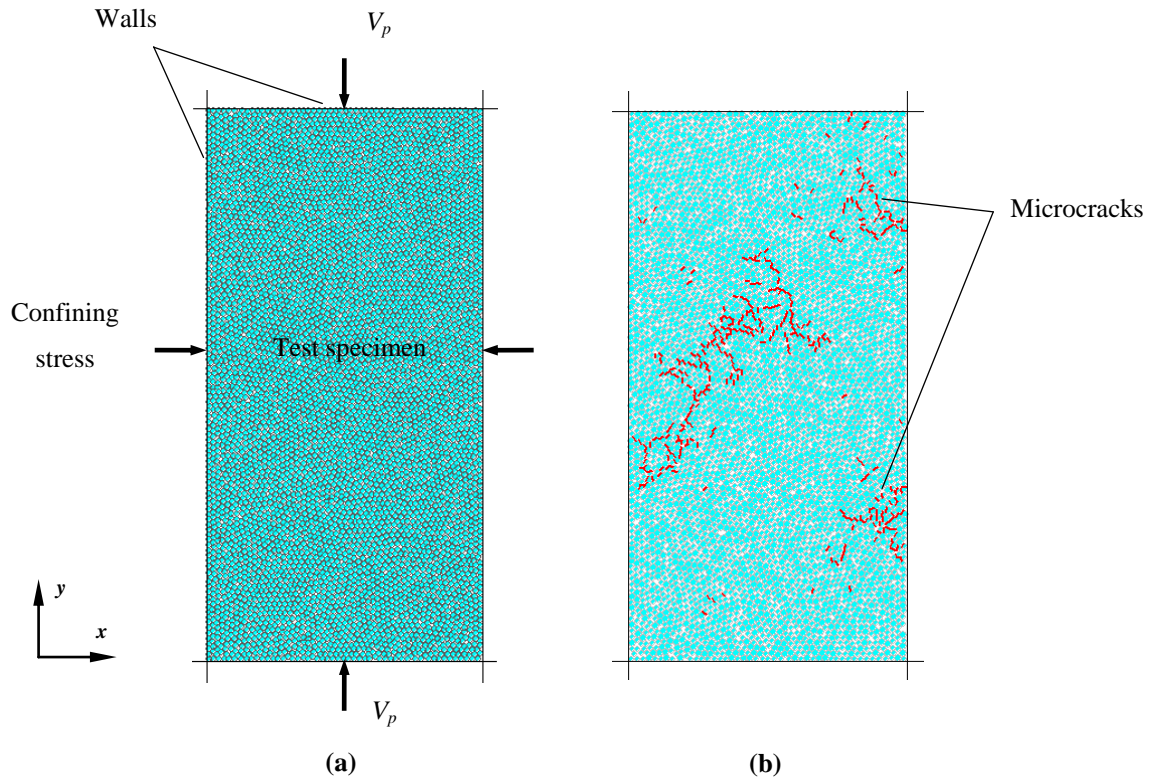


Figure 4.6 Schematic of the compression test (a) Test environment (b) Failed specimen

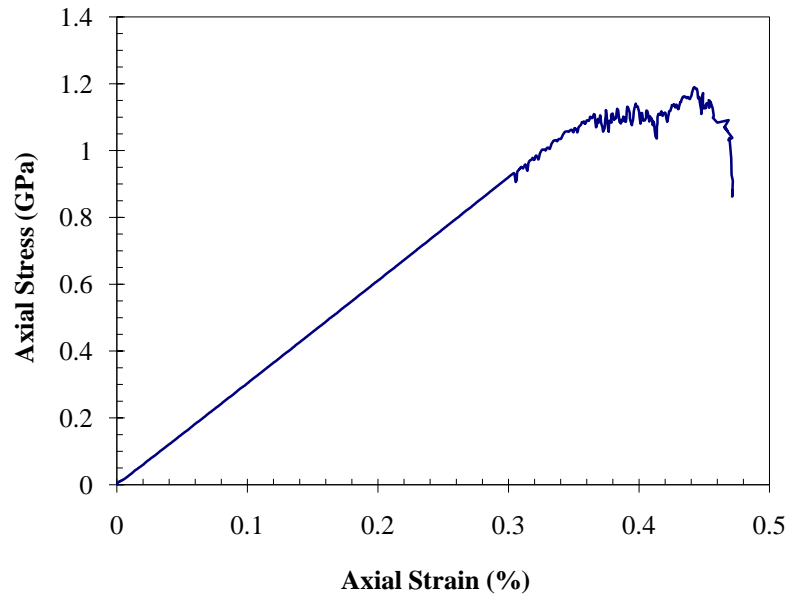


Figure 4.7 Axial stress versus axial strain in a compression test

Table 4.3 Parameters in numerical tests

Parameter	Compression Test	Bending Test	Fracture Toughness Test
Specimen length (L), mm	0.12	45	45
Specimen height (H), mm	0.24	3.0	3.0
Specimen thickness (b), mm	4.0	4.0	4.0
Loading span ($L_o/2$), mm	N/A	20	20
Support span (L_o), mm	N/A	40	40
Bearing diameter ($1.5H$), mm	N/A	4.5	4.5
Average particle radius (R_{av}), μm	1.1	7.7	7.7
Precrack length (a), mm	N/A	N/A	0.12, 0.15, 0.18
Final velocity (V_p), m/s	0.05	0.01	0.01

Table 4.4 Property comparison between real silicon nitride and synthetic material (25 °C)

Property	Real Material	Synthetic Material	Error
Elastic modulus (GPa)	310	300	3.2%
Poisson's ratio	0.27	0.264	2.2%
Flexural strength (MPa)	800	783	2.1%
Fracture toughness ($\text{MPa} \cdot \text{m}^{1/2}$)	6.0	6.1	1.7%

Note:

property data provided by Ceradyne Inc.

shown in Figure 4.9. Using the break load, the flexural strength (σ_b) can be obtained through the following equation (ASTM, 2006a):

$$\sigma_b = \frac{3PL_o}{4bH^2} \quad (4.4)$$

where P is the break force, N,

L_o is the support span, mm

b is the specimen thickness, mm

H is the specimen height, mm

Figure 4.8b shows the fracture of the failed specimen in the bending test. The specimen breaks inside the loading span. The fracture pattern is similar to that of the actual test (Tan et al., 2008b). The cracks first occur at the bottom face of the test specimen which has the maximum tensile stress and then gradually propagate upward to the top face which has the maximum compression stress. This demonstrates that the failure of silicon nitride ceramics usually takes place due to tension rather than compression. The macroproperty of flexural strength derived from the numerical bending test is listed in Table 4.4.

Numerical Fracture Toughness Test

Numerical fracture toughness test is developed to estimate the fracture toughness of the synthetic material. The four-point fixture test environment is shown in Figure 4.10a. The ASTM standard (C1421-01b) is followed and the precracked beam method is adopted (ASTM, 2006b).

The only difference between the fracture toughness and bending tests is that the specimen in the fracture toughness test has a precrack. The precrack is achieved by deleting some selected parallel bonds between particles at the region of the precrack (Shen and Lei, 2006). The precrack length (a) should be between $0.35H$ and $0.6H$. The parameters associated with the numerical fracture toughness test are presented in Table 4.3. One of the load histories in the calibration process is shown in Figure 4.11. The fracture toughness is calculated by the following equation (ASTM, 2006b; Srawley and Gross, 1976) for four-point flexure with $0.35 < a/H < 0.6$:

$$K_{Ic} = g \left[\frac{PL_o 10^{-6}}{2bH^{3/2}} \right] \left[\frac{3(a/H)^{3/2}}{2(1-a/H)^{3/2}} \right] \quad (4.5)$$

where: a is the precrack length, mm

b is the specimen thickness, mm

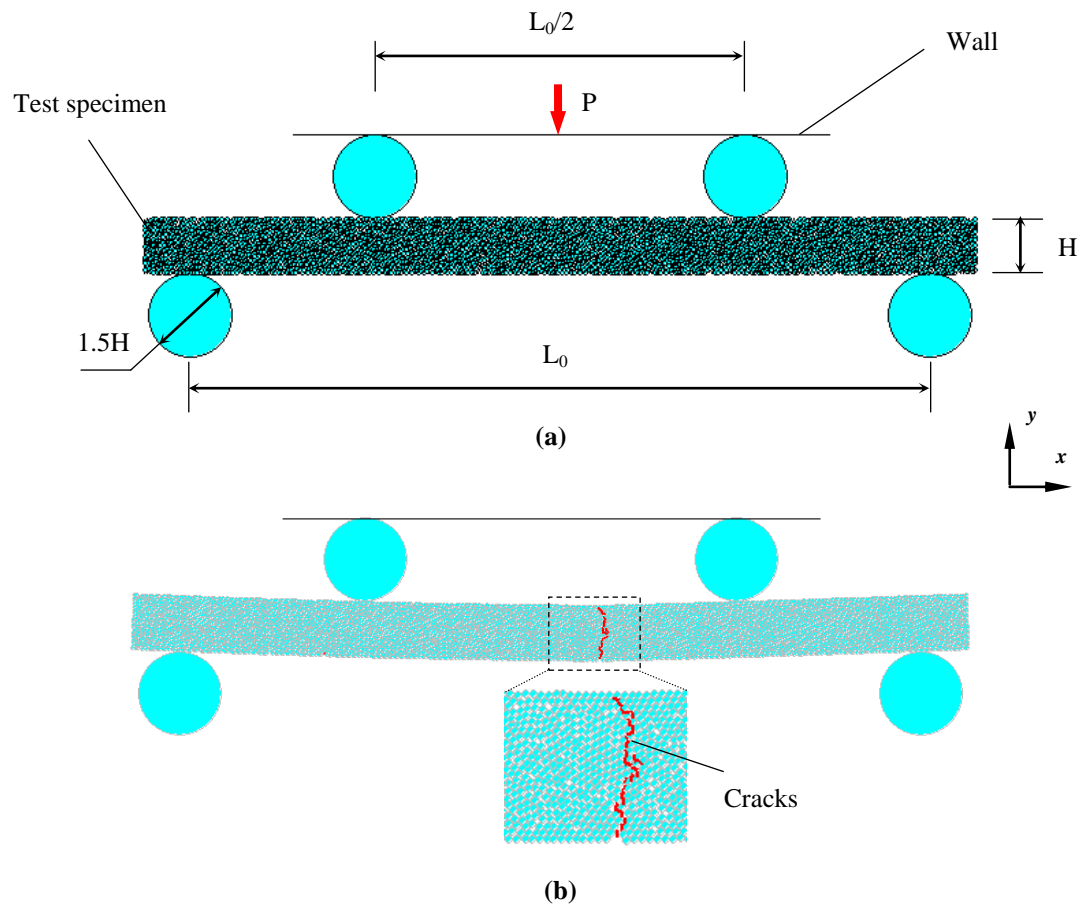


Figure 4.8 Four-point fixture schematic of the bending test

(a) Test environment (b) Failed specimen

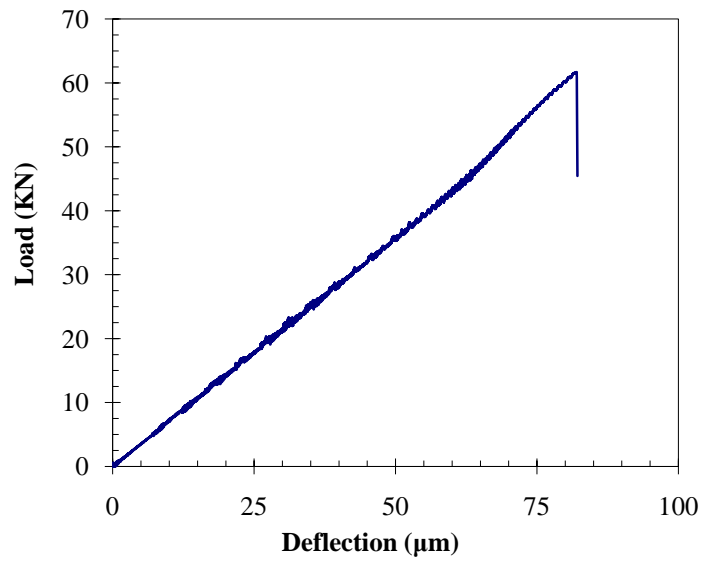


Figure 4.9 Load versus deflection in a bending test

H is the specimen height, mm

P is the break force, N

L_0 is the support span, mm

g is the function of the ratio a/H for four-point flexure, and

$$g = g(a/H) = 1.9887 - 1.326(a/H) - \frac{\{3.49 - 0.68(a/H) + 1.35(a/H)^2\}(a/H)\{1 - (a/H)\}}{\{1 + (a/H)\}^2}.$$

Figure 4.10b shows the failed specimen with fracture. The cracks propagate upward from the end of the precrack to the top face. The ratios of the crack length to the specimen height are chosen to be 0.4, 0.5 and 0.6, respectively, and the average fracture toughness is finally calculated. Note that if the real average particle radius is used, there will be so large a number of particles that the numerical test is too difficult to perform. However, the relationship between the average particle radius and the fracture toughness (Shen and Lei, 2006) suggests that an alternative larger average particle radius can be used. The relationship is expressed as: $K_{Ic} \propto \sqrt{R_{av}}$ where K_{Ic} is fracture toughness and R_{av} is the average particle radius. The macroproperty of fracture toughness derived from the numerical fracture toughness test is presented in Table 4.4.

Calibration Guidelines

To some extent, the calibration process is a trial-and-error process, in that there has been no complete theory so far that can predict the macroscopic behavior of a synthetic material from microparameters and geometry. However, the process of material creation reveals that the macroproperties of the synthetic material are strongly associated with some microparameters in Table 4.1. Young's modulus is mainly determined by particle-particle contact and parallel-bond moduli (Itasca, 2002); Poisson's ratio is related to the particle and parallel-bond stiffness ratios (Itasca, 2002); Flexural strength depends on both inter- and intra-cluster normal and shear strengths (Shen and Lei, 2009b); Fracture toughness is strongly related to inter- and intra-cluster normal strengths as well as the particle radius (Potyondy and Cundall, 2004; Shen and Lei, 2006). Note that the pores inside the workpiece and fabrication flaws at the surface/subsurface should also be considered in the calibration process. The calibration process can be guided by the following steps:

- (1) To match the Young's modulus, inter- and intra-cluster strengths are first set to a

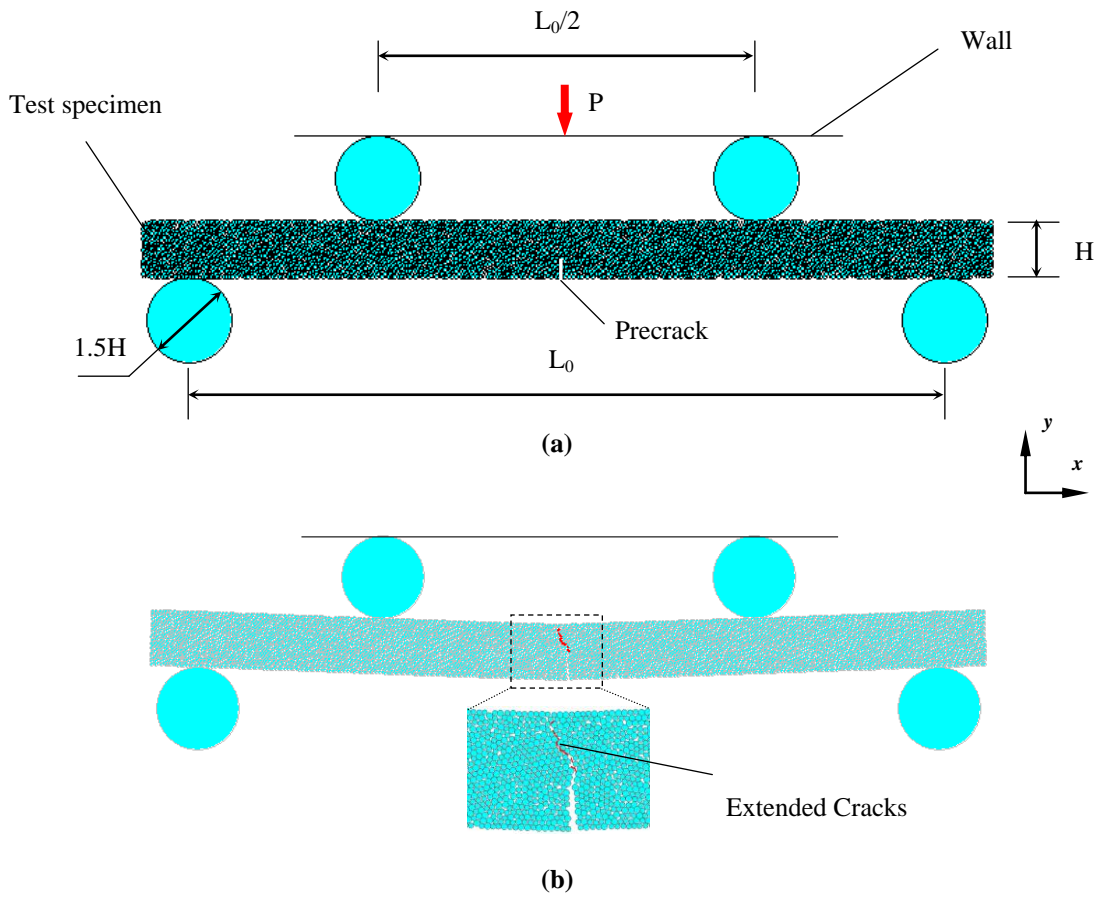


Figure 4.10 Four-point fixture schematic of fracture toughness test
(a) Test environment (b) Failed specimen

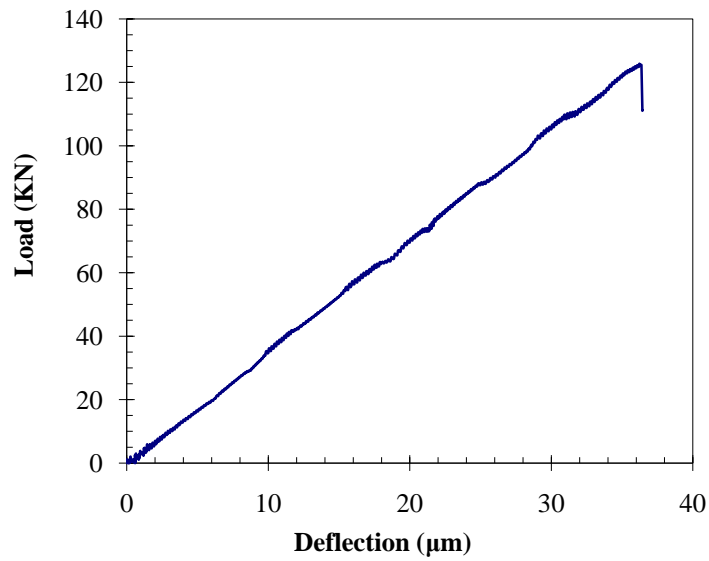


Figure 4.11 Load versus deflection in a fracture toughness test

large value and particle-particle contact and parallel-bond moduli are varied. Then, particle and parallel-bond stiffness ratios are varied so as to match the Poisson's ratio. Usually it needs a few iterations to have a good agreement. In this step, the numerical biaxial test is needed.

(2) To match the fracture toughness, first inter- and intra-cluster shear strength are set to a large value and inter- and intra-cluster normal strength are varied. In this step, the numerical fracture toughness test is needed.

(3) To match the flexural strength, the inter- and intra-cluster shear strengths are varied. Inter- and intra-cluster normal strengths are fixed. In this step, the numerical bending test is needed.

(4) To repeat Steps (2) and (3) by adjusting the inter- and intra-cluster normal and shear strengths until a good agreement is reached.

4.4 Specimen Dimensions for Material Removal

The material-creation approach presented in this study provides an effective way to reveal the deformation, damage and crack behavior under loading. For example, the numerical bending and fracture toughness tests can be used to mimic the actual expensive tests. Another important application is to simulate the dynamic process of machining such as turning, milling, drilling, ploughing, planing and so on.

In the companion paper, simulation of laser-assisted milling is conducted. The material removal, chips, surface/subsurface damages, and crack initiation, propagation and coalescence are discussed in detail. However, the specimen used in the machining simulation is usually a small part of the workpiece due to the limitation of the particle number (Figure 4.12). Hence, a reasonable specimen becomes the key issue to achieve successful simulation. There are three basic requirements as follows:

(1) To ensure the macroproperties not to be changed

The average particle size in the numerical bending or fracture toughness tests is usually different from that in material removal simulation. However, Shen and Lei (2006, 2009b) concluded that average particle size can influence both the flexural strength and fracture toughness of the specimen. Thus, the effect from the particle size cannot be neglected in the synthetic material creation. In addition, Yang et al. (2006) found that as the ratio between the specimen length and the average particle radius (L/R_{av}) is larger than 90, the Poisson's ratio

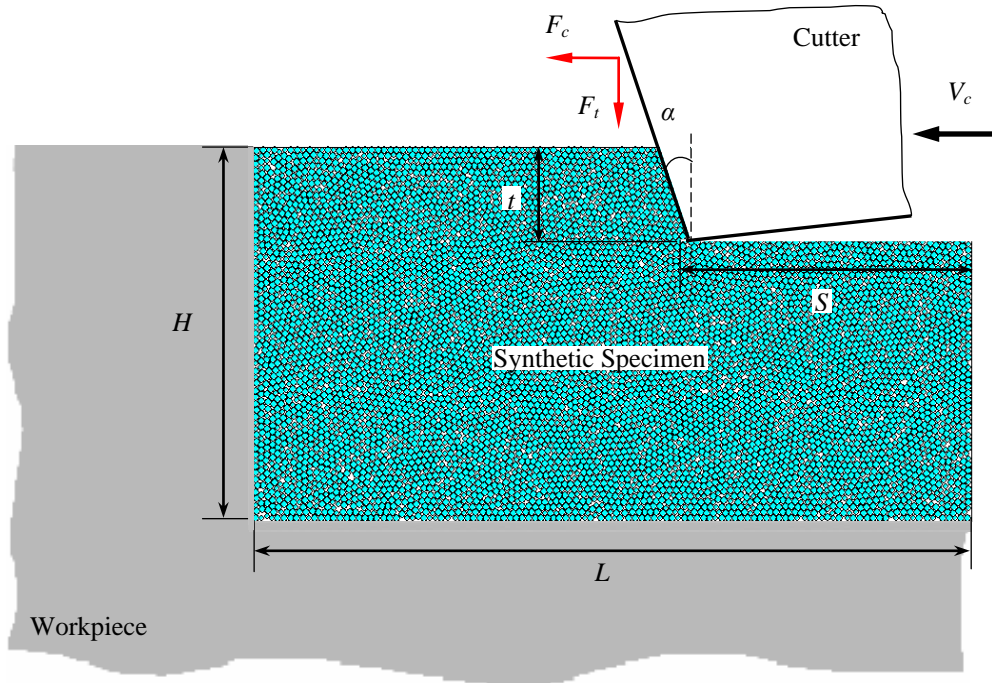


Figure 4.12 Schematic of material removal configuration

appears to be independent of particle size, and when the ratio is larger than 130 the Young's modulus varies little for different particle sizes.

(2) To avoid the boundary effect

Both the experiments and the simulations (Shen and Lei, 2005; Shen and Lei, 2009a) show that the material removal of silicon nitride ceramics is mainly realized by brittle fractures. Cracks first develop near the tool tip and then propagate forward to form the lateral cracks and downward to form median cracks. Hence, the ratios of specimen length to the average radius (L/R_{av}) and the specimen height to the average radius (H/R_{av}) should be large enough so as to avoid cracks reaching the left and bottom boundaries.

(3) To have enough microevents for repeatability

The ratios of cutting length to the average radius (S/R_{av}) and the uncut chip thickness to the average particle radius (t/R_{av}) should also be large enough so as to allow more particles to engage in material removal, thus capturing more microevents.

4.5 Conclusions

The DEM is one effective approach to model the microstructures of brittle materials with granular nature. In the microstructural modeling of the β -Si₃N₄, clusters and parallel bond are used to mimic the real grain shapes and the intergranular glass phase between grains, respectively. For a successful creation of a synthetic material, the calibration process is definitely needed. The macroproperties of the synthetic material must match the corresponding physical properties of the real one, which is done through conducting numerical testing (compression, bending, and fracture toughness test) on the synthetic material. Several guidelines are given to assure an efficient calibration process. For a reasonable synthetic specimen prepared for material removal, its dimensions, uncut thickness and cutting length should be selected carefully, thus avoiding the boundary effect and obtaining more microevents. However, there is still some work to do in the next step, which should mainly focus on obtaining more information on the microstructure of the real material so as to improve the accuracy of the model.

Chapter 4 - Machining Modeling and Experimental Investigation of Laser-Assisted Machining of Silicon Nitride Ceramics *

In laser-assisted machining (LAM), laser heating causes the variations of the material properties. Therefore, temperature-dependent materials used for LAM will be created in this Chapter. Also, the three-dimensional (3D) milling with a curved cutting edge will be converted to the two-dimensional (2D) orthogonal cutting with a straight cutting edge, because this study uses a 2D distinct element code, PFC^{2D}. The machining model is validated through comparing the predicted results with the experimental ones in terms of cutting forces, chip size, and depth of subsurface damage. In addition, the mechanisms of LAM are analyzed in detail from the aspects of material removal, chips, surface/subsurface damages, as well as crack initiation, propagation and coalescence.

5.1 Introduction

Laser-assisted machining (LAM) of advanced structural ceramics has been studied for about two decades. König and Zaboklicki (1993) first used laser-assisted turning to machine silicon nitride ceramics, and demonstrated the feasibility of LAM for advanced ceramics. Rozzi et al. (1998) successfully used a numerical model to predict the temperature distribution of a ceramic workpiece in LAM and established a scientific basis from the thermal aspects. Lei et al. (2001), Rebro et al. (2004) and Pfefferkorn et al. (2005) successively conducted experimental assessment of LAM, and showed the ability to machine various ceramics. Tian and Shin (2006) studied complex feature machining of ceramics and thus extended the capability of LAM. In addition, some other types of operations of LAM were investigated as well, including Westkäemper (1995) and Marinescu (1998) on laser-assisted grinding of silicon nitride, Chang and Kuo (2007) on laser-assisted planing of Al₂O₃, Yang et al. (2007) and Tian et al. (2008) on laser-assisted milling (LAMill) of silicon nitride.

The contents of this Chapter are from my following journal paper:

* **Shen, Xinwei**, Yang, Budong, and Lei, Shuting (2009). Numerical modeling and simulation of laser-assisted machining of silicon nitride ceramics with distinct element method: part II, simulation of the dynamic cutting process. *Journal of Manufacturing Science and Engineering, Transactions of the ASME*, (under review)

However, there is very little literature concerning the mechanisms of LAM of ceramics through numerical models. The reason is that machining of brittle materials exhibits very complicated characteristics such as crack formation and propagation, discontinuous chips and so on, which increases the difficulty of model development by using the continuum model (e.g. FEA model). But it should be noted that some FEA models still achieved various degrees of success in simulating brittle materials machining.

Combining the theories of contact and fracture mechanics, Zhang and Cao (2000) developed a FEA model to simulate the material removal process of glass ceramics. The subsurface microcracks were assessed and the surface integrity was evaluated. Kumbera et al. (2001) and Ajjarapu et al. (2004) used two-dimensional FEA models to conduct orthogonal cutting of silicon nitride. The models considered power-law strain-hardening, thermal softening, rate sensitivity and adaptive remeshing technique; moreover, it was assumed that silicon nitride ceramics behave in a ductile fashion under high pressures and very small depth of cut. Liu and Zhang (2002) incorporated continuum damage mechanics (CDM) with finite element analysis to predict lateral damage induced by grinding. Recently, in order to simulate the chip formation in laser-assisted turning of silicon nitride ceramics, Tian and Shin (2007) presented a multiscale FEA model and used hexagonal cells to contain several silicon nitride grains. In addition, some analytical models were developed to predict machining flaw size (Marshall et al., 1983), chip thickness (Subramanian et al., 1997) and cutting forces (Liang and Devereux, 1993). Also, some molecular dynamics (MD) models were applied to investigate the material removal mechanism and surface generation process (Komanduri and Raff, 2001).

Nevertheless, one weakness of FEA models is the lack of consideration of material microstructures at grain scale, which, as well recognized, dominate the thermal-mechanical dynamic behaviors of brittle materials (Rühle, 1985; Lee and Rainforth, 1994). The analytical models cannot describe the complicated machining process, and molecular dynamics (MD) models are usually used for ultraprecision and nanometric machining. Hence, effective modeling and simulation methods in brittle machining are strongly needed. Currently, the distinct element method (or discrete element method, DEM) seems to be a promising approach, which treats a material as an assembly with densely packed and arbitrarily sized circular particles bonded together. When the bonds break, cracks form or propagate. In contrast with continuum models (e.g. FEA model), the DEM can describe non-linear behavior and localization with accuracy and

treat the material inhomogeneity as well. Moreover, it can handle the complex particle contact physical processes with coupled shear and bulk deformation effects.

The DEM was first introduced by Cundall for the analysis of rock-mechanics (Cundall, 1971). In recent years, it has been applied to the material removal simulation. Huang (1999) used the DEM to conduct rock cutting and found that the transition of failure modes is related to the depth of cut. Kaitkay and Lei (2005) developed a DEM model to simulate rock cutting under different hydrostatic pressures and achieved a good agreement with the experiments. Ledgerwood (2007) also used DEM for rock cutting under different hydrostatic pressures and pointed out that rock drillability is more largely affected by inelastic properties than elastic ones. Lei and Yang (2005) applied the DEM to ceramic machining and indicated that both the median and lateral cracks are very similar to the cracks observed in the experiments. Later on, Shen and Lei (2005) extended it to LAM of ceramics and concluded that all the parameters, such as workpiece temperature, rake angle, depth of cut, damping coefficient and cluster size, affect the crack formation and surface/subsurface damages. Tan et al. (2008) used the DEM to investigate the crack length and depth in scratching of Al_2O_3 ceramics. They found that both the maximum surface crack length and subsurface crack depth increase as the scratching depth increases.

Built on our previous work (Shen and Lei, 2005, Shen and Lei, 2009b), the purpose of this paper is to develop and validate a grain-scale DEM machining model for a silicon nitride ceramic. The model helps to reveal the machining mechanisms of LAM at different operating temperatures, especially in terms of material removal, chip formation, surface/subsurface damages, and crack initiation, propagation and coalescence. In the following sections, a temperature-dependent synthetic silicon nitride material is first created according to the approach presented in the companion paper (Shen and Lei, 2009a). Then, an equivalent orthogonal cutting configuration is established to relate simulation to the three-dimensional (3D) milling experiments. Next, the laser-assisted milling (LAMill) experiments are described. Finally, the model is validated with detailed comparison and discussions of the experimental results and model predictions.

5.2 Temperature-Dependent Synthetic Material

In this section, the two-dimensional (2D) distinct element code, PFC^{2D}, is used to create three temperature-dependent synthetic specimens for laser-assisted milling. The material used in

this study is a sintered reaction bonded silicon nitride (β -Si₃N₄) with 8wt% additives (Ceradyne Inc.). Some properties are listed in Table 5.1

5.2.1 Temperatures over the Cutting Zone

As is known, silicon nitride is a temperature-dependent material (Hampshire, 1991). Laser local heating can cause its thermophysical properties to change with temperature (Table 5.1). Hence, the temperatures of the workpiece especially over the cutting zone must be known before simulation.

In this study, the temperatures of the workpiece are obtained through a transient 3D thermal FEA model which was verified through a series of laser-assisted milling (LAMill) experiments in our previous work (Shen and Lei, 2009c). Figure 5.1 illustrates the temperature distribution under the following operating conditions: laser power (P_l) of 410 W, preheat time (t_p) of 12 s, cutting speed (V_c) of 1.0 m/s, feed (f) of 0.024 mm/tooth/rev, feed rate (V_f) of 6 mm/min and depth of cut (DOC) of 0.2 mm.

In Figure 3.6, the MN and MX symbols identify the locations of the minimum and maximum temperatures (the left face of the workpiece and the laser spot center), respectively.

Table 5.1 Properties of Si₃N₄

Parameter	Temperature (°C)			
	25	1080	1260	1350
Density (kg/m ³)	3200			
Flexural Strength (MPa)	800	750	540	420
Elastic Modulus (GPa)	310	297	294	291
Poisson Ratio	0.27	0.26	0.255	0.251
Fracture Toughness (MPa · m ^{1/2})	6.0	5.3*	6.6*	6.2*
Specific Heat (J/kg · K)	680.4	1080	1135	1160
Thermal Conductivity (W/m · K)	26	18	17	16

Note: * Obtained from interpolation from Mutoh et al. (1992) and property data from Ceradyne Inc.

The contour interval is uniform and defined as the difference between two adjacent contour lines. The region near the laser spot has higher temperatures (over 1000°C) than the surroundings. The approaching portion of the laser spot continuously absorbs energy from heat conduction and as a result, temperatures increase quickly, while the newly uncovered region is gradually cooling down due to free convection and thermal radiation. The contour intervals in the x , y and z directions are not uniform and instead tend to increase from the laser spot to the surrounding portion. That is, along the x , y and z directions, the thermal gradients are becoming smaller. The temperature distribution reveals that the laser heat source has strong influence on the region around the laser spot and weak influence on the region beyond. Section A-A is made as shown in Figure 3.6, which passes through the cutting zone at the top face of the workpiece.

5.2.2 Synthetic Specimen for LAM

Figures 5.1a,b,c show the configuration of laser-assisted milling, the cutting zone (uncut chip) and temperatures over the cutting zone from simulation (Shen and Lei, 2009c), respectively. The workpiece dimensions are $4.3_x \times 5.6_y \times 48_z$ mm. If the specimen in simulation is selected to have the same size of the workpiece, a very large number of particles (roughly 1.3×10^6) are required, which, however, is computationally prohibitive in our current situation. Hence, a small one with dimensions of $0.56_x \times 0.4_y \times 0.13_z$ mm is adopted.

In addition, for convenience the temperatures over the specimen in simulation are simplified as well. Figure 3.6 shows that the temperatures in the x direction are not uniform. It is unlikely to use the specimen with the short length of 0.56 mm to reflect the temperature variations of the workpiece with the width of 4.3 mm. However, in considering the temperature differences in this direction are within 42°C (Shen and Lei, 2009c), the average temperature is acceptable for the specimen. Similarly, the temperatures in the y direction are also selected as an average value because of the 2D distinct element code and the temperature differences within 55°C. In the z direction, as illustrated in Figure 5.1b, the feed (f) of 0.024 mm/rev/tooth is much smaller than both the workpiece width (W_w) of 4.3 mm (in the x direction) and the depth of cut (DOC) of 0.2 mm (in the y direction), so the temperature variations over the cutting zone in the z direction can be neglected. Furthermore, the temperature of the specimen in the z direction can also be regarded as uniform, since, in LAMill, the temperatures over the cutting zone are maintained almost the same in each cut.

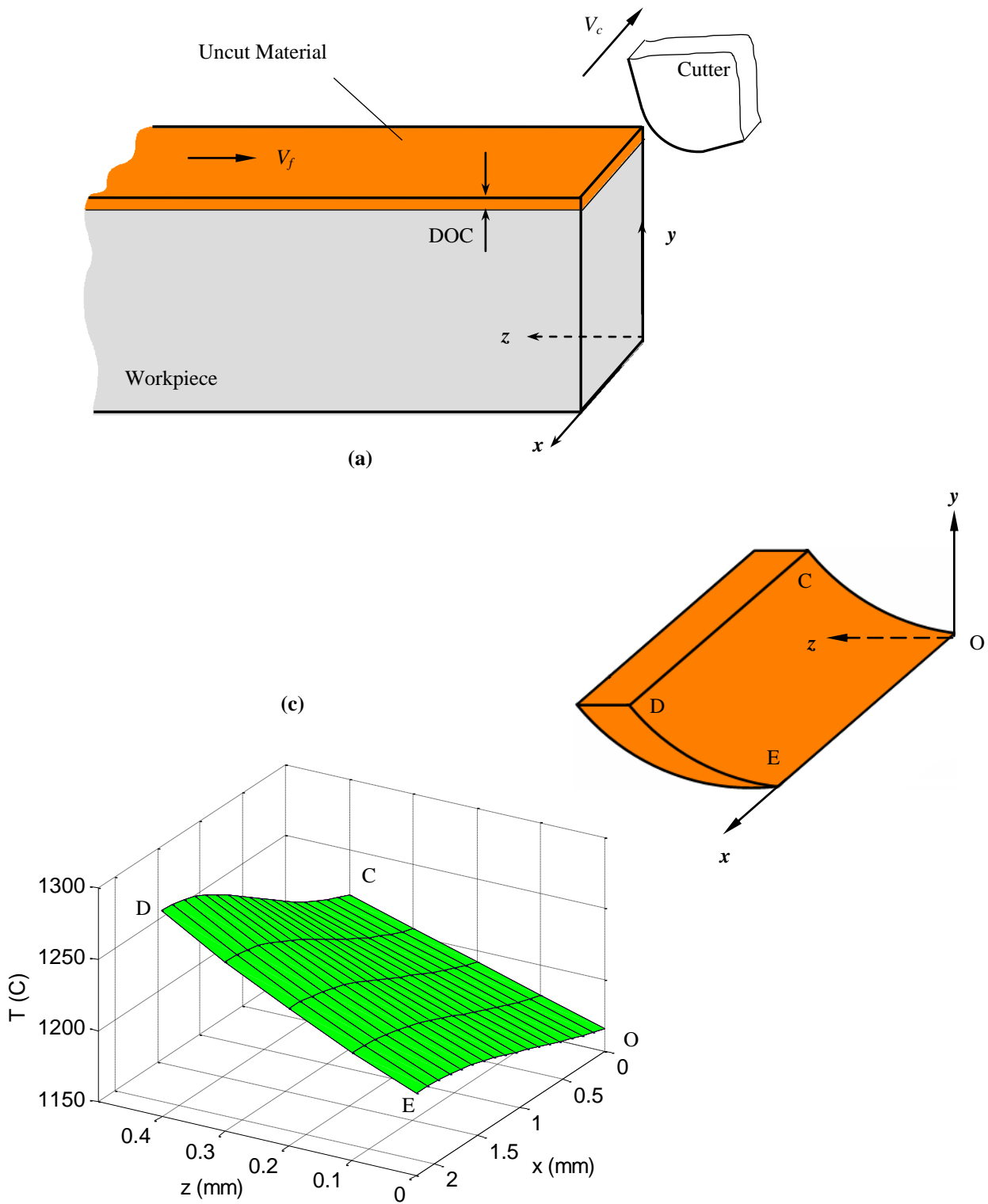


Figure 5.1 Schematics of laser-assisted milling

(a) Configuration (b) Cutting zone (uncut chip) (c) Temperatures over the cutting zone from simulation ($P_l = 410$ W, $V_c = 1.0$ m/s, $f = 0.024$ mm/tooth/rev, $V_f = 6$ mm/min, and $t_p = 12$ s, $L_c = 7.0$ mm)

5.2.3 Creation of Temperature-Dependent Synthetic Specimen

The small specimen mentioned above can be created following the approach presented in the companion paper (Shen and Lei, 2009a). Through the numerical compression, bending and fracture toughness tests, the responses of the specimen are made to match the corresponding thermophysical properties at a certain temperature. This temperature-dependent synthetic specimen will be used in simulation of LAMill. In this study, the specimens at the temperatures of 1080°C, 1260°C and 1350°C are created containing 16,087 particles, respectively. As an example, some key parameters are provided in Table 5.2 and the ultimate microparameters for the case of 1350°C are listed in Table 5.3.

5.3 Equivalent Orthogonal Cutting

In order to conduct simulations of the 3D milling process using the two-dimensional (2D) distinct element code, PFC^{2D}, the curved cutting edge in the 3D milling (Figure 5.2a) should be converted into the straight cutting edge in orthogonal cutting (Figure 5.2b). Through the equations presented by Young et al. (1994) and Arsecularatne et al. (1995), the rake angle (α) and side cutting edge angle (C_s) of the cutter with an equivalent cutting edge are estimated. The equivalent uncut chip thickness ($t_{u,e}$) and width of cut (b) are approximated using the following equations (Young et al., 1994):

$$t_{u,e} = f \cos(C_s) \quad (5.1)$$

$$b = DOC / \cos(C_s) \quad (5.2)$$

where $t_{u,e}$ is equivalent uncut chip thickness, mm

b is equivalent width of cut, mm

f is feed, mm

C_s is side cutting edge angle, deg

DOC is depth of cut, mm

Note that the cutting edge only includes a part of the round nose ($DOC \leq r(1 - \sin(C_s))$) and does not extend to the straight side of the cutting edge.

Since the cutter nose radius (r) of 0.787 mm used in this study is much larger than the depth of cut (DOC) of 0.2 mm, there is only one part of its nose contacting the workpiece in milling. Moreover, the cutter diameter (D_c) of 76.2 mm is considerably larger than the workpiece

Table 5.2 Parameters that control the material-creation procedure

Parameter	Value
Specimen height, H (mm)	0.13
Specimen length, L (mm)	0.6
Specimen thickness, b (mm)	0.4
Average particle radius, R_{av} (μm)	1.1
Particle size ratio, R_{max}/R_{min}	1.2
Cluster size, N_c	5

Table 5.3 Microparameters that define the DEM material (1350°C)

Parameter	Value
Particle density, ρ (kg/m^3)	3200
Particle-particle contact modulus, E_c (GPa)	243
Parallel-bond modulus, \bar{E}_c (GPa)	
Particle stiffness ratio, k_n/k_s	2.65
Parallel-bond stiffness ratio, \bar{k}^n/\bar{k}^s	
Particle friction coefficient, μ	0.4
Parallel-bond normal inter-cluster strength, mean, $\bar{\sigma}_{c,mean}$ (GPa)	1
Parallel-bond shear inter-cluster strength, mean, $\bar{\tau}_{c,mean}$ (GPa)	0.55
Parallel-bond normal intra-cluster strength, mean, $\bar{\sigma}'_{c,mean}$ (GPa)	5
Parallel-bond shear intra-cluster strength, mean, $\bar{\tau}'_{c,mean}$ (GPa)	2.75

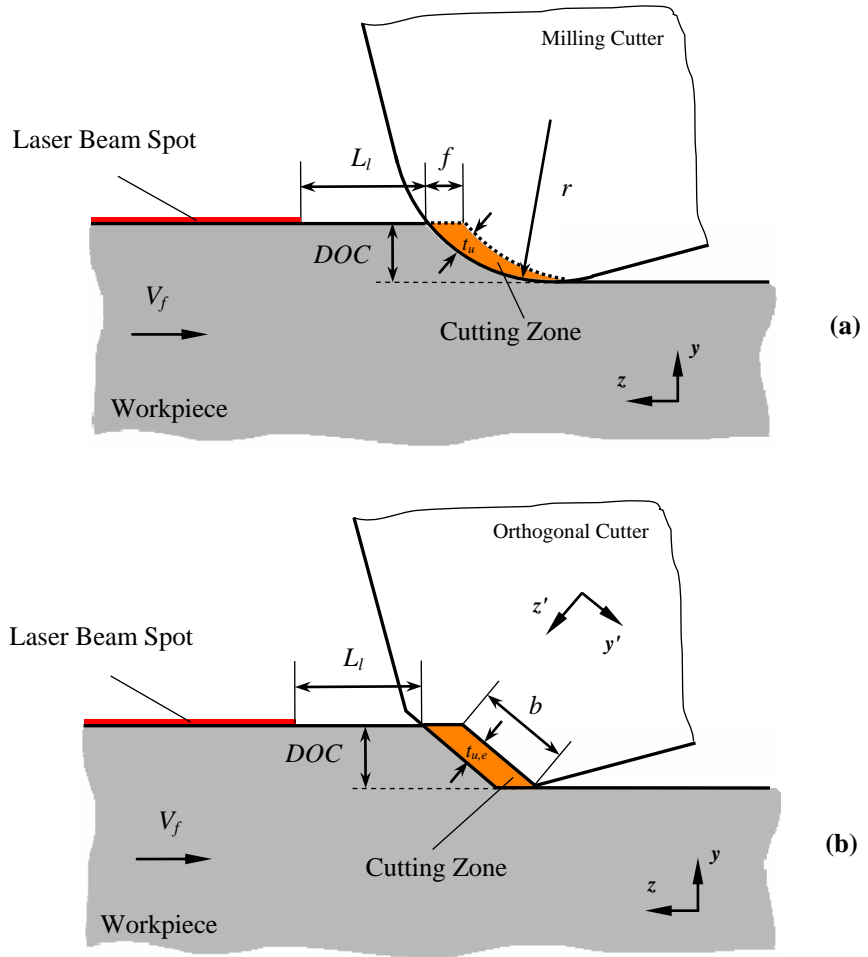


Figure 5.2 Schematics of laser-assisted milling (a) Actual milling (b) Equivalent orthogonal cutting

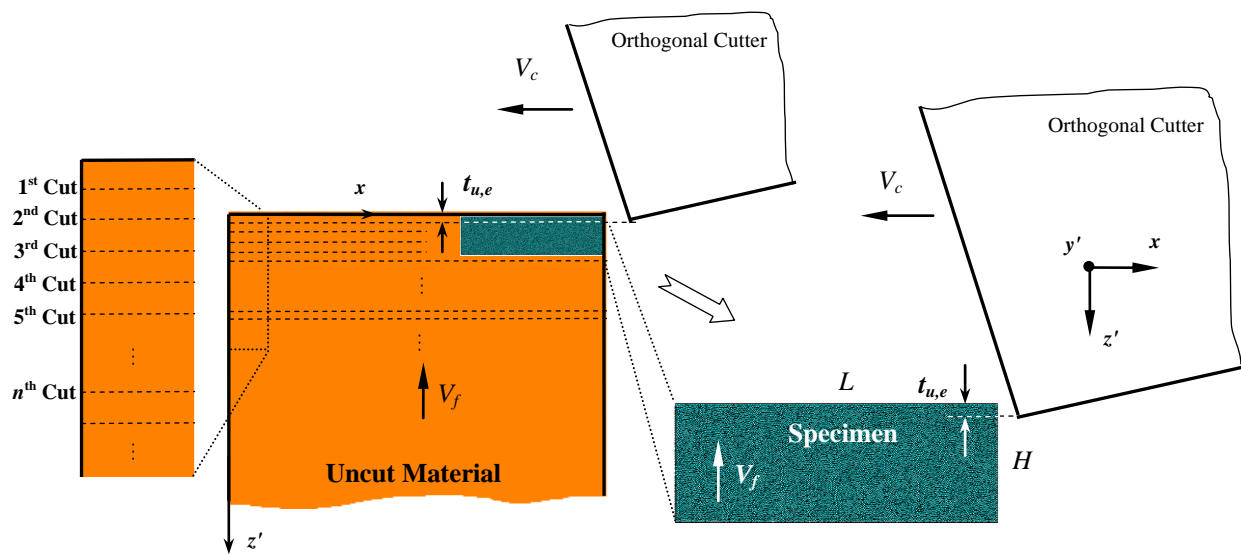


Figure 5.3 Orthogonal cutting in simulation

width (W_w) of 4.3 mm. Thus, the cutting path on the workpiece can be approximated to be a straight line. The cross section of the uncut chip (called cutting zone in this study) in any y - z plane is shown as Figure 5.2a. Note that the cutter motion is in the x direction (out-of-plane).

Thus, the orthogonal cutting in simulation can be schematized in Figure 5.3.

5.4 Experimental Setup of LAMill

In order to validate the DEM model, LAMill experiments are conducted. The experimental setup is illustrated in Figure 2.1. The milling operation is carried out on a CNC machine (Haas Automation Inc.). A diode laser (Visotek Inc., DFL500) with a top hat power distribution is used to generate a high power laser beam, which is delivered through the optical fiber and strikes on the workpiece surface at the angle of about 70 deg. The air jet is employed to cool and prevent the optics from being overheated. An infrared pyrometer (Williamson Inc., Model 91-20-C-23D) with a range of 475-1750°C is used to concurrently measure the surface temperature of the workpiece. The dynamometer (Kistler Inc., Type 9257B) is fixed on the worktable and utilized with a charge amplifier (Kistler Inc., Type 5010) to measure the cutting forces in the global x , y , and z directions. Both the pyrometer and the laser optics are installed through holders on the spindle. The workpiece is clamped with a vise mounted on the dynamometer. Between the workpiece and vise, insulating materials are used to prevent heat loss. Both the measurement results from the pyrometer and the dynamometer are digitally recorded in a computer.

In addition, dozens of our experiments demonstrated that there is severe tool wear in LAMill of silicon nitride with commercial carbide inserts; therefore, a house-made milling cutter is made which has a single tooth with a solid PCBN insert (SNM322, J&M diamond Tool, Inc). The insert is clamped on a tool holder (Kennametal, Model CSRNR083 NA4), and the tool holder is fixed in a steel shaft. The purpose of this special design is to simplify the machining process and thus facilitate analysis, because it always assures that only one tooth contacts the workpiece in the cutting operation. The parameters of the nose cutter used in this study include: rake angle (α) of -5 deg, clearance angle (β_c) of 5 deg, inclination angle (i) of 0 deg, side cutting edge angle (C_s) of 15 deg, chamfer angle (θ_c) of 20 deg and chamfer width (W_c) of 0.1 mm.

5.5 Model Validation

The operating conditions of LAMill experiments are shown in Table 5.4. The feed rate (V_f), feed (f), cutting speed (V_c) and depth of cut (DOC) are fixed. The cutting temperature (T_c) is the only variable with values of 1080°C ($P_l = 300$ W, $t_p = 15$), 1260°C ($P_l = 410$ W, $t_p = 12$ s) and 1350°C ($P_l = 470$ W, $t_p = 8$ s). The equivalent uncut chip thickness (t), width of cut (b) and rake angle (α_e) are taken to be 0.012 mm, 0.4 mm and -4.84 deg, respectively.

Table 5.4 Operating conditions of laser-assisted milling of Si₃N₄

Temperature (°C)	Feed (mm/tooth/rev)	Feed rate (mm/min)	Cutting Speed (m/s)	Depth of Cut (mm)
1080	0.024	6	1.0	0.3
1260				
1350				

Figure 5.4 shows the configuration of the equivalent orthogonal cutting. In order to better display the relationship between the specimen, the cutter, the cracks and the chips, the first cut of the machining process is shown. Due to the specialty of the first cut (cut on fresh material), the following cuts are focused on in the analysis of cutting forces, chips and the depth of subsurface damage (d). Note that the ideal rigid cutter (without wear flat) is modeled with a standard wall consisting of five line segments.

The mechanisms of the dynamic machining process can be evaluated from the following aspects:

Material Removal

Once the cutter touches the workpiece, the cutting force dominates the material deformation and removal, which can be described through simulation. As the cutter contacts the particle assembly, the resulting force and moment rise quickly. They are transmitted by the parallel bonds to the surrounding particles. As a result, the normal and shear stresses acting within the bond material increase immediately. When the stress exceeds the corresponding bond strength, the parallel bonds begin to break and the cutting forces decrease quickly. As shown in Figure 5.5, the compressive forces are found inside the specimen. The maximum compressive force

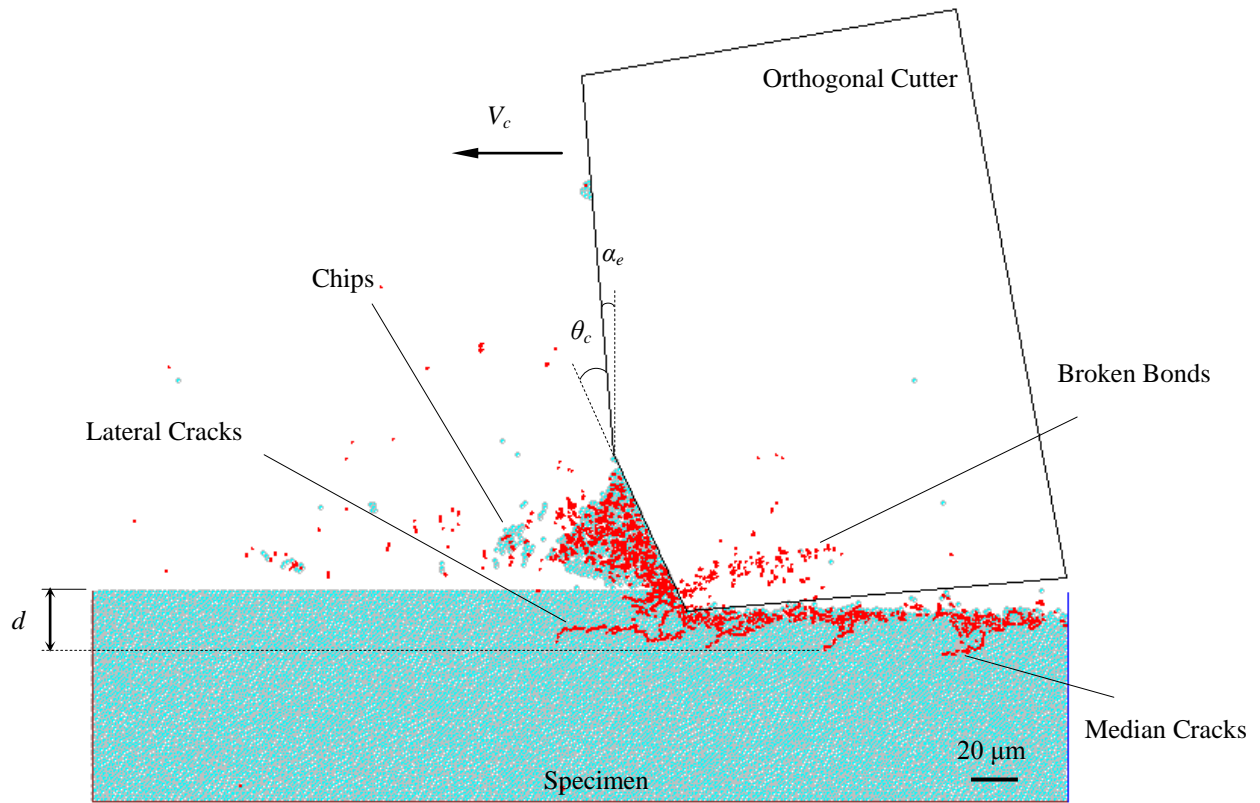


Figure 5.4 Configuration of the orthogonal cutting

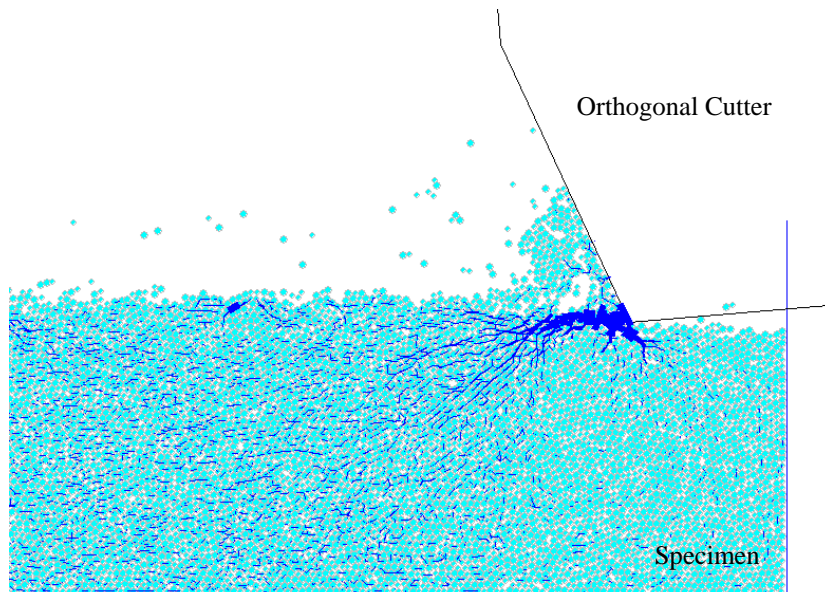


Figure 5.5 Contact-force distribution from simulation (Note: the thickness represents the magnitude)
 ($T_c = 1350^\circ\text{C}$, $DOC = 0.2\ \text{mm}$, $V_c = 1\ \text{m/s}$, $f = 0.024\ \text{mm/rev/tooth}$)

occurs at the region near the tool tip, usually called primary crushing region. Thus, cracks first develop around the tool tip and then run forward to form the lateral cracks and propagate downward to form median cracks. With the cutter moving, the contact forces redistribute. The localized bond breakage also induces global stress redistribution. The continuous bond breakage near the tool tip and coalescence of cracks eventually cause some particles to escape from the assembly, thus forming the chips. With the cutter moving forward, these chips accumulate and pile up along the cutter face and are carried away by the cutter. Meanwhile, a damage layer with some loosely attached particles is left on the scratched surface, which can be observed in the freshly machined surfaces of the workpiece.

It should be mentioned that with the cutter contacting the workpiece in LAMill, the deformation induced by the creep also occurs inside the silicon nitride material. High temperature due to laser local heating leads to the amorphous intergranular glass phase to redistribute via viscous flow process. After the viscous flow process exhausts, the new deformation process, cavity formation at the multigrain junctions or solution-precipitation, takes over, which depends on whether the creep is in tension or in compression (Chadwick et al., 1993; Wiederhorn, 1999). However, in the process dominated by machining, the deformation from the creep is neglected in this study.

Cutting Forces

The history of the cutting forces in Figure 5.6 clearly shows the highly dynamic nature of the cutting process from the “microscopic” aspect within the cutting length of 0.3 mm, which is too difficult to capture in the actual machining because all the events happen in only 0.3 ms. From this “microscopic” process, it can be seen that, along with the crack formation, propagation and coalescence, the cutting forces (main and thrust forces) show fluctuations. It can be imagined that the force exerted by the cutter initially turns into elastic energy at the cutting zone, and as the load exceeds the fracture strength of the material, this energy is then released to a large extent as kinetic energy of the ejected chips. The built-up and sudden release of the cutting energy is manifested through the steep variations of the cutting forces. Also, it can be seen that crack formation and propagation is strongly related to the cutting forces. A long crack usually has a corresponding couple of peak forces (main and thrust forces). It is suggested that cutting force can roughly reflect the variations of the surface/subsurface cracks. This can partly explain why

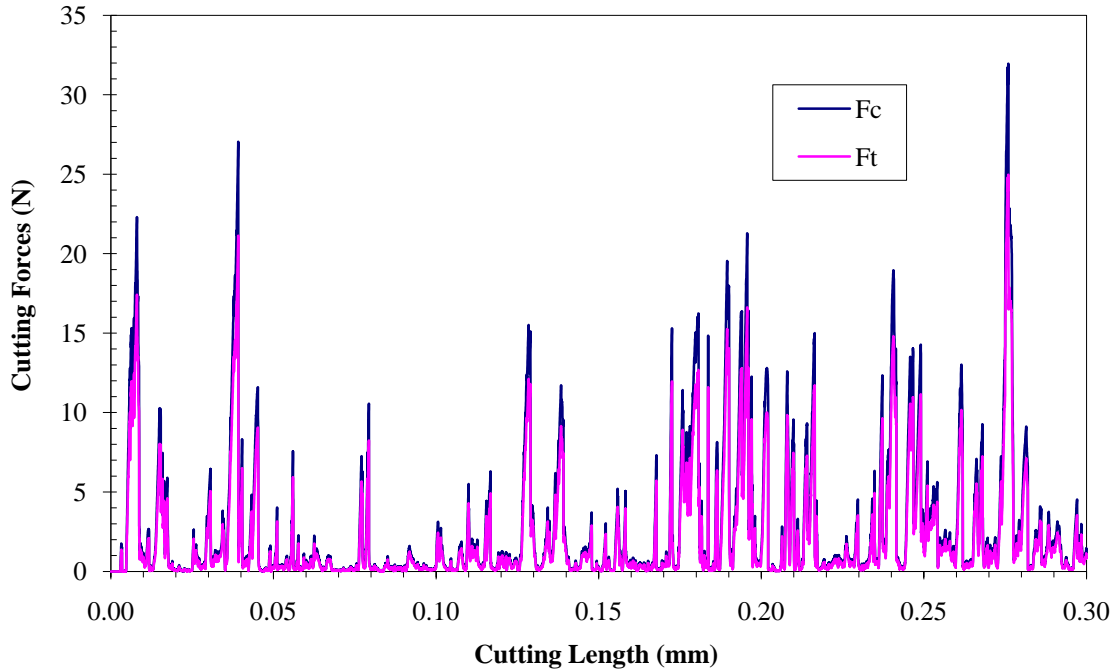


Figure 5.6 Histories of the cutting forces from simulation
 ($T_c = 1350^\circ\text{C}$, $DOC = 0.2$ mm, $V_c = 1$ m/s, $f = 0.024$ mm/rev/tooth)

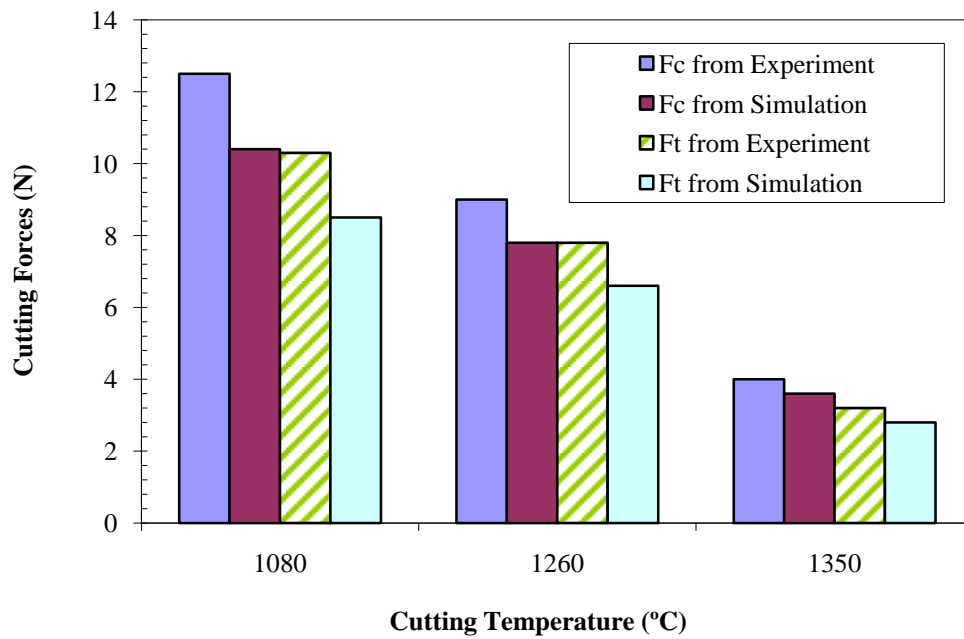


Figure 5.7 Comparison of the experimental and simulated cutting forces under different cutting temperatures

small cutting force is commonly desired in machining. Certainly, cutting force is the most important parameter in evaluating the cutting dynamic process.

Consequently, in this study the average cutting forces are chosen for a quantitative comparison between experiments and predictions. To compute the cutting forces with different depths of cut from experiments, the cutting forces F_z and F_y , are first converted to the main force (F_c) and thrust force (F_t) and then the average main and thrust forces are obtained, respectively.

Figure 5.7 shows a comparison of the cutting forces at the temperatures of 1080°C, 1260°C and 1350°C. As expected, both the predicted and the experimental forces decrease as the cutting temperature increases. However, it is found that the cutting forces at 1260°C has a sudden increase following the trend from 1080°C to 1350°C, although the temperature difference between 1080°C and 1260°C is still larger than that between 1260°C and 1350°C. This can be explained by the fact that, 1260°C falls within the temperature range of brittle-to-ductile transition (1200-1275°C). Mutoh et al. (1992) revealed that as the temperature rises to the softening point of the glass phase (about 1200°C), the intergranular glass phase becomes adequately soft and the brittle-to-ductile transition of fracture occurs. The resistance to brittle fracture causes a rapid increase of the fracture toughness and, thus slowing down the decrease of the cutting force. Thus, it is strongly recommended to avoid the brittle-to-ductile transition in LAMill.

From Figure 5.7, it can also be found that the predicted results consistently underestimate about 10%-17% of the cutting forces in the experiments. Besides the various possible reasons such as the 2D nature of the model, the simplified temperature distribution for the specimen and the material removal induced by laser heating, it is believed that tool wear and exit edge chipping are the main reasons which are not considered in the current simulations. To this end, the initial cutting length (L_c) of 2 mm in the experiments is considered in the comparison of the cutting forces in this study.

Figure 5.8 clearly shows that the tool wear decreases largely when the cutting temperature rises.

It can be observed from Figure 5.9 that exit edge chipping varies with the cutting temperature. Edge chipping is a sudden macroscale or microscale edge damage and arises from the sudden release of the energy built in the machining process. Exit edge chipping occurs when the cutter is leaving the workpiece. Yang et al. (2009b) concluded that edge chipping can affect

the cutting force. A more edge chipping causes a large cutting force, because of the extra portion of the material being removed besides the portion at the cutting zone.

In addition, Figure 5.7 also shows that with the cutting temperature increasing, the ratio between the predicted and the experimental forces increases. This is mostly attributed to the decrease of both tool wear and exit edge chipping with temperature.

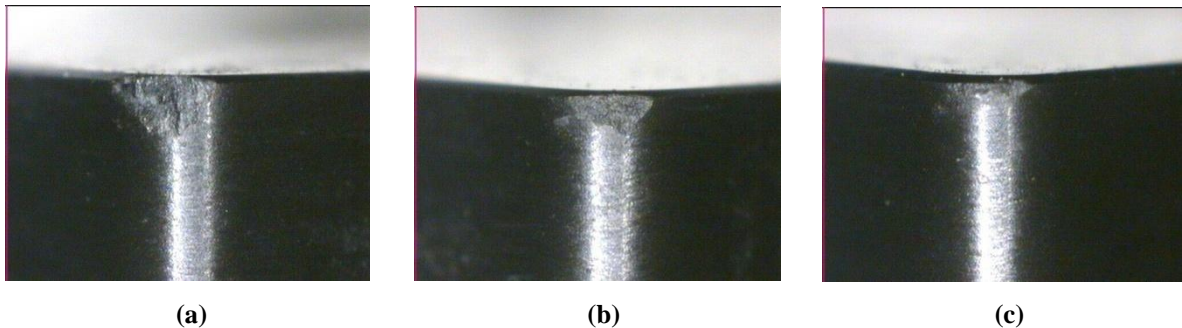


Figure 5.8 Tool wear under different cutting temperatures ($L_c = 10$ mm)
(a) 1080°C (b) 1260°C (c) 1350°C ($DOC = 0.2$ mm, $V_c = 1$ m/s, $f = 0.024$ mm/rev/tooth)

Chips

Figure 5.10 shows the discontinuous chips collected from laboratory experiments at the cutting temperature of 1350°C. They can be roughly divided into three sizes in chip length: small (<25 μm), medium (25-50 μm) and large (50-70 μm), which are indicated with the arrows by numbers 1, 2 and 3 in Figure 5.10b. They approximately account for 70%, 20% and 10% of the total chips, respectively. Note that with the cutting temperature increasing, both the chip size and the percentage of the large size tend to increase. One large chip is enlarged as in Figure 5.10c. The chip thickness is in the out-of-plane direction and the chip length in the arrow-indicated direction, since both the width and the length of the chip shown in Figure 5.10c are larger than the maximum uncut chip thickness (i.e., feed) of 0.024 mm. Moreover, the structural analysis indicates that the arrow-indicated direction is the cutting direction.

In the simulation, various chip sizes are also found as shown in Figure 5.11. A chip consists of a few particles which have the same color and closely contact each other. The circled chip in Figure 5.11, as an example, has chip length of 37 μm and the average thickness of about 6 μm . It can be obviously seen that the thickness falls within the range of the uncut chip

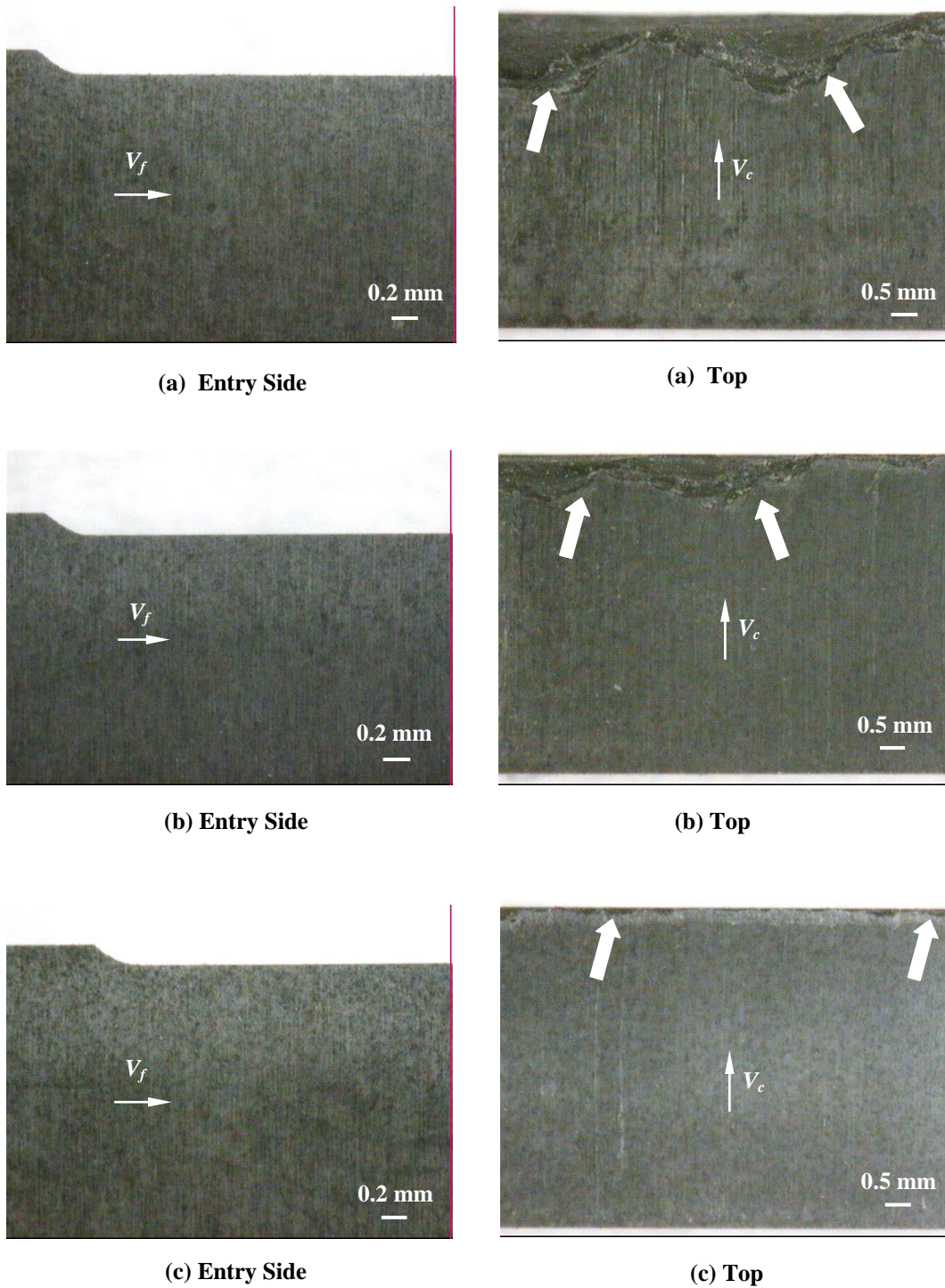


Figure 5.9 Exit edge chipping at different cutting temperatures (a) 1080°C (b) 1260°C (c) 1350°C (DOC = 0.2 mm, $V_c = 1$ m/s, $f = 0.024$ mm/rev/tooth)

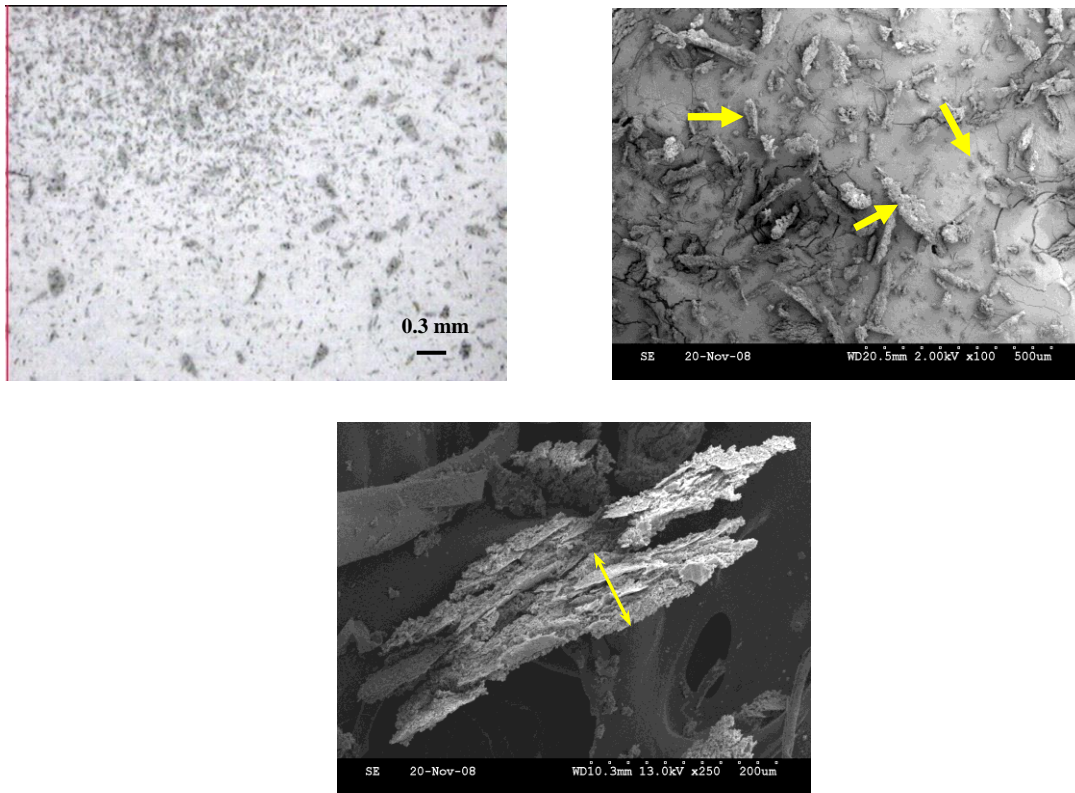


Figure 5.10 Chips in LAMill experiments ($T_c = 1350^\circ\text{C}$)
 (a) Chips in optical image (b) Chip sizes in SEM (c) Enlarged chip in SEM

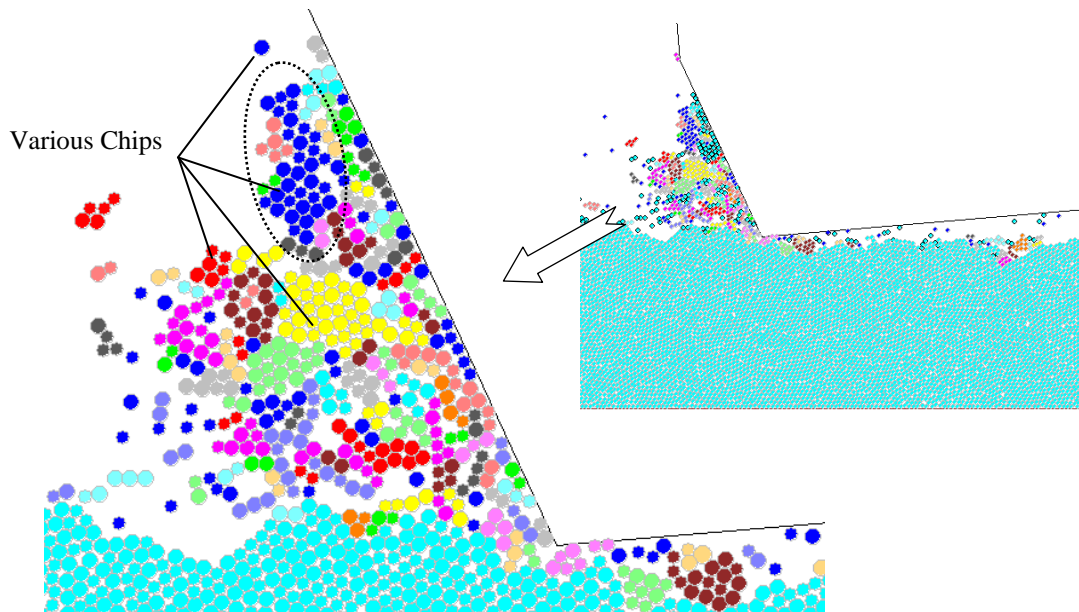


Figure 5.11 Chips in simulation ($T_c = 1350^\circ\text{C}$)

thickness and thus the chip belongs to the medium size. Note that due to running the short cutting length, it is unlikely to capture all the sizes of the chips shown in Figure 5.10 through simulation. However, both the simulations and the experiments demonstrate that the material removal of silicon nitride ceramics in LAMill is mainly realized by brittle fractures.

Surface/Subsurface Damages

Figure 5.12 illustrates the damage of a machined surface detected from laser confocal scan microscopy (LCSM). The operating conditions of the machined workpiece are: the depth of cut (*DOC*) of 0.2 mm and the cutting temperature of around 1200°C which is close to 1260°C in the simulation. The enlarged image in Figure 5.12 clearly shows that the subsurface damages are not uniformly distributed at the subsurface, which can also be seen in the simulation (Figure 5.13b). Figure 5.12 also shows that the measured depths of subsurface damage are generally less than 30 μm. In the simulation (Figure 5.13b), the maximum depth of subsurface damage (*d*) is about 27 μm. However, it should be mentioned that the value from the simulation does not fully represent the depth of subsurface damage in the machined workpiece. This is because the uncut chip thickness (*t'*) near the machined surface (Figure 5.2a) is smaller than the equivalent uncut chip thickness (*t*) used in the simulation (Figure 5.2b), which suggests that the actual depths of

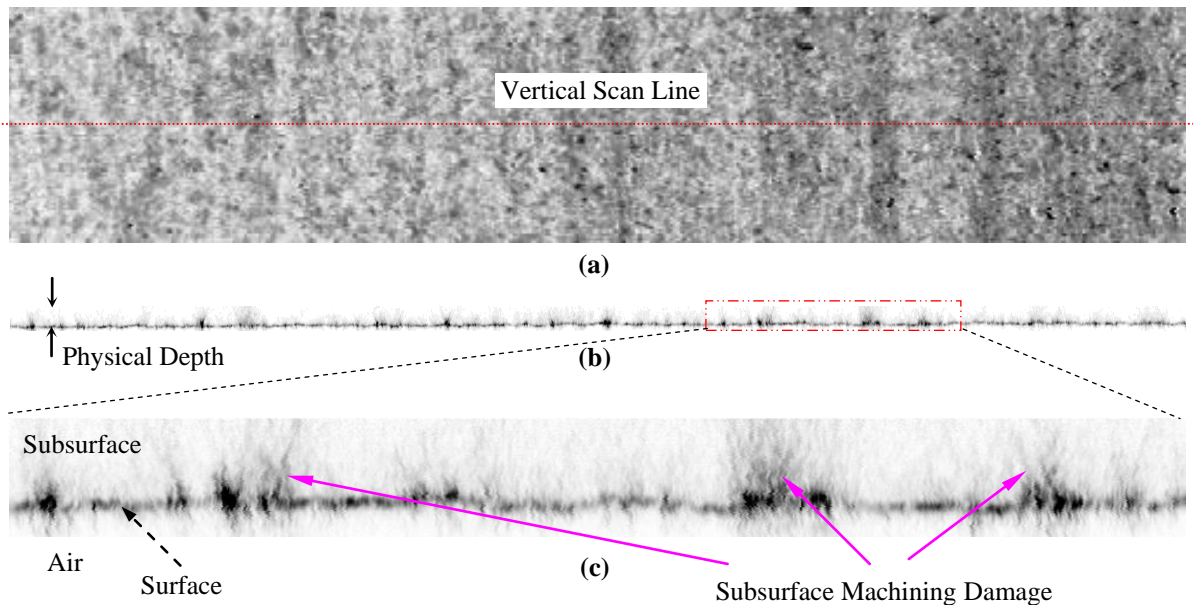


Figure 5.12 Subsurface damages detected from LCSM (a) Horizontal plane scan image (1 mm × 0.2 mm) (b) Vertical cross-sectional scan image (1 mm × 0.04 mm) (c) Enlarged image (0.2 mm × 0.04 mm)

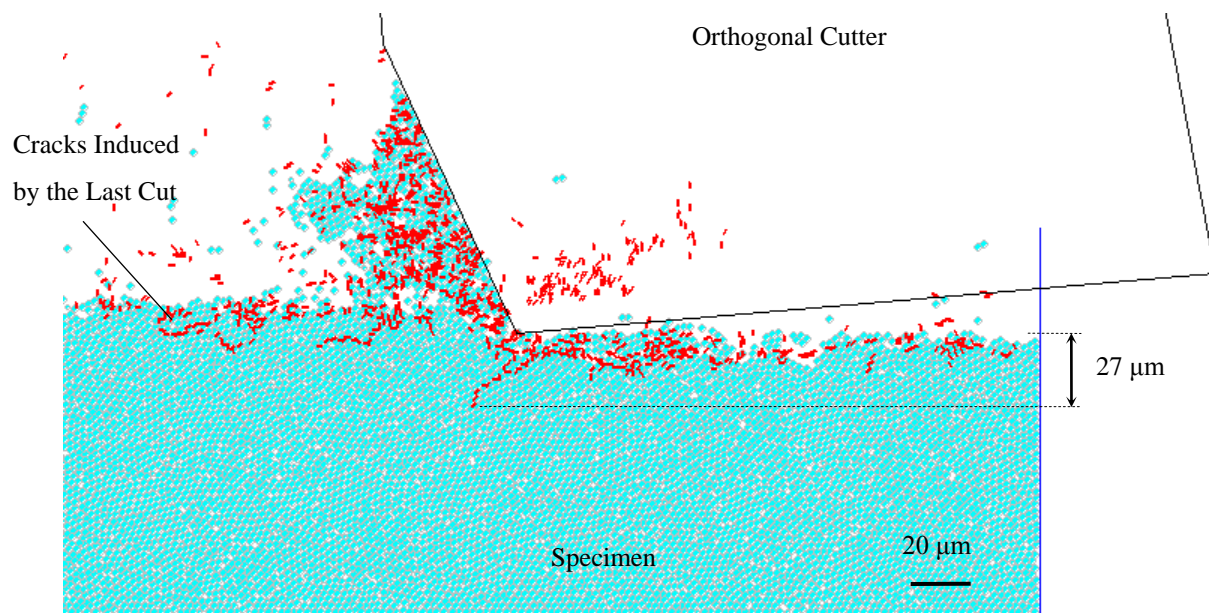


Figure 5.13 Surface/subsurface damages
 ($T_c = 1260^\circ\text{C}$, $\text{DOC} = 0.2 \text{ mm}$, $V_c = 1 \text{ m/s}$, $f = 0.024 \text{ mm/rev/tooth}$)

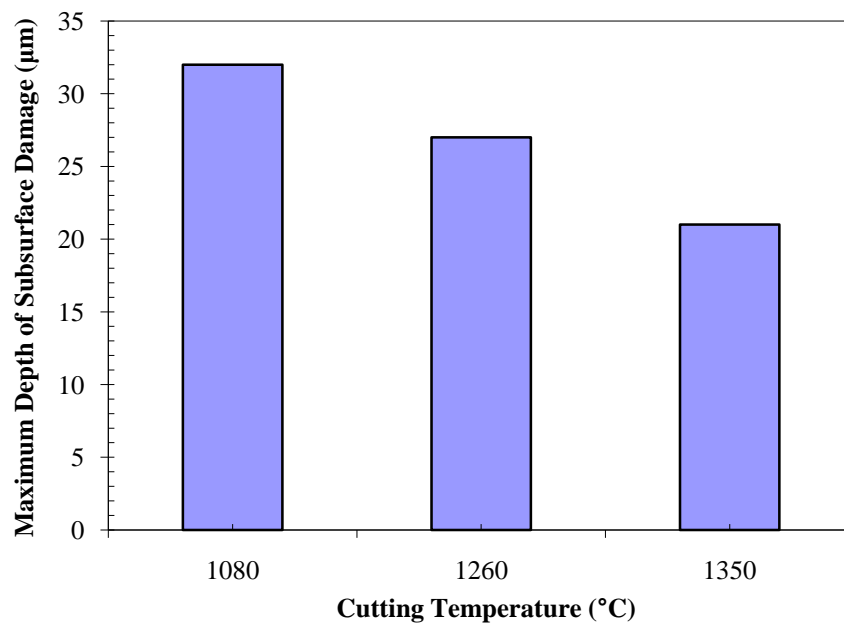


Figure 5.14 Comparison of the maximum subsurface damages (d) at different cutting temperatures

subsurface damage in the workpiece should be smaller than those predicted from the simulation (Figure 5.13b). In considering the small temperature difference between the detected workpiece and the specimen, the maximum depth of subsurface damage predicted are reasonable. Although currently the accurate relationship between the actual and the predicted maximum depths of subsurface damage cannot be given, it is true that its variations in actual machining can be reflected by those in the simulation as the operating conditions change.

Figure 5.14 shows a comparison of the maximum depth of subsurface damages (d) at the cutting temperature of 1080°C, 1260°C and 1350°C. It can be seen that, as expected, with the cutting temperature increasing, the maximum depth of subsurface damage decreases. That is, a large cutting temperature can cause a small subsurface damage for the machined workpiece.

Beware that the 2D nature of the simulation compounds the severity of dynamic behaviors mentioned above (e.g., high peak forces, long cracks). Actually, the shape of a particle in a PFC^{2D} model is a cylinder rather than a sphere, i.e., there are no variations in the third dimension and thus no allowance of additional grains with different orientations, which is obviously not the case in a real material. Therefore, it appears fair to say that the 2D specimen models the material in a simplified way that it also loses some fine features during the cutting simulation (resulting in more rugged behavior). But despite its 2D nature, the cutting simulation vividly depicts the brittle behavior of the material removal process of silicon nitride ceramic in LAMill.

5.6 Conclusions

The distinct element method (DEM) is an effective approach to simulating laser-assisted machining (LAM) of silicon nitride ceramics. The creation of a temperature-dependent specimen experimental results with model predictions. The machining mechanism governing LAM is analyzed from the aspects of material removal, cutting forces, chips, and surface/subsurface damages. Various sizes of the discontinuous chips from the simulations and the experiments demonstrate that the fundamental mechanism of material removal in LAMill is mainly realized by brittle fractures. High cutting temperature can decrease the cutting force, tool wear, exit edge chipping and surface/subsurface damages. Moreover, the temperature range of brittle-to-ductile transition is recommended to be avoided in LAMill. However, there is still some work to be done next, such as extending the 2D model to 3D, improving the computing efficiency, etc.

References

- Ajjarapu, S. K., Fesperman, R. R., Patten, J. A., and Cherukuri, H. P., (2004). Experimental and numerical investigation of ductile regime machining of silicon nitride. AIP Conference Proceedings, 712, 1377-1383.
- Allor, R. L., Jahanmir, S. (1996). Current problems and future directions for ceramic machining. American Ceramic Society Bulletin, 75(7), 40-43.
- Anderson, M. C., and Shin, Y. C. (2006). Laser-assisted machining of an austenitic stainless steel: P550. Proceedings of the Institution of Mechanical Engineers, Part B (Journal of Engineering Manufacture), 220(B12), 2055-67.
- ANSYS Inc.. ANSYS (finite element analysis package), Release 11.0.
- Atanasov, P. A., Eugenieva, E. D., and Nedialkov, N. N. (2001). Laser drilling of silicon nitride and alumina ceramics: a numerical and experimental study. Journal of Applied Physics, 89(4), 2013-2016.
- ASTM Standard E1426, 98 (2003) Standard test method for determining the effective elastic parameter for x-ray diffraction measurements of residual stress. ASTM International, West Conshohocken, PA, DOI: 10.1520/E1426-98R03, www.astm.org.
- ASTM (2006a). Standard test method for flexural strength of advanced ceramics at ambient temperatures, Annual Book of ASTM Standard: Designation: C 1161-02c, 15.01, 217-232.
- ASTM (2006b). Standard test method for determination of fracture toughness of advanced ceramics at ambient temperature. Annual Book of ASTM Standard: Designation: C 1421-01b, 15.01, 626-659.
- Bass, M., Beck, D., and Copley, S. M. (1979). Laser-assisted machining. Proceedings of the Society of Photo-Optical Instrumentation Engineers, Fourth European Electro-Optics Conference, 164, 233-40.
- Batha H. D., Whitney, E. D. (1973). Kinetics and mechanism of the thermal decomposition of Si_3N_4 . Journal of the American Ceramic Society 56(7): 365-369.
- Beltrao, P. A., Gee, A. E., Corbett, J., Whatmore, R. W., Goat, C. A., and Impey, S. A. (1999). Single point diamond turning of ferroelectric materials. Ferroelectrics, 228(1-4), 229-239.
- Bhattacharyya, B., Doloi, B. N., and Sorkhel, S. K. (1999). Experimental investigations into electrochemical discharge machining (ECDM) of non-conductive ceramic materials. Journal of Materials Processing Technology, 95(1-3), 145-154.
- Bifano, T. G., Dow, T. A., and Scattergood, R. O. (1988). Ductile-regime grinding: a new technology for machining brittle materials. American Society of Mechanical Engineers (ASME), 113-120.
- Blackley, W. S., and Scattergood, R. O. (1991). Ductile-regime machining model for diamond turning of brittle materials. Precision Engineering, 13(2), 95-103.

- Bushby A. J. (1994). Surface oxidation of a sintered silicon nitride: implications for mechanical properties. *International Ceramic Monograph, Proceedings of the International Ceramics Conference Austceram*, 94(2): 1007-1012.
- Chandrasekaran, N. (1997). Molecular dynamics simulations of machining, materials testing, and tribology at the atomic scale. Ph.D. Thesis, Oklahoma State University, USA.
- Chang, C.-W., and Kuo, C.-P. (2007). An investigation of laser-assisted machining of Al₂O₃ ceramics planing”, *International Journal of Machine Tools & Manufacture*, 47(3-4), 452-461.
- Chermant, J. L., and Coster, M. (2002). Modeling of ceramic microstructure. *Key Engineering Materials*, 206-213(1), 593-599.
- Ching, Y. H., Mao, Y. W., and Shin, Y. L. (2008). A quasi-steady-state thermal model for laser-assisted cutting of zirconia ceramics. *Key Engineering Materials*, 364-366(2), 1003-1008.
- Churchill, S. W., and Chu, H. H. S. (1975). Correlating equations for laminar and turbulent free convection from a vertical plate. *International Journal of Heat and Mass Transfer*, 18(9), 1049-1053.
- Clinton, D. J. (1971-1972). Preparation and ion beam machining of ceramic materials for transmission electron microscopy. *Micron*, 3(3), 358-372.
- Copley, S. (1985). Laser applications. *Handbook of High Speed Machining Technology* edited by R. King, Chapman Hall, New York, 387-416.
- Cundall, P. A. (1971). A computer model for simulating progressive large scale movements in blocky rock systems. *Proceedings of the Symposium of the International Society of Rock Mechanics (Nancy, France, 1971)*, 1, Paper No. II-8.
- Cundall, P. A. (1987). Distinct element models of rock and soil structure. *Analytical and Computational Methods in Engineering Rock Mechanics*, 4, 129-163.
- Ceradyne Inc.. (2006). www.ceradyne.com, Silicon Nitride Property Data - 2006,
- Desilets, B. H. (1978). Mechanism of cavity formation in unfired ceramic by electron-beam machining”, *journal of vacuum science and technology*. 15(3), 1056-1059.
- Ehmann, K. F., Kapoor, S. G., DeVor, R. E., and Lazoglu, I. (1997). Machining process modeling: a review. *Journal of Manufacturing Science and Engineering, Transactions of the ASME*, 119(4(B)), 655-663.
- Falk, L. K. L., Schneider, N., Menke, Y., and Hampshire, S. (2007). The intergranular oxynitride microstructure in silicon nitride based ceramics. *Materials Science Forum*, 554, 113-118.
- Faulk, N. M. (1993). Electrical discharge machining of advanced ceramics. *NIST Special Publication*, 847, 525-534.
- Fok, S. L., Mitchell, B. C., Smart, J., and Marsden, B. J. (2001). A numerical study on the application of the Weibull theory to brittle materials. *Engineering Fracture Mechanics*, 68(10), 1171-1179.
- Fukuzawa, Y. Y., Mohri, N. N., and Tani, T. T. (2002). Electrical discharge machining of insulating si₃n₄ ceramics. *Praktische Metallographie*, 39(10), 529-41.

- Geng, H. (Editor) (2004). *Manufacturing Engineering Handbook*, McGraw-Hill Professional.
- Germain, G., Morel, F., Lebrun, J.-L., Morel, A., and Huneau, B. (2006). Effect of laser assistance machining on residual stress and fatigue strength for a bearing steel (100Cr6) and a titanium alloy (Ti6Al4V). *Materials Science Forum*, 524-525, 569-74.
- Goldstein, R. J., Sparrow, E. M., and Jones, D. C. (1973). Natural convection mass transfer adjacent to horizontal plates. *International Journal of Heat and Mass Transfer*, 16(5), 1025-1035.
- Gou, C., and Chand, R. H. (1995). Grindability of ceramics. *Proceedings of The Society of Manufacturing Engineers*, Edited by R. H. Chand, Michigan, 125-136.
- Guo, Z. (1998). Experimental and numerical analysis of abrasive waterjet drilling of brittle materials. Ph.D Dissertation, University of Washington, USA.
- Guo, Z., and Ramulu, M. (2001). Investigation of displacement fields in an abrasive waterjet drilling process: part 1. experimental measurements. *Experimental Mechanics*, 41(4), 375-387.
- Gutierrez, G., and Araya, J. G. (2004). Analytical solution for a transient three-dimensional temperature distribution in laser-assisted machining processes. *Proceedings of the ASME Heat Transfer/Fluids Engineering Summer Conference 2004*, 3, 1055-1063.
- Hahn, R., Lost, C., and Schulze, P. (1993). Ultrasonic shaping: an economical procedure to machine complex ceramic components. *NIST Special Publication*, 847, 385-389.
- Hazzard, J. F., Young, R. P., and Maxwell, S. C. (2000). Micromechanical modeling of cracking and failure in brittle rocks. *Journal of Geophysical Research*, 105(B7), 16683-16697.
- Hampshire, S. (1991). Engineering properties of nitrides. *Ceramics and Glasses, Engineered Materials Handbook*, 4, The Materials Information Society, 812-820.
- Heuvelman C. J., König W., Töenshoff H. K., Meijer J., Kirner P. K., Rund M., Schneider M. F., van Sprang I. (1992). Surface treatment techniques by laser beam machining. *CIRP Annals* 41(2): 657-666.
- Hibi, Y., Enombto, Y., Kikuchi, K., Shikata, N., and Ogiso, H. (1995). Excimer laser-assisted chemical machining of SiC ceramic. *Applied Physics Letters*, 66(7), 817-18.
- Howlett S. P., Morrell R., Taylor R. (1986). The effects of oxidation on the thermal diffusivity of reaction bonded silicon nitride. *British Ceramic Proceedings*, 37: 81-94.
- Huang, H. (1999). Discrete element modeling of tool-rock interaction. Ph.D. Thesis, University of Minnesota, Minneapolis, Minnesota, USA.
- Itasca Consulting Group, Inc. (2002). *PFC^{2D} Manual - FISH, Command, Theory and Background*, V3.0, Minneapolis, Minnesota.
- Incropera, F. P. and Dewitt, D. P. (1996). *Fundamentals of Heat and Mass Transfer*, John Wiley & Sons, 4th Edition.
- Ito, S., Nakamura, M., and Kanematsu, W. (1987). Machining of high performance ceramics. *Bulletin of the Japan Society of Precision Engineering*, 21(3), 167-172.

- Ives, I. K., Evans, C. J., Jahanmir, S., Polvani, R. S., Strakna, T. J., and McGlaufflin, M. L. (1993). Effect of ductile-regime grinding on the strength of hot-isostatically-pressed silicon nitride. NIST Special Publication, 847, 341-352.
- Iwanek, H., Grathwohl, G., Hamming, R., and Brugger, N. (1986). Machining of ceramics by different methods. Verlag Deutsche Keramische Gesellschaft, 417-423.
- Jain, N. K., and Jain, V. K. (2001). Modeling of material removal in mechanical type advanced machining processes: a state-of-art review. International Journal of Machine Tools and Manufacture, 41(11), 1573-1635.
- Janvrin, B. C. (1996). Neodymium-YAG laser-assisted turning of difficult-to-machine silicon nitride. Ph.D. Dissertation, Iowa State University, USA.
- Jau, B. M., Copley, S. M., and Bass, M. (1981). Laser-assisted machining. Manufacturing Engineering Transactions, pp. 12-15.
- Jen, T.-C., Chen, Y.-M., and Tuchowski, F. (2004). Experimental and numerical studies of laser-assisted drilling processes. Proceedings of the ASME Heat Transfer/Fluids Engineering Summer Conference 2004, HT/FED, 3, 1015-1023.
- Jeon, Y., and Pfefferkorn, F. E. (2005). Effect of laser preheating the workpiece on micro-end milling of metals. American Society of Mechanical Engineers, Manufacturing Engineering Division, MED, 16-1, 479-488.
- Jeon, Y., and Pfefferkorn, F. E. (2008). Effect of laser preheating the workpiece on micro end milling of metals. Journal of Manufacturing Science and Engineering, Transactions of the ASME, 130(1), 0110041-0110049.
- Jerby, E., Dikhtyar, V., and Aktushev, O. (2003). Microwave drill for ceramics. American Ceramic Society Bulletin, 82(1), 35-37.
- Jia, Z., Zhang, J., Ai, X., and Ai, Z. (1995). Combined machining of USM and EDM for advanced ceramics. Journal of Advanced Materials, 26(3), 16-20.
- Jin, Q., Wilkinson, D. S., Weatherly, G. C., Luecke, W. E., and Wiederhorn, S. M. (2001). thickness alteration of grain-boundary amorphous films during creep of a multiphase silicon nitride ceramic. Journal of the American Ceramic Society, 84(6), 1296-1300.
- Kaitkay, P. (2002). Modeling of rock cutting using distinct element method. Master Thesis, Kansas State University, Manhattan, Kansas, USA.
- Kawai, C., and Yamakawa, A. (1997). Effect of porosity and microstructure on the strength of Si₃N₄: designed microstructure for high strength, high thermal shock resistance, and facile machining”, Journal of the American Ceramic Society, 80(10), 2705-2708.
- Khosrofian, J. M., and Garetz, B. A. (1983). Measurement of a Gaussian laser beam diameter through the direct inversion of knife-edge data. Applied Optics 22(21), 3406-10.
- Kiso, H., Taguchi, T., Fukuhara, M., and Kimura, T. (1987). Machining of advanced ceramics by turning with sintered polycrystalline diamond tool. Bulletin of the Japan Society of Precision Engineering, 21(2), 142-143.

- Komanduri, R., and Raff, L. M. (2001). A Review on the molecular dynamics simulation of machining at the atomic scale. *Proceedings of the Institution of Mechanical Engineers*, 215 Part B, 1639-1672.
- Koshy, P., Dumitrescu, P., Stenekes, J., and Elbestawi, M. A. (2006). High-power diode laser assisted hard turning of AISI D2 tool steel”, *International Journal of Machine Tools & Manufacture*, 46(15), 2009-2016.
- Kotrc, M. and Uebel, J. (2005). Modeling and simulation in ceramics with the PFC particle method. *Ziegelindustrie International*, 12, 14-21.
- Kumbera, T. G., Cherukuri, H. P., Patten, J. A., Brand, C. J., and Marusich, T. D. (2001). Numerical simulations of ductile machining of silicon nitride with a cutting tool of defined geometry. *Machining Science and Technology*, 5(3), 341-352.
- König, W., Dauw, D. F., Levy, G., and Panten, U. (1988). EDM-future steps towards the machining of ceramics. *Annals CIRP*, 37(2), 623-631.
- König, W., Treppe, F., and Zaboklicki, A. (1992). Laser-assisted milling: an innovative technology for hardly cuttable materials. *VDI-Z*, 134(2), 43-48.
- König, W., and Zaboklicki, A. K. (1993). “Laser-assisted hot machining of ceramics and composite materials. *NIST Special Publication*, 847, 455-463.
- König, W., and Zaboklicki, A. K. (1994). Laser-assisted hot machining processes: technological potentials. *Laser-Assisted Net Shape Engineering Proceedings of the LANE’94*, 1, 389-404.
- Lange, F. F. (1972). Dense Si₃N₄ and SiC: some critical properties for gas turbine application. *The Gas Turbine and Fluids Engineering Conference & Producers Show - American Society of Mechanical Engineering*, San Francisco, 1-8.
- Lavrenko V. A., Gogotsi Y. G., Goncharuk A. B., Alekseev A. F., Grigorev O. N., Shcherbina O. D. (1985). High-temperature oxidation of reaction-sintered silicon nitride with various additions. *Soviet Powder Metallurgy and Metal Ceramics* 24(3), 207-210.
- Lavrinovich, A. V., Kryl, Y. A., Androsov, I. M., and Artemyuk, S. A. (1990). Effect of dimensional laser machining on the structure and properties of silicon nitride. *Soviet Powder Metallurgy and Metal Ceramics*, 29(4), 328-32.
- Ledgerwood, R. (2007). PFC modeling of rock cutting under high pressure conditions”, *Rock Mechanics: Meeting Society’s Challenges and Demands*, *Proceedings of the 1st Canada-US Rock Mechanics Symposium*, Vancouver, Canada, 511-518.
- Lee, T. C., and Lau, W. S. (1991). Some characteristics of electrical discharge machining of conductive ceramics. *Materials and Manufacturing Processes*, 6(4), 635-648.
- Lee, W. E., and Rainforth, W M. (1994). *Ceramic Microstructures Property Control by Processing*, Chapman & Hall, New York.
- Lei, S., and Yang, B. (2005). Distinct element simulation of ceramic machining: material removal mechanism. *Transactions of the North American Manufacturing Research Institute of SME*, 33, 485-492.

- Lei, S., and Kaitkay, P. (2002). Micromechanical modeling of rock cutting under pressure boundary conditions using distinct element methods. *Transactions of the North American Manufacturing Research Institution of SME*, 30, 207-214.
- Lei, S., Shin, Y. C. and Incropera, F. P. (2001). Mechanical characteristics in laser-assisted machining of silicon nitride ceramics. *ASME Journal of Manufacturing Science and Engineering*, 123, 639-646.
- Lim, H.-J., Lim, Y.-M., Kim, S. H., and Kwak, Y. K. (2001). Self-aligned micro tool and electrochemical discharge machining (ECDM) for ceramic materials. *Proceedings of the SPIE - The International Society for Optical Engineering*, 4416, 348-353.
- Liu, X., and Zhang, B. (2002). Machining simulation for ceramics based on continuum damage mechanics. *Journal of Manufacturing Science and Engineering, Transactions of the ASME*, 124(3), 553-561.
- Lloyd, J. R. and Moran, W. R. (1974). Natural convection adjacent to horizontal surfaces of various planforms. *Transactions of the ASME, Series C, Journal of Heat Transfer*, 96(4), 443-447.
- Lu, C., Danzer, R., and Fischer, F. D. (2002). Fracture statistics of brittle materials: Weibull or normal distribution. *Physical Review E (Statistical, Nonlinear, and Soft Matter Physics)*, 65(6), 067102/1-4.
- Maiti, S., and Geubelle, P. H. (2004). Mesoscale modeling of dynamic fracture of ceramic materials. *Computer Modeling in Engineering & Sciences*, 5(2), 91-101.
- Marinescu I. D. (1998). Laser-assisted grinding of ceramics. *InterCeram: International Ceramic Review*, 47(5), 314-316.
- Martin, C., Cales, B., Vivier, P., and Mathieu, P. (1989). Experimental investigation of thermo-electrical discharge machinable ceramic composites. *Materials Science & Engineering A: Structural Materials: Properties, Microstructure and Processing*, A109(1-2), 351-356.
- Matsubara, H. (1999). Computational modeling of ceramic microstructure by mc and MD aspect in dynamics. *Key Engineering Materials*, 166, 1-8.
- Maruo H., Miyamoto I., Ooie T. (1992). Processing mechanism of ceramics with high intensity lasers. *Proceedings of LAMP'92 Nagaoka*, 293-298.
- Mayer, J. E. Jr., and Fang, G. P. (1993). Diamond grinding of silicon nitride ceramic. *NIST Special Publication*, 847, 205-222.
- McColm I. J. (1983). *Ceramic Science for Materials Technologists*. Leonard Hill, Chapman and Hall, New York.
- Mikhailova G. N., Mikhailov B. P., Troitskii, A. V. (2004). Laser welding of HTSC ceramics. *Laser Physics Letters*, 1(10), 525-527.
- Miyamoto, I., Taniguchi, N., and Kawata, K. (1984). Surface finishing of single crystal and polycrystal alumina ceramics by ion beam machining", *Japan Soc of Precision Engineering*, 502-507.
- Moore, D. M. (1986). Ultrasonic impact grinding. *Carbide and Tool Journal*, 21-23.

- Morita N. (1993). Crack-free processing of hot-pressed silicon nitride ceramics using pulsed YAG laser. NIST Special Publication, 847, 517-526.
- Munakata, Y., and Senda, T. (1990). Tensile strength of cracked ceramic specimens in lower-quality-fuelled combustion gas streams. *High temperature technology*, 8(4), 252-256.
- Munz, D., Rosenfelder, O., Goebbels, K., and Reiter, H. (1986). Assessment of flaws in ceramic materials on the basis of non-destructive evaluation. *Fracture Mechanics of Ceramics*, 7, 265-283.
- Mutoh Y., Miyahara N., Yamaishi K., Oikawa, T. (1993). High temperature fracture toughness in silicon nitride and sialon. *Transactions of the ASME, Journal of Engineering Materials and Technology*, 115(3), 268-272.
- Müecklich, F., Ohser, J., Blank, S., Katrakova, D., and Petzow, G. (1999). Stereological analysis of grain size and grain shape applied to silicon nitride ceramics. *Zeitschrift fuer Metallkunde/Materials Research and Advanced Techniques*, 90(8), 557-561.
- Pei, Z. J. (1995). Rotary ultrasonic machining of ceramic characterization and extensions. Ph.D Dissertation, University of Illinois at Urbana-Champaign, USA.
- Petzow, G., and Greil, P. (1988). Dense silicon nitride processing, properties and applications. *Powder Metallurgy and Related High Temperature Materials: Proceedings of the 4th International Conference*, P. Ramakrishnan (Editor), Bombay, Trans Tech Publications.
- Pfefferkorn F. E., Shin Y. C., Tian, Y., Incropera, F. P. (2004). Laser-assisted machining of magnesia-partially-stabilized zirconia. *Journal of Manufacturing Science and Engineering, Transactions of the ASME*, 126(1), 42-51.
- Pfefferkorn, F. E., Incropera, F. P., and Shin, Y. C. (2005). Heat transfer model of semi-transparent ceramics undergoing laser-assisted machining. *International Journal of Heat and Mass Transfer*, 48(10), 1999-2012.
- Poduraev, V. N., Sokolov, N. M., and Berenov, N. D. (1989). Plasma-assisted machining of large components made of difficult-to-machine materials. *Soviet Engineering Research*, 9(9), 53-58.
- Potyondy, D. O., and Cundall, P. A. (1999). Modeling of notch-formation mechanisms in the url mine-by tunnel: phase IV - Cundall enhancements to the PFC model of rock", Itasca Consulting Group, Inc., Report to Atomic Energy of Canada Limited (AECL), Issued as Ontario Hydro Nuclear Waste Management Division Report No. 06819-REP-01200-10002-R00.
- Potyondy, D. O., and Cundall, P. A. (2004). A bonded-particle model for rock. *International Journal of Rock Mechanics and Mining Science*, 41, 1329-1364.
- Rajagopal, S. (1982). Laser-assisted machining of tough materials. *Laser Focus*, 18(3), 49-54.
- Rebro, P. A., Shin, Y. C., and Incropera, F. P. (2004). Design of operating conditions for crackfree laser-assisted machining of mullite. *International Journal of Machine Tools and Manufacture*, 44(7-8), 677-694.
- Rice, R. W. (1993). Effects of ceramic microstructural character on machining direction – anisotropy. *Machining of Advanced Materials - NIST Special Publication*, 847, 185-204.

- Roy, S., and Modest, M. F. (1993), CW laser machining of hard ceramics: I. effects of three-dimensional conduction, variable properties and various laser parameters. *International Journal of Heat and Mass Transfer*, 36(14), 3515-3528.
- Rozzi, J. C. (1997). Experimental and theoretical evaluation of the laser-assisted machining of silicon nitride. Ph.D Dissertation, Purdue University, USA.
- Rozzi, J. C., Pfefferkorn, F. E., Incropera, F. P., and Shin, Y. C. (1998). Transient thermal response of a rotating cylindrical silicon nitride workpiece subjected to a translating laser heat source, part I: comparison of surface temperature measurements with theoretical results”, *Journal of Heat Transfer, Transactions ASME*, 120(4), 899-905.
- Rozzi, J. C., Incropera, F. P., and Shin, Y. C. (1998). Transient thermal response of a rotating cylindrical silicon nitride workpiece subjected to a translating laser heat source, part II: parametric effects and assessment of a simplified model. *Journal of Heat Transfer, Transactions ASME*, 120(4), 907-915.
- Rouxel, T. (2002). Young's modulus and fracture toughness of silicon nitride ceramics at elevated temperature. *Materials Science Forum*, 383, 3-11.
- Rühle, M. (1985). Ceramic microstructures and properties. *Journal of Vacuum Science & Technology A: Vacuum, Surfaces, and Films*, 3(3), 749-756.
- Sadat, A. B. (1999). Machining of advanced ceramics. American Society of Mechanical Engineers, Petroleum Division (Publication) PD, Tribology, 1-4.
- Sala, A. (1986). Radiant properties of materials: tables of radiant values for black body and real materials, PWN-Polish Scientific Publishers, 274.
- Samant, A. N., and Dahotre, N. B. (2008). Computational predictions in single-dimensional laser machining of alumina. *International Journal of Machine Tools and Manufacture*, 48(12-13), 1345-1353.
- Samant, A. N., and Dahotre, N. B. (2008). Ab initio physical analysis of single dimensional laser machining of silicon nitride. *Advanced Engineering Materials*, 10(10), 978-981.
- Samant, A. N., and Dahotre, N. B. (2009). An integrated computational approach to single-dimensional laser machining of magnesia. *Optics and Lasers in Engineering*, 47(5), 570-577.
- Samant, A. N., and Dahotre, N. B. (2009). Differences in physical phenomena governing laser machining of structural ceramics Source. *Ceramics International*, 35(5), 2093-2097.
- Samant, A. N., Daniel, C., Chand, R. H., Blue, C. A., and Dahotre, N. B. (2009). Computational approach to photonic drilling of silicon carbide. *International Journal of Advanced Manufacturing Technology*, 45(7-8), 704-713.
- Samant A. N., and Dahotre, N. B. (2009). Physical effects of multipass two dimensional laser machining of structural ceramics. *Advanced Engineering Materials*, 11(7), 579-585.
- Sanchez, J. A., Cabanes, I., Lopez de Lacalle, L. N., and Lamikiz, A. (2001). Development of optimum electrodischarge machining technology for advanced ceramics. *International Journal of Advanced Manufacturing Technology*, 18(12), 897-905.

- Sarfaraz, M. A., Yau, Y.-W., and Sandhu, N. S. (1993). Electron beam machining of ceramic green-sheets for multilayer ceramic electronic packaging applications. *Nuclear Instruments & Methods in Physics Research, Section B: Beam Interactions with Materials and Atoms*, 82(1), 116.
- Sakai, K., and Suzuki, Y. (2005). Laser-assisted turning of hardened steel. 24th International Congress on Applications of Lasers and Electro-Optics, ICALEO 2005 - Congress Proceedings, 719-722.
- Sarkar, B. R., Doloi, B., and Bhattacharyya, B. (2006). Parametric analysis on electrochemical discharge machining of silicon nitride ceramics. *International Journal of Advanced Manufacturing Technology*, 28(9), 873-881.
- Saurwalt, J. J. (1993). Development of a predictive grinding model for the high-quality machining of engineering ceramics. *SME Technical Paper (Series) MR*, 1-20.
- Schwartz, M. (1992). *Handbook of Structural Ceramics*, McGraw-Hill, Inc., New York.
- Shen, X., and Lei, S. (2004). Three-dimensional heat transfer and thermal stress analysis for laser-assisted milling of silicon nitride ceramics. The 6th International Conference on Frontiers of Design and Manufacturing, June 21-23, Xi'an, China.
- Shen, X., Liu, W., and Lei, S. (2005). Three-dimensional thermal analysis for laser-assisted milling of silicon nitride ceramics using FEA. *American Society of Mechanical Engineers, Manufacturing Engineering Division, MED*, 16-1, 445-452.
- Shen, X., and Lei, S. (2008). Investigation on operating temperature in laser-assisted milling of silicon nitride ceramics. *Proceedings of the 2008 International Manufacturing Science And Engineering Conference*, October 7-10, 2008, Evanston, Illinois, USA.
- Shen X., Lei S. (2009). Thermal modeling and experimental investigation for laser-assisted milling of silicon nitride ceramics. *Journal of Manufacturing Science and Engineering, Transactions of the ASME*, 131(5): 051007-1-10.
- Shen, X., and Lei, S. (2005). Distinct element simulation of laser-assisted machining of silicon nitride ceramics: surface/subsurface cracks and damage. *American Society of Mechanical Engineers, Manufacturing Engineering Division, MED*, 16-2, 1267-1274.
- Shen, X., and Lei, S. (2006). Numerical fracture toughness test for improving workpiece model in machining simulation. *Transactions of the North American Manufacturing Research Institute of SME*, 34, 285-292.
- Shen, X., and Lei, S. (2009a). Cutting simulation of laser-assisted milling of silicon nitride ceramics using PFC^{2D}. *Proceedings of the ASME 2009 International Manufacturing Science and Engineering Conference MSEC2009*, West Lafayette, Indiana, USA.
- Shen, X., and Lei, S. (2009b). A study on the effects of microparameters on macroproperty of flexural strength of synthetic silicon nitride ceramics modeled by bonded particles. *Journal of Materials Science*, (under review).
- Shen, X., Yang, B., and Lei, S. (2009). Numerical modeling and simulation of laser-assisted machining of silicon nitride ceramics with distinct element method (DEM): part II,

- simulation of the dynamic cutting process”, Transactions of the ASME, Journal of Manufacturing Science and Engineering, (under review)
- Sheppard, L. M. (1987). Machining of advanced ceramics. *Advanced Materials & Processes*, 132(6), 40-43, 46-48.
- Sheppard, L. M. (1990). automotive performance accelerates with ceramics. *American Ceramic Society Bulletin*, 69(6), 1012-1021.
- Shin, Y. C., Lei, S., Pfefferkorn, F. E., Rebro, P., Rozzi, J. C., and Incropera, F. P. (2000). Thermally (laser and plasma) assisted machining: its potential and future. *Abrasives*, April/May, 16-23.
- Shiu, W., Donze, F. V., and Daudeville, L. (2008). Compaction process in concrete during missile impact: a DEM analysis. *Computers and Concrete*, 5(4), 329-342.
- Siegal, R., and Howell, J. R. (1981). *Thermal Radiation Heat Transfer*, 2nd Edition, McGraw-Hill Book Company.
- Singhal S. C. (1976). Thermodynamics analysis of the high temperature stability of silicon, nitrogen, silicon-nitride. *Ceramurgia*, 2, 123-130.
- Singh, R. and Melkote, S. N. (2007). Characterization of a hybrid laser-assisted mechanical micromachining (LAMM) process for a difficult-to-machine material. *International Journal of Machine Tools and Manufacture*, 47(7-8), 1139-1150.
- Singh, R., Alberts, M. J., and Melkote, S. N. (2008). Characterization and prediction of the heat-affected zone in a laser-assisted mechanical micromachining process. *International Journal of Machine Tools and Manufacture*, 48(9), 994-1004.
- Smotritskii, A. V., Zinov'ev, V. E., Starostin, A. A., Korshunov, I. G., and Petrovskii, V. Ya. (1996). Thermal properties of silicon nitride-based ceramics at high temperatures. *High Temperature*, 34(4), 541-545.
- Spector, C. J. (1977). Real-time sensor for localized pressure in e-beam machining. *IBM Technical Disclosure Bulletin*, 19(8), 3121.
- Srawley, J. E., and Gross, B. (1976). Side-cracked plates subject to combined direct and bending forces. *Cracks and Fracture*, ASTM STP 601, 559-579.
- Strenkowski, J. S., and Hiatt, G. D. (1990). Technique for predicting the ductile regime in single point diamond turning of brittle materials. *American Society of Mechanical Engineers, Production Engineering Division (Publication) PED, Fundamental Issues in Machining*, 43, 67-80.
- Tan, Y., Yang, D., Li, C. and Sheng, Y. (2008a). Discrete element method simulation of cracks in monocrystalline silicon machining process. *Zhongguo Jixie Gongcheng/China Mechanical Engineering*, 19(21), 2545-2548+2581.
- Tan, Y., Yang, D., and Sheng, Y. (2008b), Study of polycrystalline Al₂O₃ machining cracks using discrete element method. *International Journal of Machine Tools and Manufacture*, 48(9), 975-982.
- Taguchi S. P., Ribeiro S. (2004). Silicon nitride oxidation behaviour at 1000 and 1200°C. *Journal of Materials Processing Technology*, 147(3), 336-342.

- Tavarez, F. A., Plesha, M. E., and Bank, L. C. (2002). Discrete element method (DEM) for modeling solid and particulate media. Geotechnical Special Publication, 117, 155-160.
- Themelin L., D. M. and Billy M. (1993). Oxidation behaviour of a hot isostatically pressed silicon nitride material. Journal De Physique, IV(3), 881-888.
- Tian Y. Shin Y.C. (2006). Laser-assisted machining of damage-free silicon nitride parts with complex geometric features via in-process control of laser power. Journal of the American Ceramic Society, 89(11), 3397-3405.
- Tian, Y., and Shin, Y. C. (2006). Thermal modeling for laser-assisted machining of silicon nitride ceramics with complex features. Transactions of the ASME, Journal of Manufacturing Science and Engineering, 128(2), 425-34.
- Tian, Y., Wu, B., and Shin, Y. C. (2006). Laser-assisted milling of silicon nitride ceramics. Proceedings of the International Conference on Manufacturing Science and Engineering, MSEC 2006, 7.
- Tian, Y., and Shin, Y. C. (2007). Multiscale finite element modeling of silicon nitride ceramics undergoing laser-assisted machining. Transactions of the ASME, Journal of Manufacturing Science and Engineering, 129(2), 287-295.
- Tian, Y., Wu, B., Anderson, M., and Shin, Y. C. (2008). Laser-assisted milling of silicon nitride ceramics and inconel 718. Journal of Manufacturing Science and Engineering, 130(3), 031013-1-9.
- Touloukian, Y.S. (Editor) (1967). Thermophysical properties of High Temperature Solid Materials TPRC, NY, MacMillian.
- Touloukian, Y. S. and DeWitt, D. P. (Editors) (1972). Thermophysical Properties of Matter, Volume 8 Thermal Radiative Properties: Nonmetallic Solids, IFI/Plenum, New York - Washington.
- Treadwell, C., and Pei, Z. J. (2003). Machining ceramics with rotary ultrasonic machining. Ceramic Industry, 39-42.
- Tsai, C.-H. and Chen, H.-W. (2004). The Laser shaping of ceramic by a fracture machining technique. International Journal of Advanced Manufacturing Technology, 23(5-6), 342-349.
- Tuersley, I. P., Jawaid, A., and Pashby, I. R. (1994). Review: various method of machining advanced ceramic materials. Journal of Materials Processing Technology, 42(4), 377-390.
- Töenshoff H. K., Gedrat O. (1991). Absorption behavior of ceramic materials irradiated with excimer-lasers. Proceedings of SPIE - The International Society for Optical Engineering, 1377, 38-44.
- Uematsu, T., Suzuki, K., Yanase, T., and Nakagawa, T. (1988). New complex grinding method for ceramic materials combined with ultrasonic vibration and electrodischarge machining. American Soc. of Mechanical Engineers (ASME), 135-140.
- Wang, J. C., and Hsu, S. M. (1994). Chemically assisted machining of ceramics. Journal of Tribology, Transactions of the ASME, 116(3), 423-429.

- Wang, W., Sun, J., and Qin, X. (2005). Modeling and simulation of microstructure evolution in ceramic sintering. *Nongye Jixie Xuebao/Transactions of the Chinese Society of Agricultural Machinery*, 36(10), 152-155.
- Westkämper, E. (1995). Grinding assisted by Nd:YAG lasers. *CIRP Annals - Manufacturing Technology*, 44(1), 317-320.
- Wiederhorn, S. M., Fields, A. B., and Hockey, B. J. (1994). Fracture of silicon nitride and silicon carbide at elevated temperatures. *Materials Science & Engineering A: Structural Materials: Properties, Microstructure and Processing*, A176(1-2), 51-60.
- Wittel, F. K., Schulte-Fischedick, J., Kun, F., Kröplin, B. H., and Friess, M. (2003). Discrete element simulation of transverse cracking during the pyrolysis of carbon fibre reinforced plastics to carbon/carbon composites. *Computational Materials Science*, 28(1), 1-15.
- Wobker, H. G., and Tonshoff, H. K. (1993). High efficiency grinding of structural ceramics. *Machining of Advanced Materials, Proceedings of the International Conference on Machining of Advanced Materials, NIST Special Publication*, 847, 171-184.
- Wuthrich, R., and Fascio, V. (2005). Machining of non-conducting materials using electrochemical discharge phenomenon - an overview. *International Journal of Machine Tools & Manufacture*, 45(9), 1095-1108.
- Yang, B., Deines, T. W., Geist, C. M. and Lei, S. (2007). An experimental study of laser assisted milling of silicon nitride ceramic. *Transactions of the North American Manufacturing Research Institute of SME*, 35, 473-480.
- Yang, B., and Lei, S. (2008). Laser-assisted milling of silicon nitride ceramic: a machinability study. *Int. J. Mechatronics and Manufacturing Systems*, 1(1), 116-130.
- Yang, B., Jiao, Y., and Lei, S. (2006). A study on the effects of microparameters on macroproperties for specimens created by bonded particles. *Engineering Computations (Swansea, Wales)*, 23(6), 607-631.
- Yang B., Shen, X., Lei, S. (2009). Mechanisms of edge chipping in laser-assisted milling of silicon nitride ceramics. *International Journal of Machine Tools and Manufacture*, 49(3-4), 344-350.
- Yang, B., Sun, J. G., Frink, E., Lei, S., and Lease, K. (2009). Assessment of part quality in laser assisted milling of silicon nitride ceramic. *The Proceedings of the 2009 ICALEO Congress, Laser Materials Processing Conference*, 489-498.
- Yin, L., Ives, L. K., and Jahanmir, S. (2003). Influence of grinding fluids on the abrasive machining of a micaceous glass ceramic. *Ceramic Engineering and Science Proceedings*, 24(3), 191-196.
- Zavattieri, P. D., Raghuram, P. V., and Espinosa, H. D. (2001). A computational model of ceramic microstructures subjected to multi-axial dynamic loading. *Journal of the Mechanics and Physics of Solids*, 49(1), 27-68.
- Zhang, Z. and Modest, M. F. (1998). Temperature-dependent absorptances of ceramics for Nd:YAG and CO₂ laser processing applications. *Journal of Heat transfer, Transactions of ASME*, 120(2), 322-327.

- Zhang, G., and Jahanmir, S. (2007). A method of fabricating oxide ceramic articles. http://www.isr.umd.edu/research/research_briefs/older_accomplishments/008_Ceramics/welcome.html.
- Zhang, G., and Cao, Y. (2000). A computational approach to evaluate surface integrity of glass ceramics. *Transactions of NAMRI/SME*, 28, 279-284
- Zhang, J. H., Ai, X., Lee, K. W., and Wong, P. K. (1996). Study on electro-discharge diamond wheel grinding (EDGM) of ceramic materials. *Materials and Manufacturing Processes*, 11(5), 763-774.
- Zhao, Y., Dong, S., Li, Z., and Wang, H. (1998). Diamond turning model in brittle-ductile transition of brittle materials. *Weixi Jiagong Jishu/Microfabrication Technology*, 4, 70-76.

Appendix A - Publications Related to Ph.D. Dissertation *

Refereed Conference Publications

- Shen, Xinwei** and Lei, Shuting (2009). Cutting simulation of laser-assisted milling of silicon nitride ceramics using PFC^{2D}. 2009 ASME International Manufacturing Science & Engineering Conference (MSEC), 225-232
- Shen, Xinwei** and Lei, Shuting (2008). Investigation on operating temperature in laser-assisted milling of silicon nitride ceramics. 2008 ASME International Manufacturing Science & Engineering Conference (MSEC), 168-374.
- Shen, Xinwei**, Liu, Wenjie and Lei, Shuting (2005). Three-dimensional thermal analysis for laser-assisted milling of silicon nitride ceramics using FEA. ASME American Society of Mechanical Engineers, Manufacturing Engineering Division, MED, 16-1, 445-452.
- Shen, Xinwei** and Lei, Shuting (2005). Distinct element simulation of laser-assisted machining of silicon nitride ceramics: surface/subsurface cracks and damage. ASME American Society of Mechanical Engineers, Manufacturing Engineering Division, MED, 16-2, 1267-1274.
- Shen, Xinwei** and Lei, Shuting (2004). Three-dimensional heat transfer and thermal stress analysis for laser-assisted milling of silicon nitride ceramics. 6th International Conference on Frontiers of Design and Manufacturing, Xi'an, China.
- Lei, Shuting, Kaitkay, Prasad and **Shen, Xinwei** (2004). Simulation of rock cutting using distinct element method - PFC^{2D}. Numerical Modeling in Micromechanics Via Particle Methods 2004, Proceedings of the 2nd International PFC Symposium, Kyoto, Japan, 63-71.

Refereed Journal Publications

- Shen, Xinwei** and Lei, Shuting (2010). Experimental study on operating temperature in laser-assisted milling of silicon nitride ceramics. International Journal of Advanced Manufacturing Technology (in press, DOI: 10.1007/s00170-010-2702-7).
- Shen, Xinwei**, Yang, Budong, and Lei, Shuting (2010). Distinct element modeling of laser-assisted machining of silicon nitride ceramics. Journal of Manufacturing Processes, 12(1), 30-37.

Note: Journal and conference papers on femtosecond laser micro-/nano-machining which are not related to this research are excluded in the dissertation

- Shen, Xinwei** and Lei, Shuting (2009). Thermal modeling and experimental investigation for laser-assisted milling of silicon nitride ceramics. *Journal of Manufacturing Science and Engineering, Transactions of the ASME*, 131(5), 051007-1-10.
- Yang, Budong, **Shen, Xinwei** and Lei, Shuting (2009). Distinct element modeling of the material removal process in conventional and laser-assisted machining of silicon nitride ceramics. *International Journal of Manufacturing Research*, 4(1), 74-94.
- Yang, Budong, **Shen, Xinwei** and Lei, Shuting (2009). Mechanisms of edge chipping in laser-assisted milling of silicon nitride ceramics. *International Journal of Machine Tools and Manufacture*, 49(3-4), 344-350.
- Shen, Xinwei** and Lei, Shuting (2006). Numerical fracture toughness test for improving workpiece model in machining simulation. *Transactions of the North American Manufacturing Research Institute of SME*, 34, 285-292.
- Shen, Xinwei** and Lei, Shuting (2010). Research on the effects of microparameters on weibull modulus in microstructural modeling of silicon nitride ceramics with discrete element method. *Journal of Materials Research*, (under review).
- Shen, Xinwei** and Lei, Shuting (2010). A study on the effects of microparameters on macroproperty of flexural strength of synthetic silicon nitride ceramics modeled by bonded particles. *Journal of Materials Science*, (under review).
- Shen, Xinwei** and Lei, Shuting (2010). Numerical Analysis of the dynamic process of laser-assisted milling of silicon nitride ceramics with discrete element method. *Materials and Manufacturing Processes*, (under review).
- Shen, Xinwei** and Lei, Shuting (2009). Numerical modeling and simulation of laser-assisted machining of silicon nitride ceramics with distinct element method: part I, creation of the synthetic specimen for machining simulation. *Journal of Manufacturing Science and Engineering, Transactions of the ASME*, (under review).
- Shen, Xinwei**, Yang, Budong, and Lei, Shuting (2009). Numerical modeling and simulation of laser-assisted machining of silicon nitride ceramics with distinct element method: part II, simulation of the dynamic cutting process. *Journal of Manufacturing Science and Engineering, Transactions of the ASME*, (under review).

Appendix B - Finite Element Discretization Solution: Newton-Raphson Procedure in ANSYS

Overview

The finite element discretization process yields a set of simultaneous equations:

where:

$$[K]\{U\} = \{F^a\} \quad (B.1)$$

$[K]$ = coefficient matrix

$\{U\}$ = vector of unknown DOF (degree of freedom) values

$\{F^a\}$ = vector of applied loads

If the coefficient matrix $[K]$ is itself a function of the unknown DOF values (or their derivatives) then Equation B.1 is a nonlinear equation. The Newton-Raphson method is an iterative process of solving the nonlinear equations and can be written as (Bathe(2)):

$$[K_i^T]\{\Delta U_i\} = \{F^a\} - \{F_i^{nr}\} \quad (B.2)$$

$$\{U_{i+1}\} = \{U_i\} - \{\Delta U_i\} \quad (B.3)$$

where:

$[K_i^T]$ = Jacobian matrix (tangent matrix)

i = subscript representing the current equilibrium iteration

$\{F_i^{nr}\}$ = vector of restoring loads corresponding to the element internal loads

Both $[K_i^T]$ and $\{F_i^{nr}\}$ are evaluated based on the values given by $\{U_i\}$. The right-hand side of Equation B.3 is the residual or out-of-balance load vector; i.e., the amount the system is out of equilibrium. A single solution iteration is depicted graphically in Figure B.1 for a one DOF model.

In a structural analysis, $[K_i^T]$ is the tangent stiffness matrix, $\{U_i\}$ is the displacement vector and $\{F_i^{nr}\}$ is the restoring force vector calculated from the element stresses. In a thermal analysis, $[K_i^T]$ is the conductivity matrix, $\{U_i\}$ is the temperature vector and $\{F_i^{nr}\}$ is the resisting load vector calculated from the element heat flows. In an electromagnetic analysis, $[K_i^T]$ is the Dirichlet matrix, $\{U_i\}$ is the magnetic potential vector, and $\{F_i^{nr}\}$ is the resisting load vector calculated from element magnetic fluxes. In a transient analysis, $[K_i^T]$ is

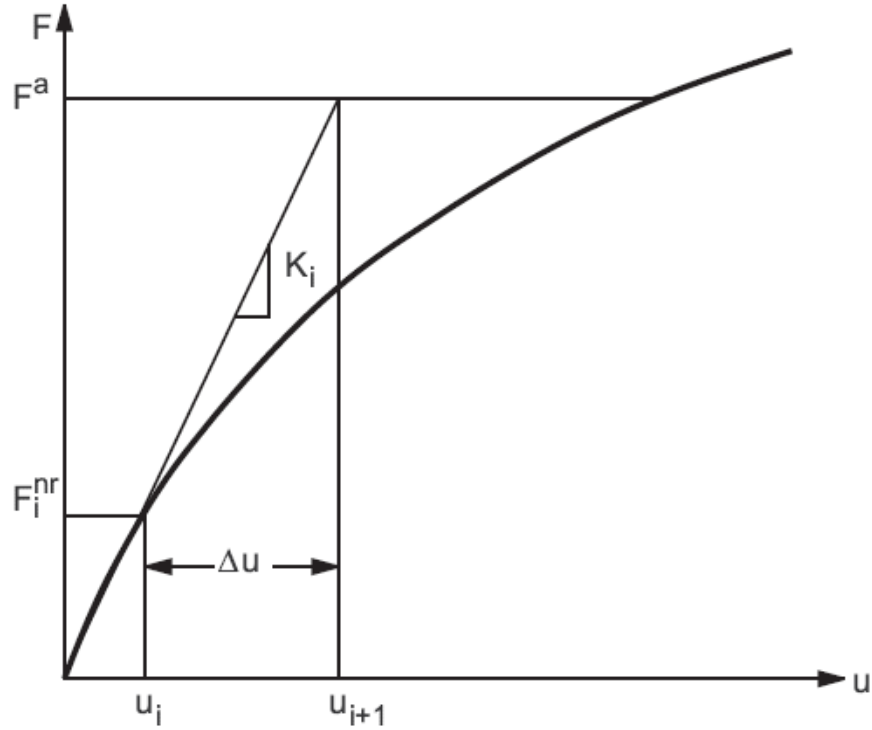


Figure B.1: Newton-Raphson solution - one iteration

the effective coefficient matrix and $\{F_i^{nr}\}$ is the effective applied load vector which includes the inertia and damping effects. As seen in the following figures, more than one Newton-Raphson iteration is needed to obtain a converged solution. The general algorithm proceeds as follows:

1. Assume $\{U_0\}$. $\{U_0\}$ is usually the converged solution from the previous time step. On the first time step, $\{U_0\} = \{0\}$.
2. Compute the updated tangent matrix $[K_i^T]$ and the restoring load $\{F_i^{nr}\}$ from configuration $\{U_i\}$.
3. Calculate $\{\Delta U_i\}$ from Equation B.3.
4. Add $\{\Delta U_i\}$ to $\{U_i\}$ in order to obtain the next approximation $\{U_{i+1}\}$ (Equation B.4).
5. Repeat steps 2 to 4 until convergence is obtained.

Figure B.2 shows the solution of the next iteration ($i+1$) of the example from Figure B.1. The subsequent iterations would proceed in a similar manner.

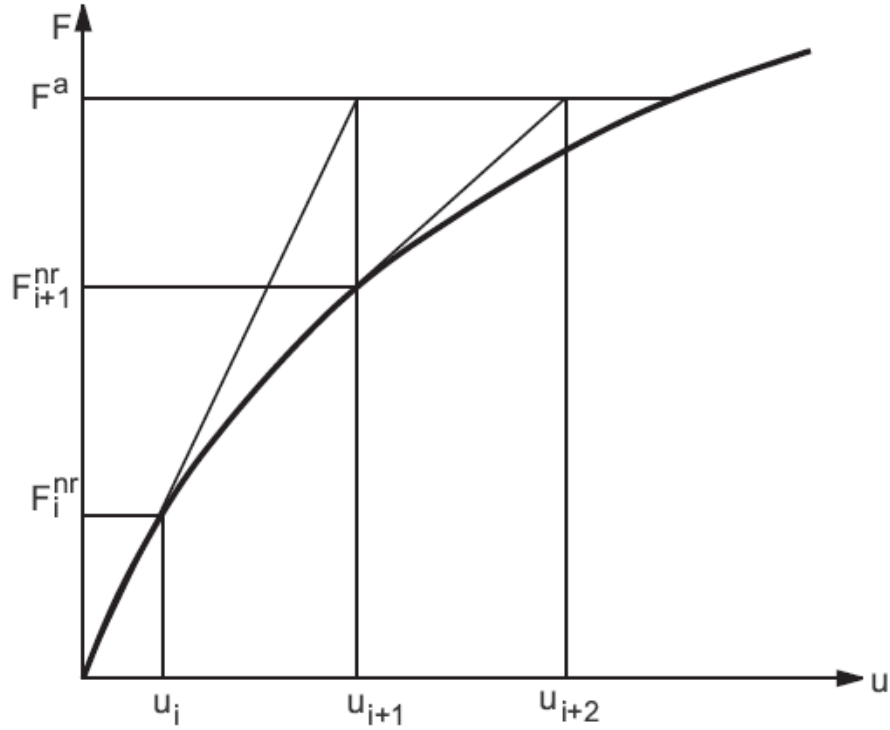


Figure B.2: Newton-Raphson solution - next iteration

The solution obtained at the end of the iteration process would correspond to load level $\{F^a\}$. The final converged solution would be in equilibrium, such that the restoring load vector $\{F_i^{nr}\}$ (computed from the current stress state, heat flows, etc.) would equal the applied load vector $\{F^a\}$ (or at least to within some tolerance). None of the intermediate solutions would be in equilibrium.

If the analysis included path-dependent nonlinearities (such as plasticity), then the solution process requires that some intermediate steps be in equilibrium in order to correctly follow the load path. This is accomplished effectively by specifying a step-by-step incremental analysis; i.e., the final load vector $\{F^a\}$ is reached by applying the load in increments and performing the Newton-Raphson iterations at each step:

$$[K_{n,i}^T]\{\Delta U_i\} = \{F_n^a\} - \{F_{n,i}^{nr}\} \quad (\text{B.4})$$

where

$[K_{n,i}^T]$ = tangent matrix for time step n, iteration i

$\{F_n^a\}$ = total applied force vector at time step n

$\{F_{n,i}^{nr}\}$ = restoring force vector for time step n, iteration i

This process is the incremental Newton-Raphson procedure and is shown in Figure B.3. The Newton-Raphson procedure guarantees convergence if and only if the solution at any iteration $\{U_i\}$ is “near” the exact solution. Therefore, even without a path-dependent nonlinearity, the incremental approach (i.e., applying the loads in increments) is sometimes required in order to obtain a solution corresponding to the final load level.

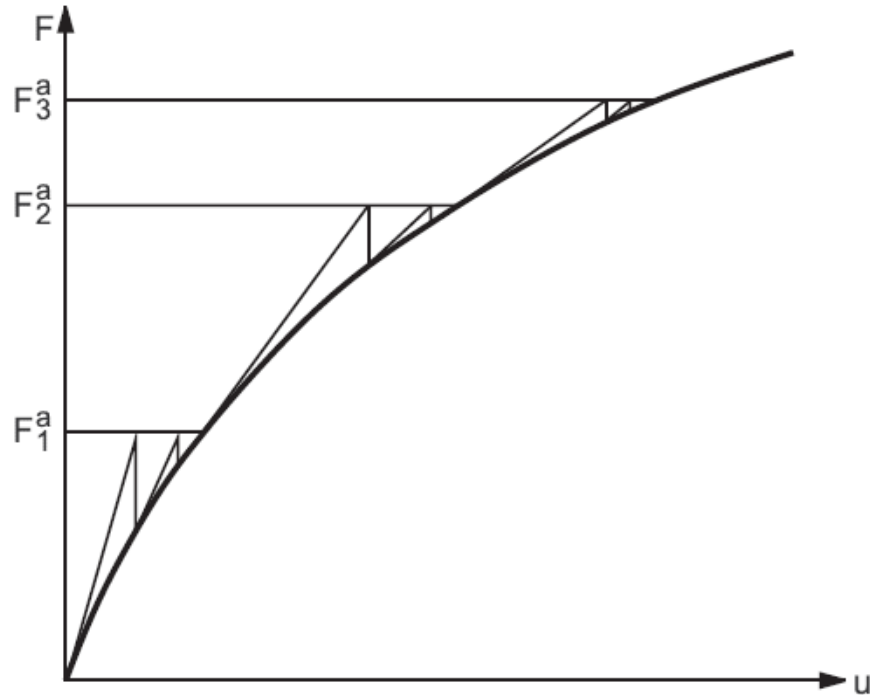


Figure B.3: Incremental Newton-Raphson procedure

When the stiffness matrix is updated every iteration (as indicated in B.3 and B.5) the process is termed a full Newton-Raphson solution procedure (NROPT,FULL or NROPT,UNSYM). Alternatively, the stiffness matrix could be updated less frequently using the modified Newton-Raphson procedure (NROPT,MODI). Specifically, for static or transient analyses, it would be updated only during the first or second iteration of each substep, respectively. Use of the initial-stiffness procedure (NROPT,INIT) prevents any updating of the stiffness matrix, as shown in Figure B.4. If a multistatus element is in the model, however, it would be updated at iteration in which it changes status, irrespective of the NewtonRaphson option. The modified and initial-stiffness Newton-Raphson procedures converge more slowly than the full Newton-Raphson procedure,

but they require fewer matrix reformulations and inversions. A few elements form an approximate tangent matrix so that the convergence characteristics are somewhat different.

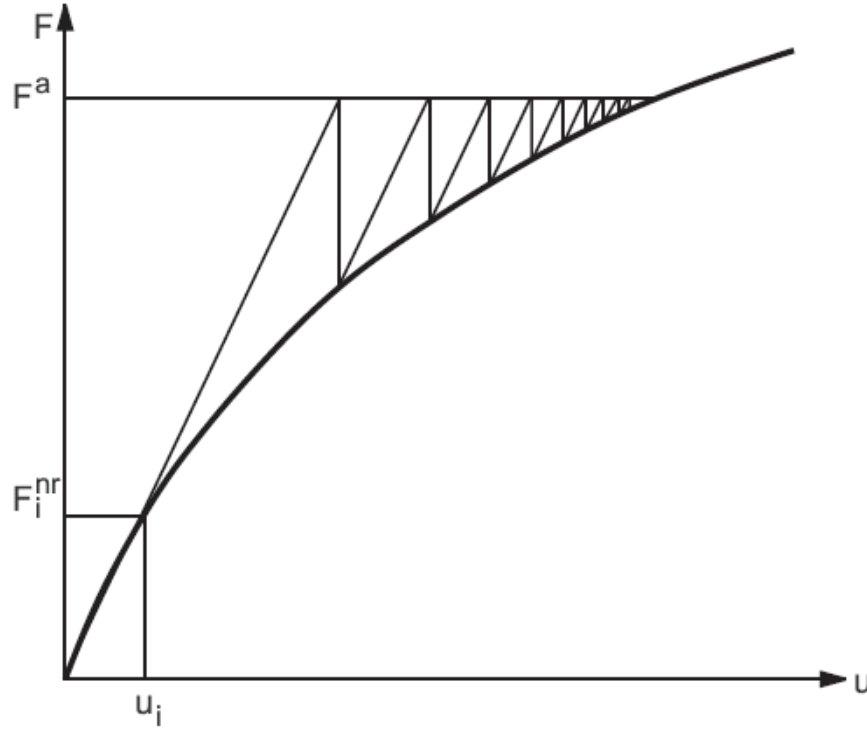


Figure B.4: Initial-stiffness newton-raphson

Convergence

The iteration process described in the previous section continues until convergence is achieved. The maximum number of allowed equilibrium iterations (input on NEQIT command) are performed in order to obtain convergence.

Convergence is assumed when

$$\|\{R\}\| < \varepsilon_R R_{ref} \quad (\text{out-of-balance convergence}) \quad (\text{B.5})$$

and/or

$$\|\{\Delta U_i\}\| < \varepsilon_U U_{ref} \quad (\text{DOF increment convergence}) \quad (\text{B.6})$$

where $\{R\}$ is the residual vector:

$$\{R\} = \{F^a\} - \{F^{nr}\} \quad (\text{B.7})$$

which is the right-hand side of the Newton-Raphson Equation B.3. $\{\Delta U_i\}$ is the DOF increment vector, ε_R and ε_U are tolerances (TOLER on the CNVTOL command) and R_{ref} and U_{ref} are reference values (VALUE on the CNVTOL command). $\|*\|$ is a vector norm; that is, a scalar measure of the magnitude of the vector (defined below).

Convergence, therefore, is obtained when size of the residual (disequilibrium) is less than a tolerance times a reference value and/or when the size of the DOF increment is less than a tolerance times a reference value. The default is to use out-of-balance convergence checking only. The default tolerance are .001 (for both ε_U and ε_R).

There are three available norms (NORM on the CNVTOL command) to choose from:

1. Infinite norm $\|\{R\}\|_{\infty} = \max|R_i|$
2. L₁ norm $\|\{R\}\|_1 = \sum|R_i|$
3. L₂ norm $\|\{R\}\|_2 = (\sum R_i^2)^{1/2}$

For DOF increment convergence, substitute Δu for R in the above equations. The infinite norm is simply the maximum value in the vector (maximum residual or maximum DOF increment), the L₁ norm is the sum of the absolute value of the terms, and the L₂ norm is the square root of the sum of the squares (SRSS) value of the terms, also called the Euclidean norm. The default is to use the L₂ norm.

The default out-of-balance reference value R_{ref} is $\|\{F^a\}\|$. For DOFs with imposed displacement constraints, $\{F^{nr}\}$ at those DOFs are used in the computation of R_{ref} . For structural DOFs, if $\|\{F^a\}\|$ falls below 1 .0, then R_{ref} uses 1 .0 as its value. This occurs most often in rigid body motion (e.g., stress-free rotation) analyses. For thermal DOFs, if $\|\{F^a\}\|$ falls below 1 .0E-6, then R_{ref} uses 1 .0E-6 as its value. For all other DOFs, R_{ref} uses 0.0. The default reference value U_{ref} is $\|\{u\}\|$.

Predictor

The solution used for the start of each time step n $\{U_{n,0}\}$ is usually equal to the current DOF solution $\{U_{n-1}\}$. The tangent matrix $[K_{n,0}]$ and restoring load $\{F^{n,0}\}$ are based on this configuration. The predictor option (PRED command) extrapolates the DOF solution using the previous history in order to take a better guess at the next solution.

In static analyses, the prediction is based on the displacement increments accumulated over the previous time step, factored by the time-step size:

$$\{U_{n,0}\} = \{U_{n-1}\} + \beta\{\Delta U_n\} \quad (\text{B.8})$$

where

$\{\Delta U_n\}$ = displacement increment accumulated over the previous time step

n = current time step

$$\{\Delta U_n\} = \sum_{i=1}^{\text{NEQIT}} \{\Delta U_i\} \quad (\text{B.9})$$

and β is defined as:

$$\beta = \frac{\Delta t_n}{\Delta t_{n-1}} \quad (\text{B.10})$$

where:

Δt_n = current time-step size

Δt_{n-1} = previous time-step size

β is not allowed to be greater than 5.

In transient analyses, the prediction is based on the current velocities and accelerations using the Newmark formulas for structural DOFs:

$$\{U_{n,0}\} = \{U_{n-1}\} + \{\dot{U}_{n-1}\}\Delta t_n + (0.5 - \alpha)\{\ddot{U}_{n-1}\}\Delta t_n^2 \quad (\text{B.11})$$

Where: $\{U_{n-1}\}$, $\{\dot{U}_{n-1}\}$, $\{\ddot{U}_{n-1}\}$ = current displacements, velocities and accelerations

Δt_n = current time-step size

α = Newmark parameter (input on TINTP command)

For thermal, magnetic and other first order systems, the prediction is based on the trapezoidal formula:

$$\{U_{n,0}\} = \{U_{n-1}\} + (1 - \theta)\{\dot{U}_{n-1}\}\Delta t_n \quad (\text{B.12})$$

where: $\{U_{n-1}\}$ = current temperatures (or magnetic potentials)

$\{\dot{U}_{n-1}\}$ = current rates of these quantities

θ = trapezoidal time integration parameter (input on TINTP command)

The subsequent equilibrium iterations provide DOF increments $\{\Delta u\}$ with respect to the predicted DOF value $\{U_{n,0}\}$, hence this is a predictor-corrector algorithm.

Adaptive Descent

Adaptive descent (Adptky on the N ROPT command) is a technique which switches to a “stiffer” matrix if convergence difficulties are encountered, and switches back to the full tangent as the solution converges, resulting in the desired rapid convergence rate.

The matrix used in the Newton-Raphson equation (Equation B.3) is defined as the sum of two matrices:

$$[K_i^T] = \xi[K^S] + (1 - \xi)[K^T] \quad (\text{B.13})$$

where:

$[K^S]$ = secant (or most stable) matrix

$[K^T]$ = tangent matrix

ξ = descent parameter

The program adaptively adjusts the descent parameter (ξ) during the equilibrium iterations as follows:

1. Start each substep using the tangent matrix ($\xi = 0$).
2. Monitor the change in the residual $\|\{R\}\|_2$ over the equilibrium iterations:
If it increases (indicating possible divergence):
 - remove the current solution if $\xi < 1$, reset ξ to 1 and redo the iteration using the secant matrix
 - if already at $\xi = 1$, continue iteratingIf it decreases (indicating converging solution):
 - If $\xi = 1$ (secant matrix) and the residual has decreased for three iterations in a row (or 2 if ξ was increased to 1 during the equilibrium iteration process by (a.) above), then reduce ξ by a factor of 1/4 (set it to 0.25) and continue iterating.
 - If the $\xi < 1$, decrease it again by a factor of 1/4 and continue iterating. Once ξ is below 0.0156, set it to 0.0 (use the tangent matrix).
3. If a negative pivot message is encountered (indicating an ill-conditioned matrix):
 - If $\xi < 1$, remove the current solution, reset $\xi = 1$ and redo the iteration using the secant matrix.
 - If $\xi = 1$, bisect the time step if automatic time stepping is active, otherwise terminate the execution.

The nonlinearities which make use of adaptive descent (that is, they form a secant matrix if $\xi > 0$) include: plasticity, contact, stress stiffness with large strain, nonlinear magnetics using the scalar potential formulation, the concrete element SOLID65 with KEYOPT(7) = 1, and the

membrane shell element SHELL41 with KEYOPT(1) = 2. Adaptive descent is used by default in these cases unless the line search or arc-length options are on. It is only available with full Newton-Raphson, where the matrix is updated every iteration. Full Newton-Raphson is also the default for plasticity, contact and large strain nonlinearities.

Line Search

The line search option (accessed with LNSRCH command) attempts to improve a Newton-Raphson solution $\{\Delta U_i\}$ by scaling the solution vector by a scalar value termed the line search parameter.

Consider Equation B.4 again:

$$\{U_{i+1}\} = \{U_i\} + \{\Delta U_i\} \quad (\text{B.14})$$

In some solution situations, the use of the full $\{\Delta U_i\}$ leads to solution instabilities. Hence, if the line search option is used, Equation B.5 is modified to be:

$$\{U_{i+1}\} = \{U_i\} + s\{\Delta U_i\} \quad (\text{B.15})$$

where:

$$s = \text{line search parameter, } 0.05 < s < 1.0$$

s is automatically determined by minimizing the energy of the system, which reduces to finding the zero of the nonlinear equation:

$$g_s = \{\Delta U_i\}^T (\{F^a\} - \{F^{nr}(s\{\Delta U_i\})\}) \quad (\text{B.16})$$

where:

g_s = gradient of the potential energy with respect to s

An iterative solution scheme based on regula falsi is used to solve Equation B.7.

Iterations are continued until either:

1. g_s is less than $0.5 g_0$, where g_0 is the value of Equation B.7 at $s = 0.0$ (that is, using $\{F_n\}$ for $\{F^{nr}(s\{\Delta U\})\}$).
2. g_s is not changing significantly between iterations.
3. Six iterations have been performed.

If $g_0 > 0.0$, no iterations are performed and s is set to 1.0. s is not allowed below 0.05.

The scaled solution $\{\Delta U_i\}$ is used to update the current DOF values $\{U_{i+1}\}$ in Equation B.4 and the next equilibrium iteration is performed.

Arc-Length Method

The arc-length method (accessed with ARCLEN,ON) is suitable for nonlinear static equilibrium solutions of unstable problems. Applications of the arc-length method involve the tracing of a complex path in the load-displacement response into the buckling/post buckling regimes. The arc-length method uses the explicit spherical iterations to maintain the orthogonality between the arc-length radius and orthogonal directions. It is assumed that all load magnitudes are controlled by a single scalar parameter (i.e., the total load factor). Unsmooth or discontinuous load-displacement response in the cases often seen in contact analyses and elastic-perfectly plastic analyses cannot be traced effectively by the arc-length solution method. Mathematically, the arc-length method can be viewed as the trace of a single equilibrium curve in a space spanned by the nodal displacement variables and the total load factor. Therefore, all options of the Newton-Raphson method are still the basic method for the arc-length solution. As the displacement vectors and the scalar load factor are treated as unknowns, the arc-length method itself is an automatic load step method (AUTOTS, ON is not needed). For problems with sharp turns in the load-displacement curve or path dependent materials, it is necessary to limit the arc-length radius (arc-length load step size) using the initial arc-length radius (using the NSUBST command). During the solution, the arc-length method will vary the arc-length radius at each arc-length substep according to the degree of nonlinearities that is involved.

The range of variation of the arc-length radius is limited by the maximum and minimum multipliers (MAXARC and MINARC on the ARCLEN command).

In the arc-length procedure, nonlinear Equation B.3 is recast associated with the total load factor λ :

$$[K_i^T]\{\Delta U_i\} = \lambda\{F^a\}\{F_i^{nr}\} \quad (B.17)$$

where λ is normally within the range $-1.0 \sim 1 \sim 1.0$. Writing the proportional loading factor λ in an incremental form yields at substep n and iteration i (see Figure B.5)

$$[K_i^T]\{\Delta U_i\} - \Delta\lambda\{F^a\} = (\lambda_n + \lambda_i)\{F^a\} - \{F_i^{nr}\} = -\{R_i\} \quad (B.18)$$

where:

$\Delta\lambda$ = incremental load factor (as shown in Figure B.5)

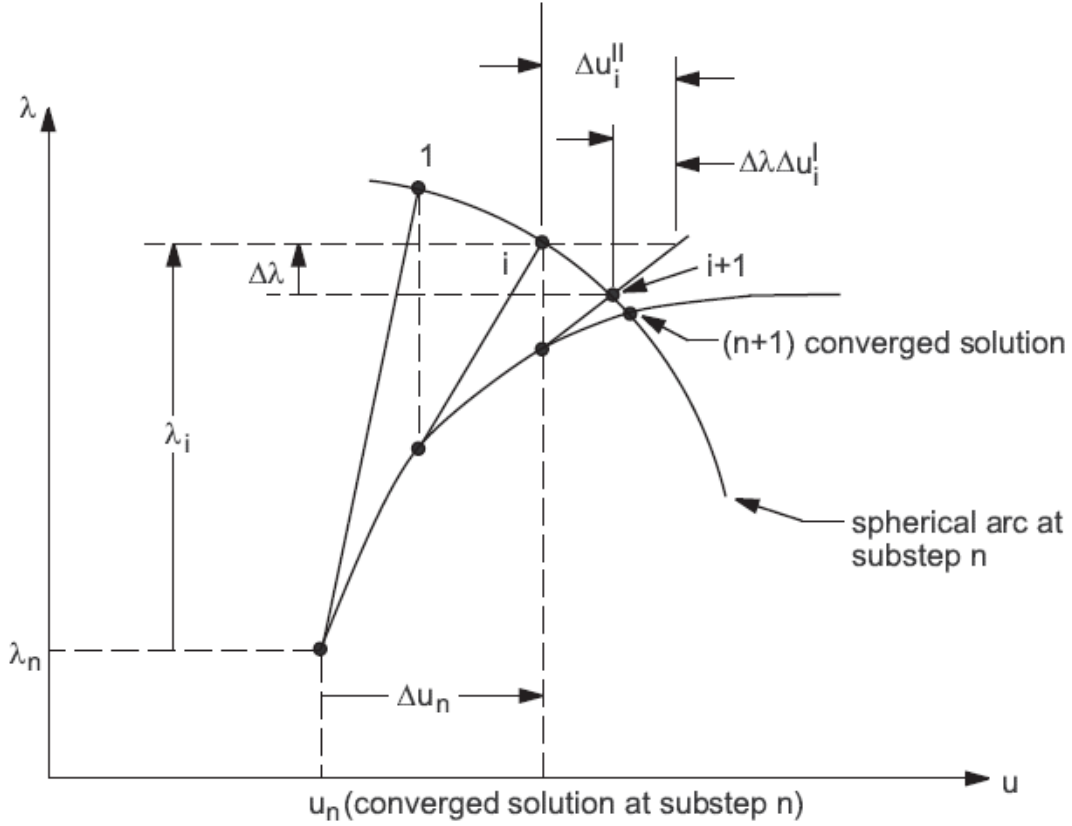


Figure B.5: Arc-length approach with full Newton-Raphson

The incremental displacement $\{\Delta U_i\}$ can be written into two parts following Equation B.19:

$$\{\Delta U_i\} = \Delta\lambda\{\Delta U_i^I\} + \{\Delta U_i^{II}\} \quad (\text{B.19})$$

where:

$\{\Delta U_i^I\}$ = displacement due to a unit load factor

$\{\Delta U_i^{II}\}$ = displacement increment from the conventional Newton-Raphson method

These are defined by:

$$\{\Delta U_i^I\} = [K_i^T]^{-1}\{F^a\} \quad (\text{B.20})$$

$$\{\Delta U_i^{II}\} = -[K_i^T]^{-1}\{R_i\} \quad (\text{B.21})$$

In each arc-length iteration, it is necessary to use Equation B.21 and Equation B.22 to solve for $\{\Delta U_i^I\}$ and $\{\Delta U_i^{II}\}$. The incremental load factor $\Delta\lambda$ in Equation B.20 is

determined by the arc-length equation which can be written as, for instance, at iteration i (see Figure B.5):

$$\ell_i^2 = \lambda_i^2 + \beta^2 \{\Delta U_n\}^T \{\Delta U_n\} \quad (\text{B.22})$$

where:

β = scaling factor (with units of displacement) used to ensure the correct scale in the equations

$\{\Delta U_n\}$ = sum of all the displacement increments $\{\Delta U_i\}$ of this iteration

The arc-length radius ℓ_i is forced, during the iterations, to be identical to the radius iteration ℓ_1 at the first iteration, i.e.

$$\ell_i = \ell_{i-1} = \dots = \ell_1 \quad (\text{B.23})$$

While the arc-length radius ℓ_1 at iteration 1 of a substep is determined by using the initial arc-length radius (defined by the NSUBST command), the limit range (defined by the ARCLen command) and some logic of the automatic time (load) step method.

Equation B.20 together with Equation B.23 uniquely determines the solution vector $(\Delta U_i, \Delta \lambda)^T$. However, there are many ways to solve for $\Delta \lambda$ approximately. The explicit spherical iteration method is used to ensure orthogonality. In this method, the required residual r_i (a scalar) for explicit iteration on a sphere is first calculated. Then the arc-length load increment factor is determined by formula:

$$\Delta \lambda = \frac{r_i - \{\Delta U_n\}^T \{\Delta U_i\}}{\beta^2 \lambda_i + \{\Delta U_n\}^T \{\Delta U_i\}} \quad (\text{B.24})$$

The method works well even in the situation where the vicinity of the critical point has sharp solution changes. Finally, the solution vectors are updated according to (see Figure B.5):

$$\{U_{i+1}\} = \{U_n\} + \{\Delta U_n\} + \{\Delta U_i\} \quad (\text{B.25})$$

and

$$\lambda_{i+1} = \lambda_n + \lambda_i + \Delta \lambda \quad (\text{B.26})$$

where:

n = current substep number

Values of λ_n and $\Delta \lambda$ are available in POST26 (SOLU command) corresponding to labels ALLF and ALDLF, respectively. The normalized arc-length radius label ARCL (SOLU) corresponds to value ℓ_i / ℓ_i^0 , where ℓ_i^0 is the initial arc-length radius defined (by

the NSUBST command) through Equation B.23 (an arc-length radius at the first iteration of the first substep).

In the case where the applied loads are greater or smaller than the maximum or minimum critical loads, arc-length will continue the iterations in cycles because $|\lambda|$ does not approach unity. It is recommended to terminate the arc-length iterations (using the ARCTRM or NCNV commands).